THÈSE

En vue de l'obtention du

DOCTORAT DE L'UNIVERSITÉ DE TOULOUSE

Délivré par :
Institut National Polytechnique de Toulouse (INP Toulouse)

Présentée et soutenue par :
Anthony Ruiz

Le 9 Février 2012

Simulations Numériques Instationnaires de la combustion turbulente et transcritique dans les moteurs cryotechniques
(Unsteady Numerical Simulations of Transcritical Turbulent Combustion in Liquid Rocket Engines)

École doctorale et discipline ou spécialité :
ED MEGEP : Énergétique et transferts

Unité de recherche :
CERFACS

Directeur(s) de Thèse :
B. Cuenot - Chef de projet CERFACS, HDR
L. Selle - Chargé de recherche CNRS

Rapporteurs :
F. Dupoirieux - Maître de Recherches à l'ONERA, HDR
J. Réveillon - Professeur à l'Université de Rouen

Autre(s) membre(s) du jury :
S. Candel - Professeur à l'Ecole Centrale Paris
P. Chassaing - Professeur émérite à l'INPT
D. Saucereau - Ingénieur SNECMA

Contents

List of Figures

List of Tables

Nomenclature

Roman letters

Symbol	Description	Units	Reference
C_p	Specific heat capacity at constant pressure	[J/(kg-K)]	
C_v	Specific heat capacity at constant volume	[J/(kg-K)]	
C_S	Constant of the standard Smagorinsky model	[-]	
C_w	Constant of the Wale model	[-]	
D_k	Molecular diffusivity of the species k	[m^2/s]	
e_s	Specific sensible energy	[J/kg]	
E	Total energy	[J/kg]	
E_a	Chemical activation energy	[J]	
g_{ij}	Component (i,j) of the velocity gradient tensor	[s^{-1}]	
$J_{k,i}$	Component (i) of the diffusive flux vector of the species k	[kg/(m^2 − s)]	
J	momentum-flux ratio (coaxial jets)	[-]	
k	Turbulent kinetic energy	[m^2/s^2]	
n_{dim}	Number of spatial dimensions	[-]	
P	Pressure	[N/m^2]	
q_i	Component (i) of the heat flux vector	[J/(m^2−s)]	
R	Universal gas constant	[J/(mol K)]	
s_{ij}	Component (i,j) of the velocity deformation tensor	[s^{-1}]	
T	Temperature	[K]	
$\underline{u}, u_i$	Velocity vector/ component (i)	[m/s]	
V_i^c	Component (i) of the correction diffusion velocity	[m/s]	
V_i^k	Component (i) of the diffusion velocity of the species k	[m/s]	
W	Molecular weight	[kg/mol]	
Y_k	Mass fraction of the species k	[-]	
$\mathcal{Z}$	Mixture fraction	[-]	

Greek letters

Symbol	Description	Units	Reference
δ_{ij}	Component (i,j) of the Kronecker delta	[-]	
$\bar{\Delta}$	Characteristic filter width	[m]	
$\Delta h^0_{f,k}$	Formation enthalpy of the species k	[J/kg]	
η_k	Kolmogorov length scale	[m]	
λ	Thermal conductivity	[J/(m-K)]	

μ	Dynamic viscosity	[kg/(m-s)]
ν	Kinematic viscosity	[m^2/s]
ν_t	Turbulent kinematic viscosity	[m^2/s]
Π_R	Reduced pressure = P/P_c	[-]
ϕ	Equivalence ratio	[-]
ρ	Density	[kg/m^3]
ρ_k	Density of the species k	[kg/m^3]
τ_R	Reduced temperature = T/T_c	[-]
τ_c	Characteristic chemical time scale	[s]
τ_{conv}	Characteristic convective time scale	[s]
τ_{ij}	Component (i, j) of the stress tensor	[N/m^2]
ζ	Artificial viscosity sensor	[-]
$\dot{\omega}_{kj}$	Reaction rate of the species k in the reaction j	[kg/(m^3s)]
$\dot{\omega}_T$	Heat release	[J/(m^3s)]
ω_{ac}	Acentric factor used in real gas EOS	[]

Non-dimensional numbers

Symbol	Description	Reference
Da	Damköhler	
Le	Lewis	
Re	Reynolds	
Sc	Schmidt	

Subscripts

Symbol	Description
0	Thermodynamic reference state
c	Critical point property
k	General index of the species
pb	Pseudo-boiling point property

Superscripts

Symbol	Description
$\bar{f}$	Filtered quantity
$\tilde{f}$	Density-weighted filtered quantity

Abreviations

Acronym	Description
DNS	Direct Numerical Simulation
EOS	Equation Of State
GH2	Gaseous Hydrogen
GOx	Gaseous Oxygen
LES	Large-Eddy Simulation
LOx	Liquid Oxygen
LRE	Liquid Rocket Engine
NSCBC	Navier-Stokes Characteristic Boundary Condition
PR EOS	Peng-Robinson Equation Of State
RANS	Reynolds Averaged Navier-Stokes
RMS	Root Mean Square
SRK EOS	Soave-Redlich Kwong Equation Of State

A Marina,

Acknowledgments/Remerciement

En premier lieu, j'aimerais remercier tous les membres du jury: le président Sébastien Candel et Patrick Chassaing pour avoir partagé leur érudition en combustion et turbulence, les rapporteurs Francis Dupoirieux et Julien Réveillon qui m'ont permis de préparer la soutenance grâce à leurs remarques et questions très détaillées, Didier Saucereau et Marie Theron pour l'intérêt qu'ils ont porté à mes travaux de thèses et pour leurs éclairages sur les enjeux et problématiques industrielles de R&T en propulsion liquide aérospatiale. Aussi, j'aimerais remercier mon employeur, Snecma Vernon du groupe Safran et le CNES, pour avoir financer mes travaux de recherche pendant trois ans (thèse CIFRE). Je tiens aussi à remercier les centres de calculs français et européens (CINES, IDRIS et PRACE), pour les allocations d'heures de calcul dont mes collaborateurs et moi ont pu bénéficier pour mener à bien les simulations massivement parallèles dont les résultats sont présentées dans le présent manuscrit.

Je tiens tout d'abord à remercier Thierry Poinsot et Bénédicte Cuenot pour m'avoir accueilli au sein de l'équipe combustion du CERFACS, qu'ils dirigent (avec Laurent Gicquel et les autres séniors) avec talent. Je remercie aussi Thierry pour m'avoir poussé à présenter mes résultats de thèse dans des conférences internationales (ce qui m'a permis de rencontrer mon futur employeur !) et pour m'avoir accueilli chez lui pendant quelques jours agréables à Portolla Valley. Je remercie aussi Marie Labadens, qui est un pilier essentiel du bon fonctionnement de l'équipe CFD.

Je remercie naturellement l'équipe CSG (le trio Gérard Dejean, Fabrice Fleury, Isabelle D'Ast et l'autre côté du couloir Patrick Laporte et Nicolas Monnier) pour leur support inconditionnel et leurs réponses multiples à mes demandes toujours plus farfelues. Je remercie tout particulièrement Séverine Toulouse et Nicole Boutet pour leur sympathie et pour avoir partagé ensemble la passion pour les animaux. Je n'oublie pas Chantal Nasri, Michèle Campassens et Lydia Otero pour leur amabilité et leur gentillesse naturelles.

Je tiens ensuite à remercier tous les "sages" du CERFACS qui m'ont formé au calcul hautes performances et à la mécanique des fluides numérique. En particulier Thomas Schmitt, qui est en quelque sorte mon père spirituel et qui a pris le temps de répondre à toutes mes questions sur le supercritique et sur AVBPRG lors de mon stage de fin d'études. Je remercie aussi tout particulièrement Gabriel Staffelbach, qui m'a énormément guidé et aidé dans la manipulation et la modification d'AVBP, qui m'a fait confiance et m'a ouvert les portes des centres de calculs nationaux et européens. Un grand merci à Laurent Selle, qui m'a pris en main en deuxième année en prononçant la phrase : 'j'aimerais qu'on travaille ensemble'. Travailler avec Laurent, qui est très rigoureux et très exigeant, m'a permis de me structurer et de m'endurcir. Travailler avec Laurent a aussi été une grande source de satisfaction, je me rappelle encore de son 'ça déchire ça !', en voyant mes premiers résultats de DNS. Je remercie aussi les autres séniors avec qui j'ai pu interagir : Olivier Vermorel, Eléonore Riber et Antoine Dauptain. Je remercie ensuite d'autres "anciens" de l'équipe combustion du CERFACS, qui m'ont apporté des éclairages: Guilhem Lacaze, Olivier Cabrit, Matthieu Leyko, Matthieu Boileau, Félix Jaegle, Marta Garcia, Nicolas Lamarque, Simon Mendez et Florent Duchaine.

Après les sages, je remercie les "apprentis sorciers", qui ont partagé ces trois années

de thèse, avec leurs bons et leurs mauvais moments. Je remercie tout d'abord Benedetta Franzelli, le guru officiel de Cantera, avant que Jean-Philippe Rocchi ne prenne le relais. Merci à vous deux et merci à toi Jean-Phi, d'être resté jusqu'à la dernière minute, la veille de ma soutenance, pour essayer d'éclaircir avec moi certains mystères des flammes de diffusion. Je remercie aussi Jorge Amaya, Camilo Silva et Pierre Wolf pour avoir joué quelques notes de musique (entre autres) avec moi au début de la thèse. Je remercie Alexandre Neophytou, pour ses éclairages sur les flammes triples et pour son humour 'so british', Matthias Kraushaar pour son dévouement sans faille pour organiser des parties de foot, Ignacio Duran pour les discussions en espagnol, Mario Falese pour sa curiosité naturelle, Rémy Fransen et Stéphane Jauré pour m'avoir suivi dans l'aventure avbpedia, Patricia Sierra et Victor Granet pour leur aide sur le départ aux Etats-Unis et Alexandre Eyssartier qui a dû résoudre la moitié des bugs sur les conditions limites à cause de son lien de parenté avec genprofile !

Enfin, je remercie du fond du coeur mes collègues proches, devenu amis. Merci à Gregory Hannebique pour son soutien moral, pour les coups qu'il a essayé de me porter à la boxe française, pour ses parcours top niveau (ou un peu plus) et pour son amitié, du fat mec ! Merci à Sebastian Hermeth pour ses bons conseils d'amis qui permettent d'avancer dans la vie et pour ses cours d'allemand, jetzt alles klar. Merci à Geoffroy Chaussonnet pour avoir réussi à supporter Greg et aussi pour avoir toujours le mot pour rire. Merci à Thomas Pedot, mon partenaire de bureau, qui m'a permis d'avancer dans la thèse et a su me 'booster' quand il fallait. Merci à Ignacio Hernandez, alias Nacho (ou p.....a), pour avoir emmené quotidiennement un parfum de banane dans notre bureau et pour nous avoir fait découvrir la fête à Madrid. Merci à Jean-François Parmentier pour m'avoir redonné le goût du fun dans la thèse, avec des sujets de discussions totalement décousus et merci aussi de m'avoir laissé finir ma thèse en se limitant à 15 minutes de temps de paroles par jour.

Je remercie aussi mes parents, en particulier ma mère qui a dévoué sa vie à sa famille et qui a passé tant d'heures à mes côtés pour m'aider à m'instruire pendant mon enfance. Je remercie aussi mon père qui m'a permis de développer mon originalité (notamment en référence au 'Loup et l'agneau') et qui est source d'inspiration pour moi. C'est aussi grâce à mes parents formidables et à leur éducation que j'ai pu réussir un doctorat.

Je n'ai pas réalisé ce travail de thèse tout seul. J'ai été porté par ma femme, mon amour, mon âme soeur, Marina Beriat-Ruiz, qui m'a soutenu contre vents et marées tout au long de ces trois années. Elle a su m'encourager dans les moments où je n'y croyais plus, écouter mes problèmes de viscosité artificielle, comprendre ce qu'était un maillage et comprendre que ma passion me poussait à passer mes soirées et mes week-ends devant un ordinateur au lieu de passer du temps avec celle que j'aime. Le plus dur moments ont été les derniers mois de rédaction, entremêlés avec l'organisation d'un mariage, d'un déménagement et d'un départ à l'étranger. Merci d'avoir supporter sur tes épaules le poids de mon absence.

Chapter 1

Introduction

Warning: the confidential parts of this thesis work have been removed and this manuscript does not represent the entirety of the work done by Anthony Ruiz during his PhD.

1.1 Operating principle of Liquid Rocket Engines

The aim of a launcher is to safely send human beings or satellites into space. The european space launcher Ariane 5, depicted in Fig. 1.1 is dedicated to the launch of commercial satellites. The thrust that generates the lift-off and acceleration of the launcher is produced by two different types of engine: solid-fuel rockets (or boosters) and Liquid Rocket Engines (LREs), as shown in Fig. 1.1. These two different types of engine are complementary: the boosters generate a very large thrust at take-off but are depleted rapidly, whereas the main LRE generates a smaller thrust but for a longer period of time.

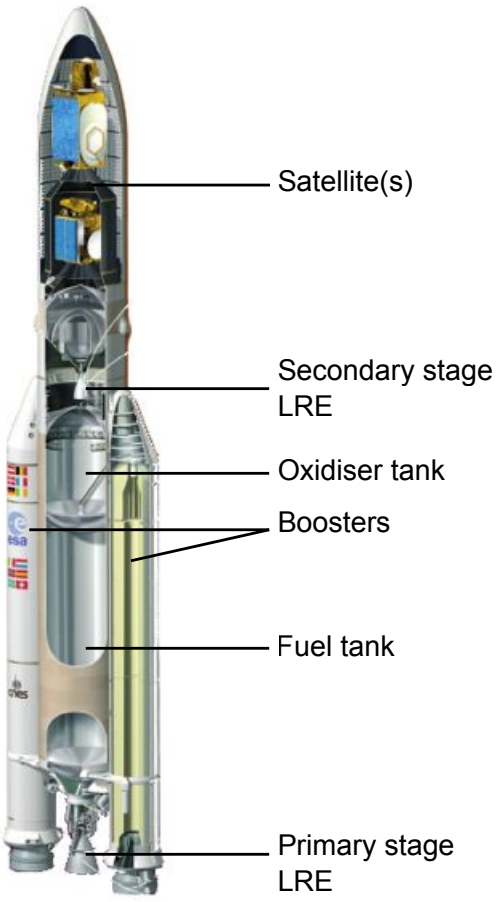

Figure 1.1: The main components of the Ariane 5 european space launcher.

Propulsion in boosters and LREs is obtained through the "reaction principle": the ejection of fluid momentum from the nozzle of the engine, generates thrust. In this system, the combustion chamber plays a central role, since it converts chemical energy, stored in the reactants (also called propellants) into kinetic energy.

Within the boosters, solid reactants are arranged in a hollow cylindrical column, as shown in Fig. 1.2. Combustion takes place at the inner surface of the cylindrical column, whose volume decreases due to abrasion until total depletion of reactants. The operating principle of a booster is fairly simple, however, complex and coupled phenomena take place within it. For instance,

the failure of the space shuttle challenger, which lead to the deaths of its seven crew members in 1986, was caused by the leakage of hot gases through the rocket casing, due to abnormal ignition stress. These hot gases caused a structural failure of the adjacent tank [William P. Rogers 1986]. In order to understand these complex phenomena, fully-coupled simulation of reacting fluid flow and structure oscillations are now possible. For instance, see [Richard & Nicoud 2011], among others.

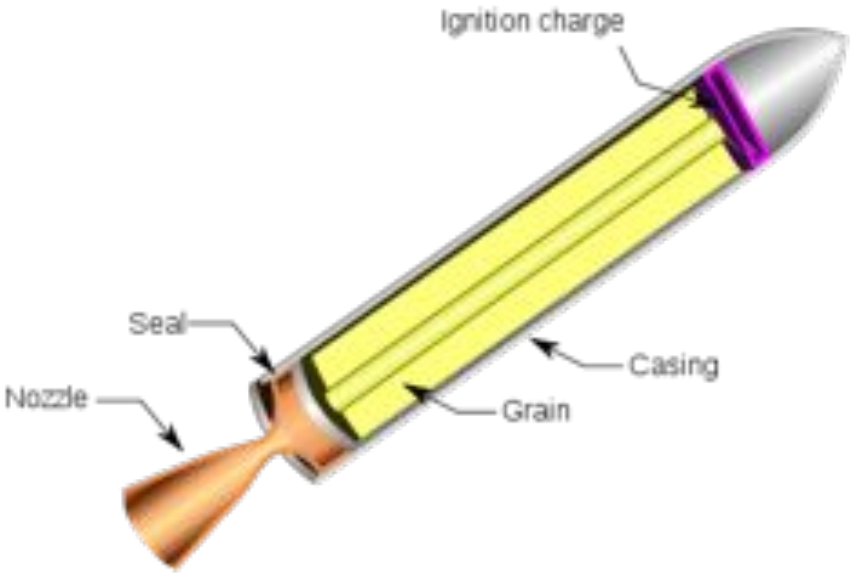

Figure 1.2: Components of a booster.

The operating principle and the type of combustion are totally different in a LRE. Fuel and oxidizer are stored in a liquid state, in separate tanks, as shown in Fig. 1.1. Turbopumps inject these non-premixed reactants into the combustion chamber, where they mix through molecular diffusion and turbulence, and burn, which expands the gas mixture.

Figure 1.3 shows the operating principle of Vulcain 2 [Snecma 2011]. The torque required to drive the turbopumps is generated by the flow of combustion products from the gas generator, which is a small combustion chamber, through turbine blades. A small amount of this torque is used to inject reactants into the gas generator itself. Finally, to start the gas generator, a solid combustion starter drives the turbopumps for a few seconds.

In general, the combustion chamber of a LRE is composed of a large number of coaxial injectors, arranged on a single plate as shown in Fig. 1.4. This compact arrangement of multiple flames enables a large delivery of thermal power in a small volume. The thermal power delivered by Vulcain 2 is 2.5 GW and the volume of the combustion chamber is 20 L. This yields a very large power density of 50 GW/m^3, which is equivalent to the power of 50 nuclear units in 1 cubic meter.

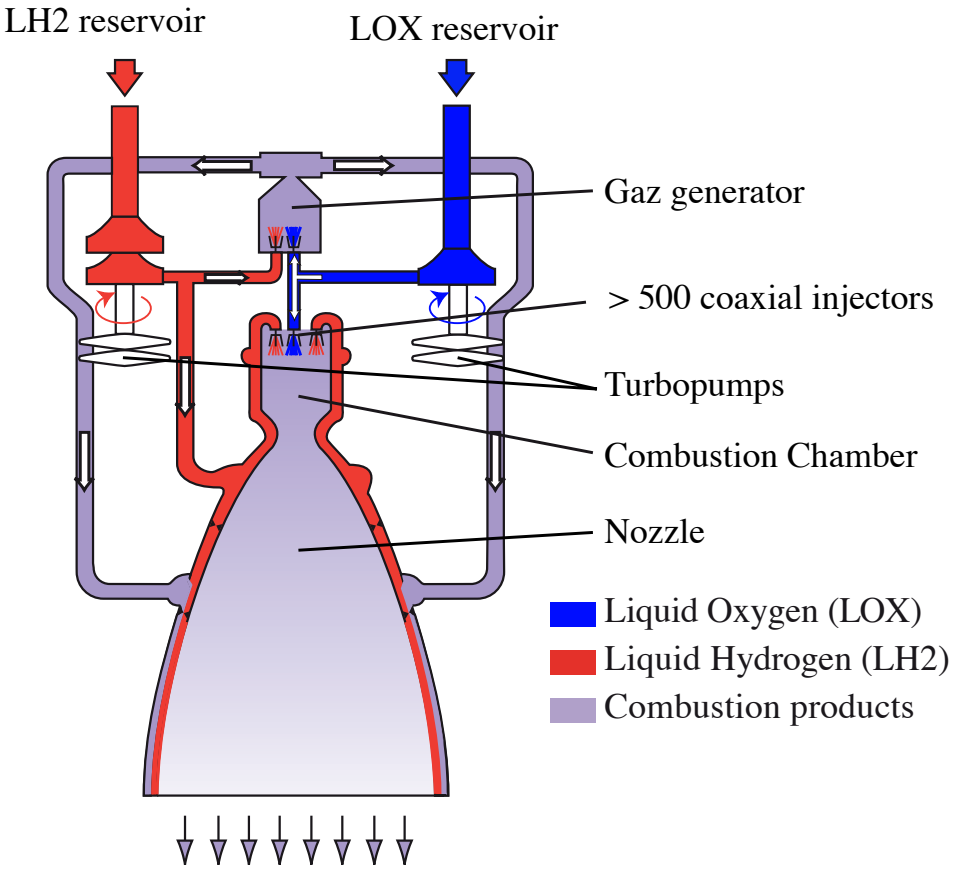

Figure 1.3: Operating principle of the Vulcain 2 engine [Snecma 2011].

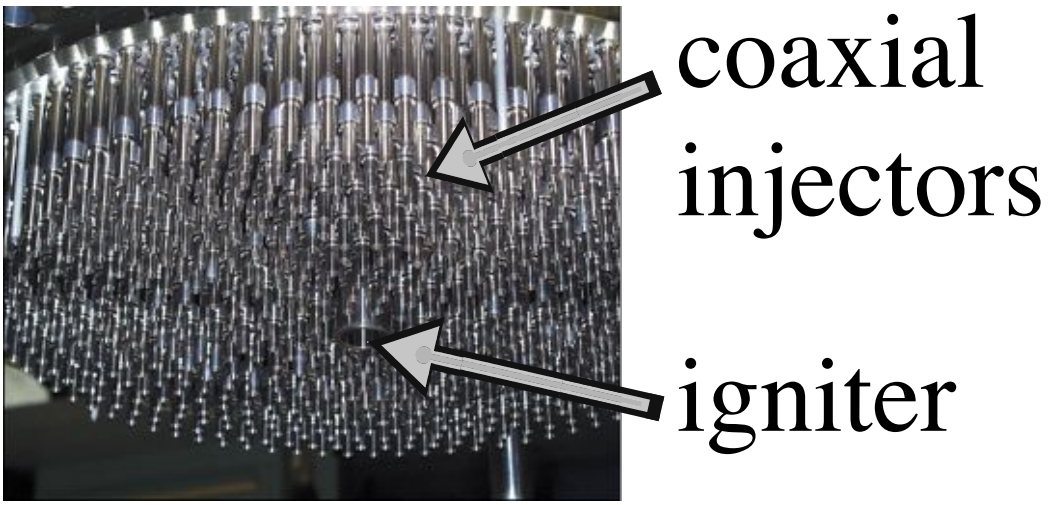

Figure 1.4: Injection plate of the Vulcain 2 LRE, composed of 566 coaxial injectors [Astrium 2011]

1.2 Combustion in LREs

This thesis work is focused on flame dynamics inside the combustion chambers of LREs (gas generator and main combustion chamber). The detailed understanding of combustion physics inside these critical propulsive organs can provide useful guidelines for improving the design of LREs.

This section reflects the state of the art in the field of combustion, at operating conditions relevant to LREs. There are several reviews on the topic, which are synthesized and complemented herein. The reader is referred to the following publications for more details on:

- experimental results [Candel *et al.* 1998,Haidn & Habiballah 2003,Candel *et al.* 2006, Oschwald *et al.* 2006, Habiballah *et al.* 2006]
- theory and modeling of turbulent supercritical mixing [Bellan 2000,Bellan 2006] and combustion [Oefelein 2006]

1.2.1 Preliminary Definitions

1.2.1.1 Supercritical and transcritical injection

In the reservoirs of a launcher, reactants are stored at a very low temperature, typically 100 K for oxygen and 20 K for hydrogen. This gives the reactants a very large density, which allows to reduce the dimension of the reservoirs and increases the possible payload. In the combustion chamber, heat release expands the gas mixture and increases its temperature. For instance, the adiabatic flame temperature of a pure H_2/O_2 flame at 10 MPa is $T_{adiab} = 3800$ K.

Since the main LRE of a launcher is started at the ground level, the initial pressure inside the combustion chamber is around 0.1 MPa. After ignition, the pressure rises until the nominal value is reached, which is approximately equal to 10 MPa.

Thus, the path followed by an O_2 fluid parcel from the reservoir to the flame zone in a LRE at nominal operating conditions is schematically represented by the arrow on the top Fig. 1.5, which shows the states of matter, as well as isocontours of heat capacity, in a T-P diagram for pure oxygen. Below the critical pressure ($P_{c,O_2} = 5.04$ MPa), the boiling line (or saturation curve) is the frontier between the liquid and gaseous state. By extension, at supercritical pressure, the pseudo-boiling line (T_{pb},P_{pb}) follows the local maxima of heat capacity and is thus the solution of the following system:

$$\begin{aligned} P &> P_c \\ \left.\frac{\partial C_p}{\partial T}\right)_P &= 0 \end{aligned} \tag{1.1}$$

The injection of oxygen inside a LRE is called 'transcritical' because of the crossing of the pseudo-boiling temperature, which is accompanied with a change of thermophysical quantities (such as density or diffusion coefficients) that vary from liquid-like (for $T < T_{pb}$) to gas-like (for $T > T_{pb}$) values.

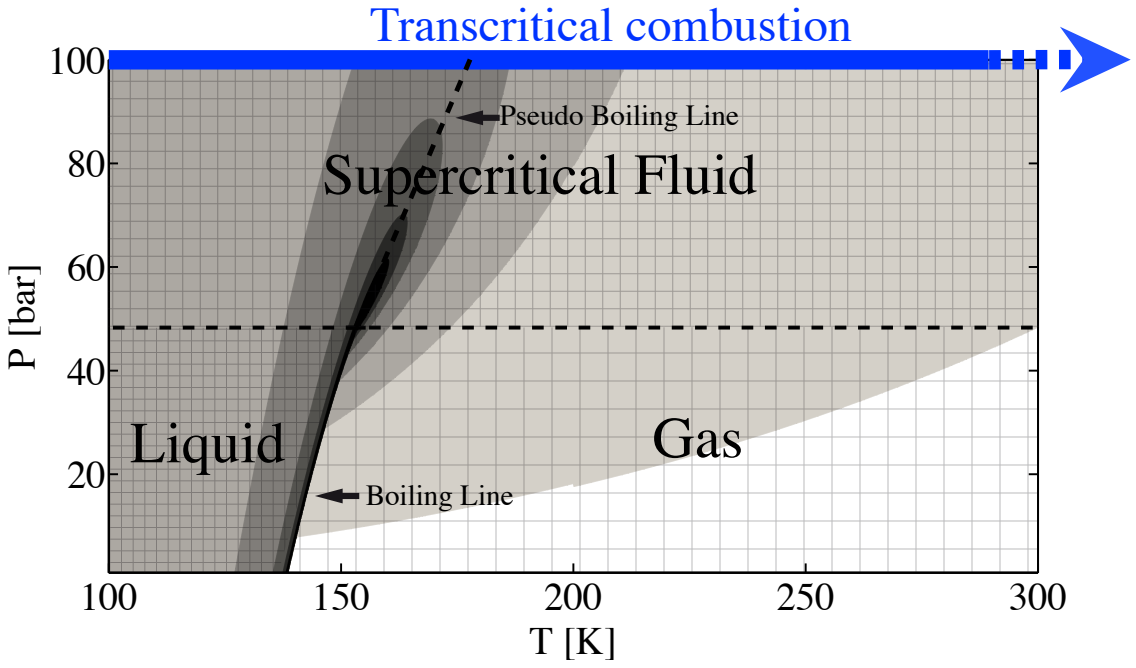

Figure 1.5: Heat capacity isocontours computed with the Soave-Redlich-Kwong equation of state (see Eq. 2.44): white = 10^3 J/K/kg; black=10^4 J/K/kg.

1.2.1.2 Scalar dissipation rate and Damköhler number

For non-premixed combustion, there is a balance between the mass flux of reactants to the flame front and the burning rates of these reactants. The mass flux of reactants to the flame front is directly related to species gradients, which determine the intensity of molecular fluxes. The scalar dissipation rate is a measure of the molecular diffusion intensity and defines the inverse of a fluid time scale:

$$\chi = 2D|\nabla \mathcal{Z}|^2 \tag{1.2}$$

where D is the thermal diffusivity (m^2/s), and $\mathcal{Z}$ is the mixture fraction [Peters 2001].

The mixture fraction is equal to the mass fraction of the H atom for pure H_2/O_2 reacting flows [Poinsot & Veynante 2005] and depends on the number of species contained in the gas mixture. For instance, for the detailed chemical scheme used in Chap. 3, the mixture fraction reads:

$$\mathcal{Z} = W_H \left(2\,\frac{Y_{H_2}}{W_{H_2}} + 2\,\frac{Y_{H_2O}}{W_{H_2O}} + \frac{Y_H}{W_H} + \frac{Y_{OH}}{W_{OH}} + 2\,\frac{Y_{H_2O_2}}{W_{H_2O_2}} + \frac{Y_{HO_2}}{W_{HO_2}} \right) \tag{1.3}$$

where Y_k and W_k are the mass fraction and the molecular weight of the species k.

The ratio of the flow time t_{flow} and the chemical time t_{chem} is the Damköhler number:

$$\mathrm{Da} = \frac{t_{flow}}{t_{chem}} \tag{1.4}$$

$$= \frac{A}{\chi} \tag{1.5}$$

where A is a typical Arrhenius pre-exponential of the chemical kinetic scheme.

1.2.1.3 Mixture ratio

The mixture ratio E is the ratio of the injected mass flow rate of oxidizer $\dot{m}_O$ and fuel $\dot{m}_F$ inside a combustion chamber:

$$E = \frac{\dot{m}_O}{\dot{m}_F} \tag{1.6}$$

In a LRE, fuel is generally injected in excess to protect the chamber walls from oxidation, consequently, the mixture ratio is generally smaller than the stoichiometric mass ratio s:

$$s = \frac{\nu'_O W_O}{\nu'_F W_F} \tag{1.7}$$

where ν'_O and ν'_F are the stoichiometric coefficients of an overall unique reaction [Poinsot & Veynante 2005]:

$$\nu'_F F + \nu'_O O \rightarrow \text{Products} \tag{1.8}$$

For H_2/O_2 combustion, $s = 8$ and for CH_4/O_2 combustion, $s = 4$.

1.2.2 Experimental studies

Flame structure at subcritical pressure

Experimental studies of flame patterns in rocket conditions were first conducted at subcritical pressure, with coaxial injectors feeded with H_2/LOx. The pioneering experimental works of [Herding *et al.* 1996, Snyder *et al.* 1997, Herding *et al.* 1998] have allowed to determine some key characteristics of cryogenic propellant combustion that are now well established, using advanced optical diagnostics (OH^* together with Planar Laser Induced Fluorescence (PLIF)). One of the most important feature that has been discovered is the anchoring of the flame on the injector rim, independently of operating conditions for H_2/O_2.

The OH^* technique use the physical principle that the flame emits light that is composed of wavelengths representative of the local gas composition. By sensing the light at a given wavelength, the location of species involved in chemical kinetics can be revealed within the flow field. The excited hydroxyl radical OH^* is a suitable flame indicator since it is an intermediate species and is thus only present at the flame front, whereas H_2O is also present in the burnt gases. The OH^* signal is an integration along the line-of-sight of the chemiluminiscence and although it provides an overview of the instantaneous reacting zone inside the flow field, it does not provide a precise view of the flame shape, which is an important information for the design of engines and for validation purposes.

In the PLIF technique, a laser sheet excites an intermediate species (OH for instance) that emits light to relax towards an unexcited state. This technique was used at subcritical pressure in [Snyder *et al.* 1997] to observe instantaneous flame fronts and study the flame shape and stabilization in reacting LOx/H_2 flows. Because the signal-to-noise ratio is

deteriorated with increasing pressure, the PLIF technique was only used at moderate pressures (less than 1 MPa) in the 1990s. Thus, the only technique available for the study of high-pressure reacting flow at that time was OH^* emission.

A major breakthrough in the experimental study of cryogenic propellant combustion was made in [Herding *et al.* 1998], where the Abel transform was first use to retrieve a cut through a time-averaged OH^* signal, with the assumption of axi-symmetry. This technique was then used in experimental studies of high-pressure reacting flows, to precisely monitor the effects of operating conditions and geometry of injectors on the flame pattern [Juniper *et al.* 2000, Singla *et al.* 2005].

Subcritical and supercritical characteristics of atomization

Since nitrogen is an inert species and bears similar characteristics to oxygen (molar mass and critical point), it has been used as an alternative species for the study of the characteristics of atomization of jets inside LREs, at subcritical and supercritical conditions. Most non-reacting experimental results have been obtained at the Air Force Research Laboratory (AFLR) and the German Aerospace Center (DLR) [Chehroudi *et al.* 2002a, Chehroudi & Talley 2001, Chehroudi *et al.* 2002b, Mayer *et al.* 1998b, Mayer & Branan 2004, Branam & Mayer 2003, Mayer & Smith 2004, Mayer *et al.* 1996, Mayer *et al.* 2000, Mayer *et al.* 2001, Mayer *et al.* 1998a, Mayer & Tamura 1996, Mayer *et al.* 2003]. It has been shown that the crossing of either the critical temperature or the critical pressure impacts atomization. At subcritical conditions, because of the joint action of aerodynamic forces and surface tension, ligaments and droplets are formed at the surface of liquid jets. At supercritical conditions (either $T > T_c$ and/or $P > P_c$), surface tension vanishes and droplets are absent from the surface of jets. Instead, in the case of a transcritical injection (see Fig. 1.5), a diffusive interface between dense and light fluid develops, where waves or 'comb-like' structures can form. Figure 1.6 shows a time sequence of a transcritical N_2/supercritical He (inert substitute for hydrogen) mixing layer, where traveling waves are observed in the diffuse interface [Teshome *et al.* 2011]. The luminance of a shadowgraph is sensitive to gradients of refractive index, which allow to localize interfaces between jets having different densities.

The normalization of the injection temperature and the chamber pressure by the critical coordinates defines the reduced temperature τ_R and the reduced pressure π_R

$$\tau_R = \frac{T}{T_c} \tag{1.9}$$

$$\pi_R = \frac{P}{P_c}, \tag{1.10}$$

and allows to identify the atomization regime.

It is thus expected that during the ignition transient of LRE, the mixing between oxygen and hydrogen is greatly impacted by the crossing of the critical pressure.

Flame structure at supercritical pressure

The first experimental results obtained at supercritical pressure, at operating conditions that are relevant to LREs, have been obtained in [Juniper *et al.* 2000]. The same advanced

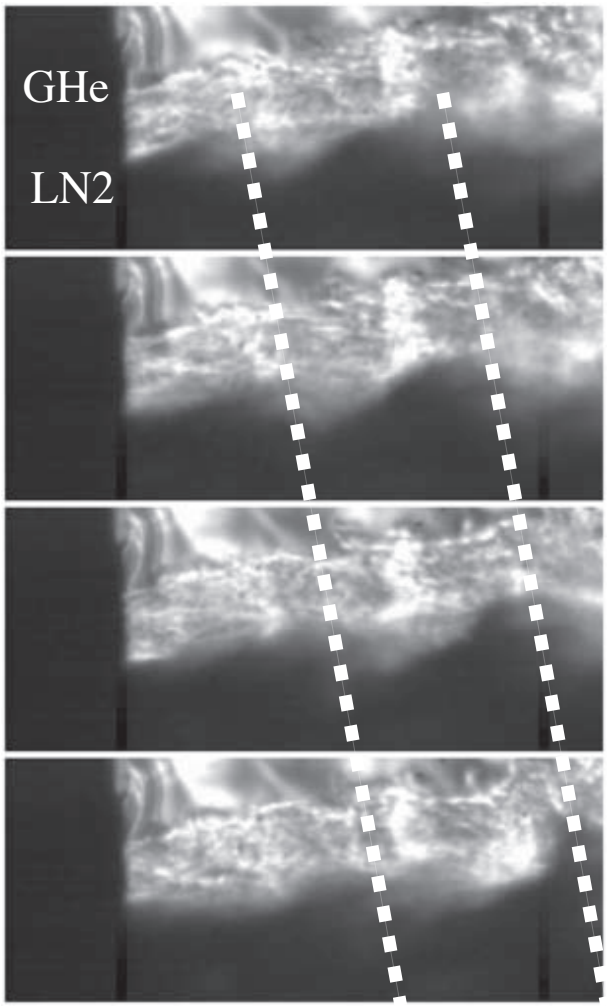

Figure 1.6: Shadowgraphs at successive instants (time between frames is 0.1 ms) of a transcritical N_2/supercritical He mixing layer [Teshome *et al.* 2011].

optical diagnostics (OH^* and PLIF) that were developed and used at subcritical pressure have successfully been applied to high-pressure combustion. An instantaneous OH^* image is shown in Fig. 1.7(a), a time-averaged OH^* image and its Abel transform is shown in the top and the bottom of Fig. 1.7(b), respectively. One can clearly see the progress that has been made in optical diagnostics using the Abel transform, where highly reacting zone can be observed at the inner shear layer, in the near-injector region, and where an opening turbulent flame brush can be observed further downstream.

Other important features of cryogenic propellant combustion were discovered in later work [Juniper & Candel 2003a], where a stabilization criterion has been devised, which essentially states that the lip height should be larger than the flame thickness to enable flame anchoring on the injector rim and overall flame stabilization.

In [Singla *et al.* 2005], methane was used instead of hydrogen, which have enabled the identification of a new flame structure under doubly transcritical injection conditions: two separate flames were observed at the inner and the outer shear layers of a coaxial

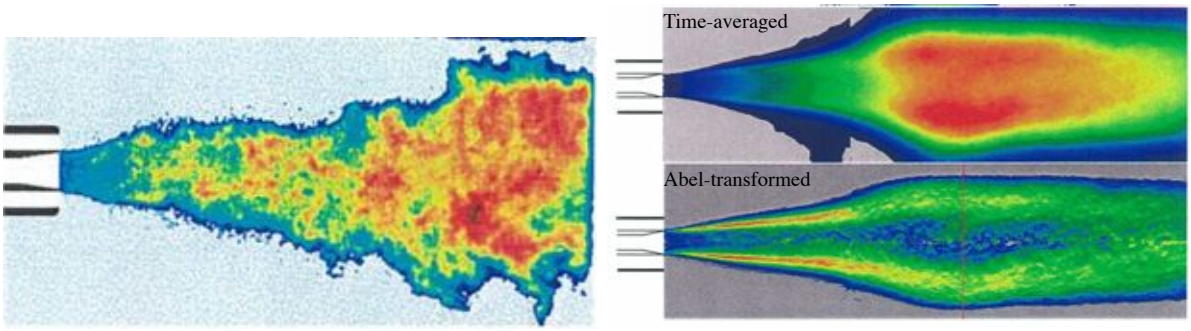

(a) (b)

Figure 1.7: Flame shape visualizations using OH^*, in a coaxial LOx/GH_2 injector [Juniper 2001]: (a) instantaneous image, (b) top: time-averaged image; bottom: Abel-transformed image. The pressure is 7 MPa.

injection.

In comparison with the Abel transform of a time-averaged OH^* signal, the PLIF provides an instantaneous visualization of the flame front and enables the study of unsteady features of combustion, such as moving flame tip at the stabilization point or flame front wrinkling due to turbulent motions. However, [Singla *et al.* 2006,Singla *et al.* 2007] are the only experimental studies that have successfully used the PLIF technique at supercritical pressures, in transcritical conditions, as shown in Fig. 1.8. On the latter figure, there is no signal from the upper flame sheet as most of the light from the laser is absorbed by the OH distribution on the lower side facing the sheet transmission window.

A close-up view of the near-injector region of PLIF images have shown that transcritical LOx/GH_2 flames are stabilized on the injector rim, which indicates that in this type of flames, the Damköhler number (see Eq. 1.4) is sufficiently large to prevent extinction.

More recently, other experimental studies of reacting fluid flows in conditions relevant to LRE, have been conducted in [Locke *et al.* 2010], at an unprecedented data acquisition rate, using shadowgraphy. Since the flame zone is a region with large density gradients (because of thermal expansion), it can be visualized using shadowgraphy. This has allowed to observe new features of cryogenic propellant combustion, such as the emission of oxygen pockets from the inner jet, as shown in Fig. 1.9, which might play an important role on unsteady heat release and possibly combustion instabilities.

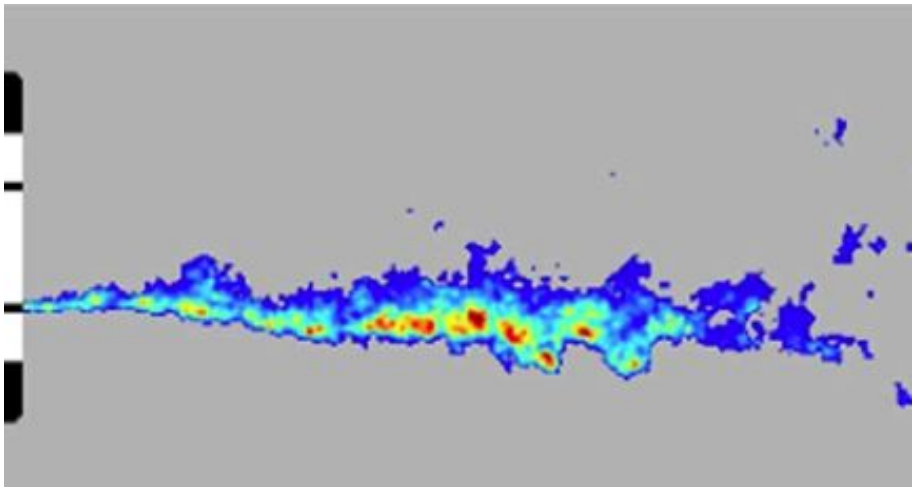

Figure 1.8: OH PLIF image of a LOx/GH_2 cryogenic flame [Singla *et al.* 2007].

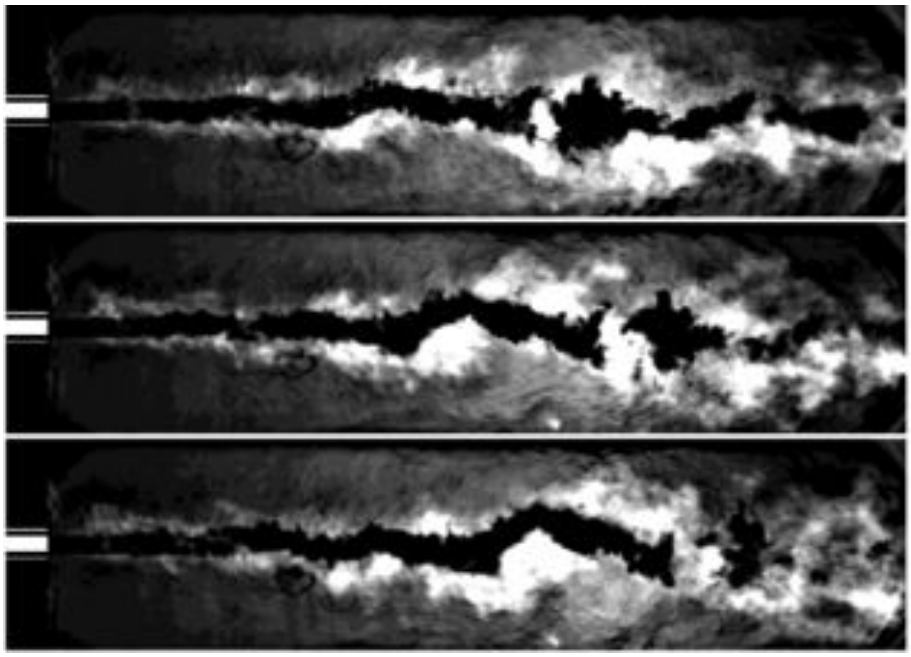

Figure 1.9: Shadowgraphs of a transcritical H_2/O_2 reacting flow at 6 MPa, taken at successive instants (time between frames is 0.25 ms) [Locke *et al.* 2010].

Influence of operating conditions and geometry of coaxial injector

Figure 1.10, extracted from [Schumaker & Driscoll 2009], shows a schematic of the near-field mixing layers in a coaxial jet. An inner shear layer is located at the interface

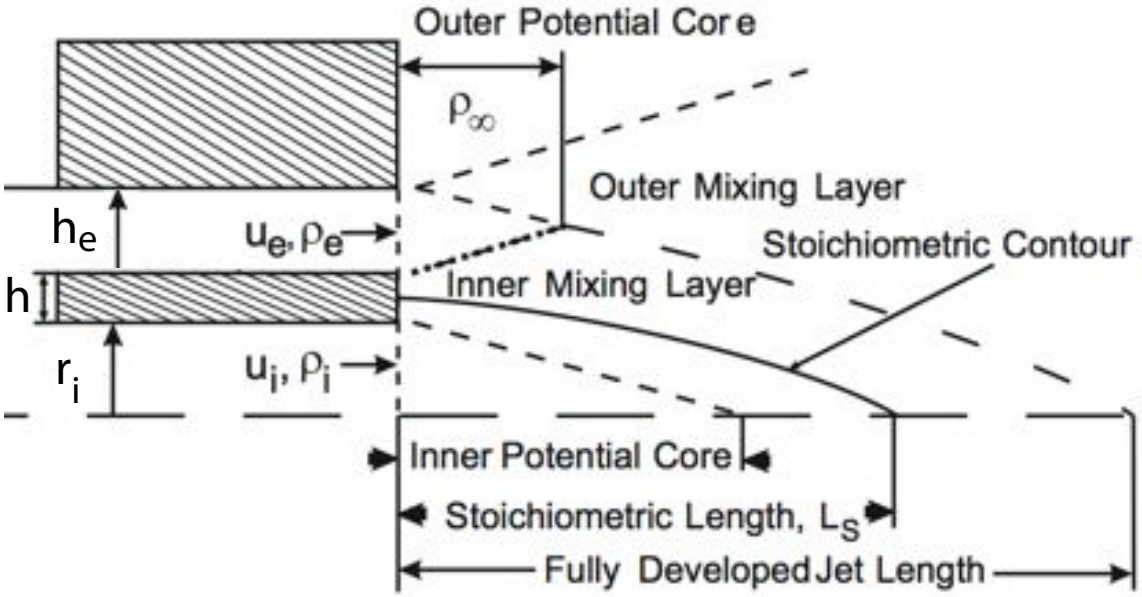

Figure 1.10: Schematic of coaxial jet injector and the near-field mixing layers [Schumaker & Driscoll 2009]

between the high-speed outer light jet and the low-speed inner dense jet. The outer shear layer lies in between the outer hydrogen and the recirculated gases of the combustion chamber.

An efficient coaxial injector should maximize turbulent mixing of reactants so that the resulting flame length and temperature stratification of burnt gases is as small as possible.

The Reynolds number compares a convection time $\tau_c = L/u$ and a diffusion time $\tau_d = \rho L^2/\mu$:

$$\begin{aligned} Re &= \frac{\tau_d}{\tau_c} \\ &= \frac{\rho L U}{\mu} \end{aligned} \tag{1.11}$$

with ρ the density (kg/m^3), L a characteristic length scale (m), U a velocity (m/s) and μ the dynamic viscosity (Pa.s). For a coaxial injector, a Reynolds number is defined for each of the inner and outer streams:

$$Re_i = \frac{\rho_{O_2} d_i U_i}{\mu_{O_2}} \tag{1.12}$$

$$Re_o = \frac{\rho_{H_2} h_e U_e}{\mu_{H_2}} \tag{1.13}$$

where the reference lengths are the inner diameter d_i ($= 2\ r_i$) and the outer channel height h_e. These Reynolds numbers characterize the fluid flow inside the feeding lines, immediately upstream of the injection plane. Because of the high injection velocities inside a LRE, the Reynolds number is large, typically above 10^5, which ensures the jets issuing from the coaxial injector rapidly transition towards turbulence. Thus, in the context of LREs, the Reynolds number is generally not an influential parameter.

Experimental studies [Snyder *et al.* 1997, Lasheras *et al.* 1998, Favre-Marinet & Camano Schettini 2001] have identified the density ratio R_ρ and the momentum-flux ratio J as the two numbers influencing mixing efficiency in coaxial configurations:

$$R_\rho = \frac{\rho_{O_2}}{\rho_{H_2}} \tag{1.14}$$

$$J = \frac{\rho_{H_2} U_{H_2}^2}{\rho_{O_2} U_{O_2}^2}. \tag{1.15}$$

The velocity ratio appears to be less influential:

$$R_u = \frac{u_{H_2}}{u_{O_2}}, \tag{1.16}$$

$$\tag{1.17}$$

and can be deduced from the density and momentum-flux ratio: $R_u = \sqrt{J\ R_\rho}$. [Favre-Marinet & Camano Schettini 2001] have determined that the potential core length is proportional to $J^{-1/2}$ for variable-density non-reacting jets, over a very wide range of values ($0.1 < J < 50$), spanning typical values in LRE (1-20).

The geometry of the coaxial injector also influences combustion efficiency. In particular, it has been shown in [Juniper *et al.* 2000, Juniper & Candel 2003b] that recessing the inner LOx tube from the outer H_2 tube increases combustion efficiency. This point is treated in more details in Chap. 4.

1.2.3 Numerical studies

Temporal mixing layers

The pioneering work of [Bellan 2000, Okong'o & Bellan 2002b, Bellan 2006] relied on Direct Numerical Simulations (DNSs) of temporal non-reacting mixing layers to study the impact of real-gas thermodynamics on the characteristics of turbulent mixing. These studies also constituted databases that were used *a priori* and *a posteriori* to determine the validity of closure terms for Large Eddy Simulation (LES). These studies lead to the following major findings:

- shear-induced instability at the interface between a dense and a light fluid give rise to larger velocity fluctuations in the light fluid than in the dense fluid and the density gradient redistributes turbulent kinetic energy from the perpendicular to the parallel direction of the interface [Okong'o & Bellan 2002b]
- because real-gas equation of states are non-linear, an additional subgrid-scale term, related to the filtering of pressure, requires closure in the LES framework [Bellan 2006].

Recently, [Foster 2009, Foster & Miller 2011] have studied a temporal reacting mixing layer between H_2 and O_2, at a large Reynolds number, and extended the *a priori* analysis of subgrid-scale turbulent fluxes to reacting conditions. However, these studies have not yet determined an adequate closure of subgrid-scale terms that could be used in LES simulations of realistic configurations.

Round jets

Several numerical studies attempted to predict the difference in turbulent mixing induced by the crossing of the critical pressure or the critical temperature.

In [Zong *et al.* 2004, Zong & Yang 2006], the effect of chamber pressure on supercritical turbulent mixing was investigated with LESs of the round jet experiments conducted with N_2 in [Chehroudi *et al.* 2002a]. An increase in the ambient pressure results was shown to provoke an earlier transition of the jet into the self-similar regime, because of reduced density stratification. Figure 1.11 shows radial distributions of normalized density at various axial locations, showing the existence of a self-similar region in supercritical jets. In [Schmitt *et al.* 2010b], the effect of injection temperature on supercritical turbulent mixing was investigated with LESs of the round jet experiments conducted with N_2 in [Mayer *et al.* 2003]. The comparison between the mean axial density profiles obtained in the numerical simulation and the experimental measurements showed good agreement. The increase of the injection temperature above the pseudo-boiling temperature (see Eq. 1.1), lead to an early transition of the jet into the self-similar regime.

RANS simulations of the cryogenic round jet experiments were also conducted in [Mayer *et al.* 2003, Kim *et al.* 2010], and were able to qualitatively reproduce the mean density profiles from the experiment.

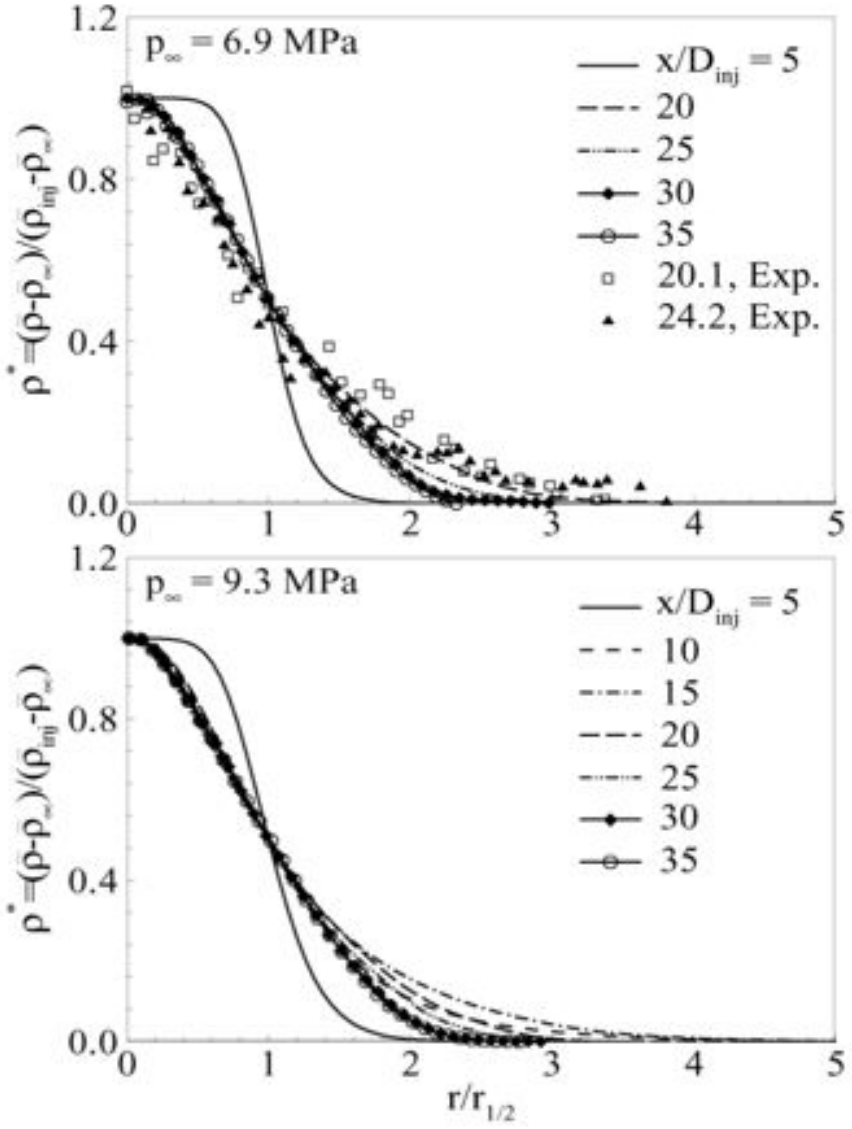

Figure 1.11: Radial distributions of normalized density at different axial locations (T_∞ = 300 K, u_{inj} = 15 m/s, T_{inj} = 120 K, D_{inj} = 254 μm) [Zong & Yang 2006]

Flame stabilization region

To the author's knowledge, [Oefelein & Yang 1998] is the first numerical work that focused on the stabilization point of a cryogenic LOx/GH_2 flame. In these numerical simulations, the flames were stabilized at the injector rim for supercritical and transcritical mixing, as shown in Fig. 1.12. The stabilizing effect of the transcritical density gradient was evidenced from these simulations, as visually observed when comparing the transcritical and the supercritical flame shapes in Figs. 1.12(a) and 1.12(b), respectively. The stabilization of the flame tip at the injector rim has later been confirmed in other experimental [Juniper *et al.* 2000, Singla *et al.* 2007] and numerical studies [Juniper & Candel 2003a].

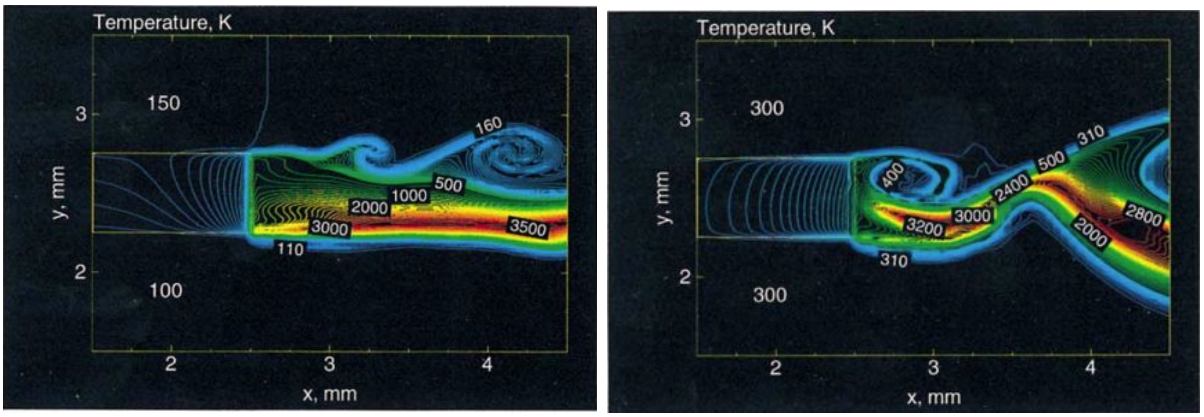

(a) (b)

Figure 1.12: Contours of temperature for the near-field region for (a) supercritical and (b) transcritical mixing [Oefelein & Yang 1998].

In [Zong & Yang 2007] the study of the near-field region of a coaxial injector fed-in with transcritical LOx/GCH_4, in the same configuration as in [Singla *et al.* 2007], also showed a flame stabilized at the injector rim.

Transcritical flame structure

Laminar counterflow diffusion flames have been studied in the literature, to scrutinize the transcritical chemical structure of LOx/GH_2 and LOx/GCH_4 flames.

In [Juniper *et al.* 2003], the study of a diffusion flame developing between gaseous hydrogen and liquid oxygen at atmospheric pressure, showed that the flame structure bears similar characteristics as a flame located in between gaseous reactants. It was also shown that the extinction strain rate is large for LOx/GH_2 (larger than $5\ 10^5\ s^{-1}$), and increases with pressure.

In [Pons *et al.* 2008] and [Ribert *et al.* 2008], it was shown for LOx/GH_2 and LOx/GCH_4 that the heat release rate per unit flame surface increases with the square root of strain rate and pressure, while the extinction strain rate evolve quasi-linearly with pressure. These studies also showed that a transcritical flame structure is very similar to a supercritical flame structure.

In the previous studies, the chemical reaction rates were assumed to bear a standard Arrhenius form. In [Giovangigli *et al.* 2011], real-gas thermodynamics derivations were used to compute chemical production rates from chemical potentials. It was found that the non-ideal chemical production rates may have an important influence at very high pressure (typically above 20 MPa).

Coaxial jet flames

Only a few numerical studies have used LES as a tool for detailed understanding of flame dynamics inside LREs. For instance, [Masquelet *et al.* 2009] led a 2D-axisymmetric simulation of a multiple-injector combustor, and focused on wall heat flux induced by combustion. Transcritical LESs of coaxial injectors were conducted in [Schmitt *et al.* 2009, Schmitt *et al.* 2010a] and [Matsuyama *et al.* 2006, Matsuyama *et al.* 2010], where the flow complexity was captured with great precision and good agreement with experimental data, as shown in Fig. 1.13.

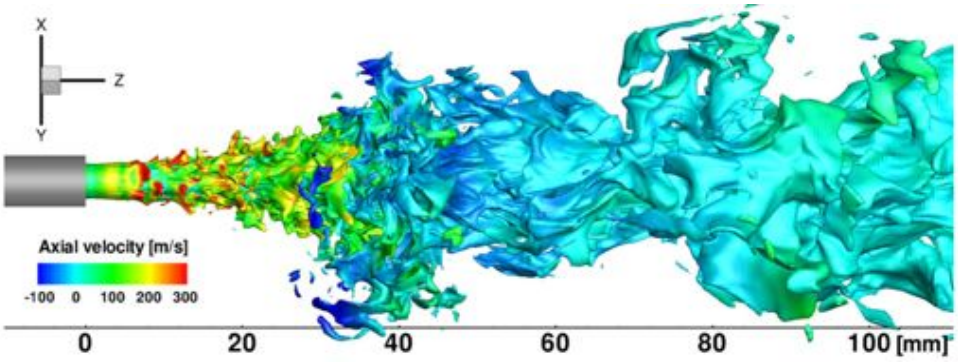

(a)

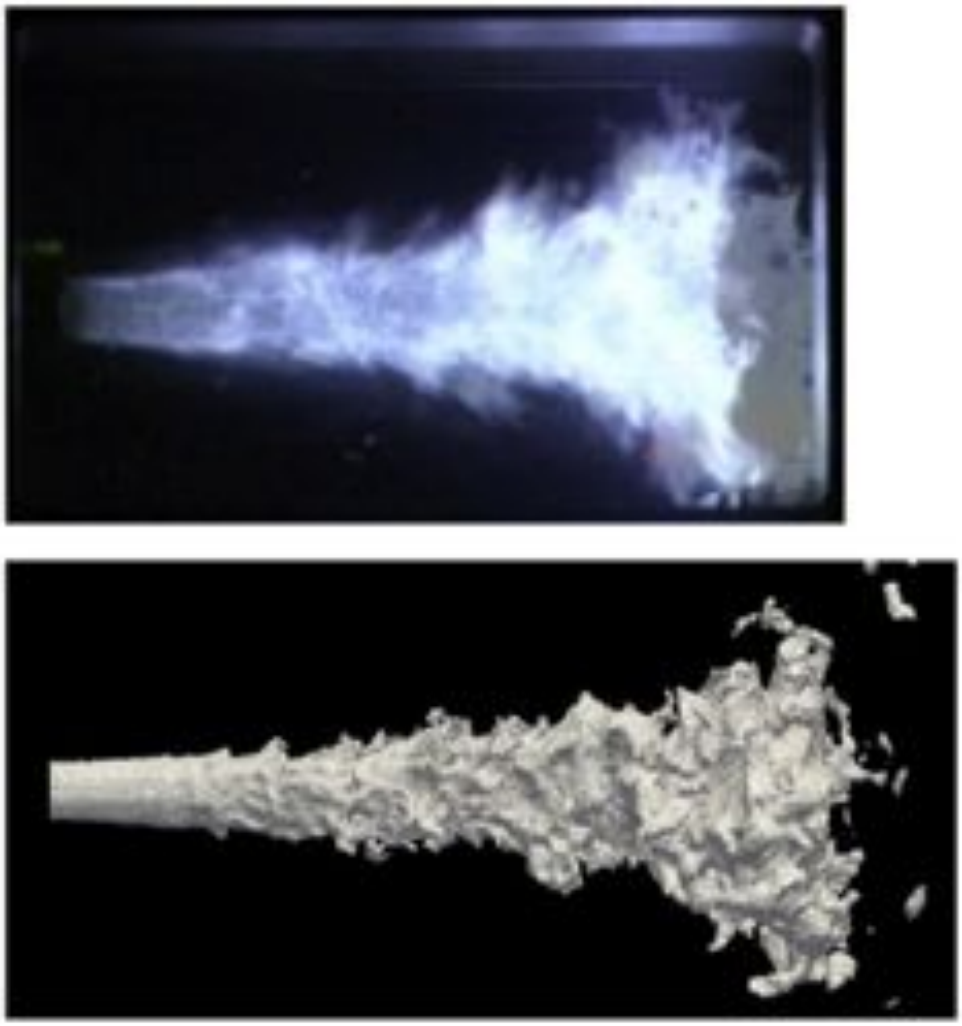

(b)

Figure 1.13: LES computations of transcritical jet flames: (a) $T = 1000$ K iso-surface colored by axial velocity in a reacting transcritical LOx/GH_2 flow [Matsuyama *et al.* 2010]. (b) Visualization of a transcritical LOx/GCH_4 flame: (top) direct visualization from experiment [Singla 2005]; (bottom) $T = (T^{max} + T^{min})/2$ isosurface from LES [Schmitt *et al.* 2010a].

1.3 Study Plan

The objective of the present thesis work is to study the characteristics of reacting flows at operating conditions and in configurations relevant to LREs, with high-fidelity unsteady numerical simulations. Figure 1.14 shows a schematic view of the combustion chamber of a LRE, and the different study levels considered herein.

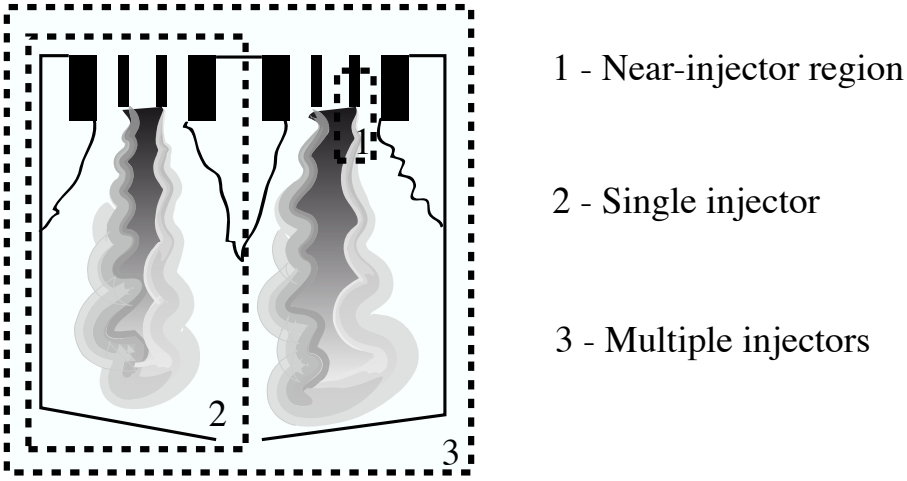

Figure 1.14: Schematic of a LRE combustion chamber, showing the different levels of study considered in the present thesis work.

1 - Near-injector region

In Chap. 3, the stabilization region of a transcritical LOx/GH_2 flame is simulated with Direct Numerical Simulation with an unprecedented spatial resolution. The non-reacting and reacting flow characteristics are compared, and information is provided on the flame stabilization mechanism and on the turbulent flame structure in LREs.

2 - Single injector

In Chap. 4, a transcritical LOx/GH_2 jet flame stabilized at the rim of a coaxial injector, is simulated with LES. The numerical results provide a detailed view of the turbulent mixing process in such a configuration. Then, an important design parameter (the inner recess length of the oxygen tube) is varied and the effects of this parameter on the flame dynamics is investigated. Numerical results are compared with experimental and theoretical results for validation.

3 - Multiple Injectors

A preliminary LES result of a multiple-injector combustor is shown in Chap. 5. The final aim of such configurations is to understand how multiple flames interact under smooth operating conditions or under transverse acoustic waves, as often encountered prior to combustion instability in LREs.

Chapter 2

Governing Equations, Thermodynamics and Numerics

Contents

This chapter presents the conservation equations implemented in the AVBP numerical solver (used in later DNS and LES studies (Sec. 3 to Sec. 5)).

The AVBP solver is co-developed by CERFACS and IFP Energies Nouvelles. It uses unstructured meshes and finite-volume and finite-element high-order schemes to discretize the direct and filtered Navier-Stokes equations in complex geometries for combustion and aerodynamics.

AVBP has been used in many different applications, ranging from gas turbines [Selle *et al.* 2004, Roux *et al.* 2005, Wolf *et al.* 2009] and piston engines [Vermorel *et al.* 2009, Enaux *et al.* 2011], to scramjets [Roux *et al.* 2010]. An overview of the solver properties and some recent industrial applications of AVBP is presented in [Gourdain *et al.* 2009a, Gourdain *et al.* 2009b].

The description of numerical schemes in the unstructured framework is omitted and may be found in the handbook of the AVBP solver [AVBP 2011] or in previous thesis

manuscripts from CERFACS. See [Lamarque 2007, Jaegle 2009, Senoner 2010], among others.

2.1 Navier-Stokes Equations

Throughout this document, it is assumed that the conservation equations for a supercritical fluid flow are similar to a perfect-gas variable-density fluid. The only difference between the two is that they are coupled to different equations of state. This single-phase formulation assumes that surface tension is negligible in front of aerodynamic forces (infinite Weber number), which appears to be an overall-correct approximation in the light of experimental studies of cryogenic flows (see Sec. 1.2.2). However, the fundamental studies of [Giovangigli *et al.* 2011] have shown that even at supercritical pressures, a fluid mixture can be unstable and phase change can still occur in certain cases. There are thus various levels of accuracy in the description of supercritical flows and in a simplified approach, it is assumed here that the supercritical fluid mixture is always stable so that no phase change occur.

Throughout this part, the index notation (Einstein's rule of summation) is adopted for the description of the governing equations. Note however that index k is reserved to refer to the k^{th} species and will not follow the summation rule unless specifically mentioned or implied by the $\sum$ sign.

The set of conservation equations describing the evolution of a compressible flow with chemical reactions reads:

$$\frac{\partial \rho u_i}{\partial t} + \frac{\partial}{\partial x_j}(\rho\, u_i\, u_j) = -\frac{\partial}{\partial x_j}[P\,\delta_{ij} - \tau_{ij}] \tag{2.1}$$

$$\frac{\partial \rho E}{\partial t} + \frac{\partial}{\partial x_j}(\rho\, E\, u_j) = -\frac{\partial}{\partial x_j}[u_i\,(P\,\delta_{ij} - \tau_{ij}) + q_j] + \dot{\omega}_T \tag{2.2}$$

$$\frac{\partial \rho_k}{\partial t} + \frac{\partial}{\partial x_j}(\rho_k\, u_j) = -\frac{\partial}{\partial x_j}[J_{j,k}] + \dot{\omega}_k. \tag{2.3}$$

In equations 2.1 to 2.3, which respectively correspond to the conservation laws for momentum, total energy and species, the following symbols (ρ, u_i, E, ρ_k) denote the density, the velocity vector, the total energy per unit mass ($E = e_c + e$, with e the sensible energy) and the density of the chemical species k: $\rho_k = \rho Y_k$ for $k = 1$ to N (where N is the total number of species); Y_k being the mass fraction of the k^{th} species. P denotes the pressure (see Eq. 2.4.1), τ_{ij} the stress tensor (see Eq. 2.12), q_j the heat flux vector (see Eq. 2.14) and $J_{j,k}$ the vector of the diffusive flux of species k (see Eq. 2.11). The source term in the species transport equations ($\dot{\omega}_k$ in Eq. 2.3) comes from the consumption or production of species by chemical reations. The source term in the total energy equation ($\dot{\omega}_T$ in Eq. 2.2) is the heat release rate, which comes from sensible enthalpy variation associated to species source terms:

$$\dot{\omega}_T = -\sum_{k=1}^{N}(\dot{\omega}_k \Delta h^0_{f,k}) \tag{2.4}$$

with $\Delta h^0_{f,k}$, the mass enthalpy of formation of species k.

The fluxes of the Navier-Stokes equations can be split into two parts:

Inviscid fluxes:

$$\begin{pmatrix} \rho\, u_i\, u_j + P\, \delta_{ij} \\ (\rho E + P\, \delta_{ij})\, u_j \\ \rho_k\, u_j \end{pmatrix} \tag{2.5}$$

Viscous fluxes:

$$\begin{pmatrix} -\tau_{ij} \\ -(u_i\, \tau_{ij}) + q_j \\ J_{j,k} \end{pmatrix} \tag{2.6}$$

2.1.1 Species diffusion flux

In multi-species flows the total mass conservation implies that:

$$\sum_{k=1}^{N} Y_k\, V_i^k = 0 \tag{2.7}$$

where V_i^k are the components in directions (i=1,2,3) of the diffusion velocity of species k. They are often expressed as a function of the species molar concentration gradients using the Hirschfelder-Curtis approximation:

$$X_k\, V_i^k = -D_k \frac{\partial X_k}{\partial x_i}, \tag{2.8}$$

where X_k is the molar fraction of species k: $X_k = Y_k W / W_k$. In terms of mass fraction, the approximation 2.8 may be expressed as:

$$Y_k\, V_i^k = -D_k \frac{W_k}{W} \frac{\partial X_k}{\partial x_i} \tag{2.9}$$

Summing Eq. 2.9 over all k's shows that the approximation 2.9 does not necessarily comply with equation 2.7 that expresses mass conservation. In order to achieve this, a correction diffusion velocity $\vec{V}^c$ is added to the diffusion velocity V_i^k to ensure global mass conservation [Poinsot & Veynante 2005]:

$$V_i^c = \sum_{k=1}^{N} D_k \frac{W_k}{W} \frac{\partial X_k}{\partial x_i} \tag{2.10}$$

and computing the diffusive species flux for each species k as:

$$J_{i,k} = -\rho \left(D_k \frac{W_k}{W} \frac{\partial X_k}{\partial x_i} - Y_k V_i^c \right) \tag{2.11}$$

Here, D_k are the diffusion coefficients for each species k in the mixture (see section 2.1.4). Using equation Eq. 2.11 to determine the diffusive species flux implicitly verifies Eq. 2.7.

2.1.2 Viscous stress tensor

The stress tensor τ_{ij} is given by:

$$\tau_{ij} = 2\mu \left(S_{ij} - \frac{1}{3}\delta_{ij} S_{ll} \right) \tag{2.12}$$

where S_{ij} is the rate of strain tensor and μ is the dynamic viscosity (see section 2.1.4).

$$S_{ij} = \frac{1}{2} \left(\frac{\partial u_i}{\partial x_j} + \frac{\partial u_j}{\partial x_i} \right) \tag{2.13}$$

2.1.3 Heat flux vector

For multi-species flows, an additional heat flux term appears in the diffusive heat flux. This term is due to heat transport by species diffusion. The total heat flux vector then takes the form:

$$q_i = \underbrace{-\lambda \frac{\partial T}{\partial x_i}}_{\text{Heat conduction}} \underbrace{-\rho \sum_{k=1}^{N} \left(D_k \frac{W_k}{W} \frac{\partial X_k}{\partial x_i} - Y_k V_i^c \right) \bar{h}_k}_{\text{Heat flux through species diffusion}} = -\lambda \frac{\partial T}{\partial x_i} + \sum_{k=1}^{N} J_{i,k} \bar{h}_k \tag{2.14}$$

where λ is the heat conduction coefficient of the mixture (see section 2.1.4) and $\overline{h}_k$ the partial-mass enthalpy of the species k [Meng & Yang 2003].

Dufour terms in Eq. 2.14 and Soret terms in Eq. 2.11 have been neglected, because they are thought to be second-order terms for the type of flow investigated here (in a DNS of reacting H_2/O_2, [Oefelein 2006] showed they were negligible in front of the other terms), which would add an unnecessary level of complexity.

2.1.4 Transport coefficients

In CFD codes for perfect-gas multi-species flows the molecular viscosity μ is often assumed to be independent of the gas composition and close to that of air. In that case, a simple power law can approximate the temperature dependency of a gas mixture viscosity.

$$\mu = c_1 \left(\frac{T}{T_{ref}} \right)^b \tag{2.15}$$

with b typically ranging between 0.5 and 1.0. For example $b = 0.76$ for air.

For transcritical combustion, it is not possible to describe the 'liquid-like' viscosity and the 'gas-like' viscosity with the same expression. Instead, the Chung model is used to compute dynamic viscosity as a function of T and ρ_k [Chung *et al.* 1984,Chung *et al.* 1988].

The dynamic viscosity decreases with temperature in a liquid and increases with temperature in a gas. This is illustrated by the evolution of dynamic viscosity and thermal conductivity with temperature at 10 MPa for pure oxygen, as shown in Fig. 2.1. In this figure, the transport coefficients for heat and momentum are computed with the method

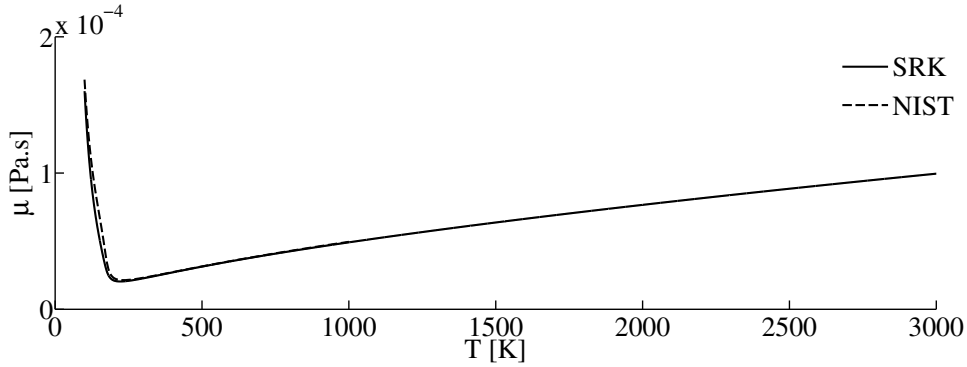

(a)

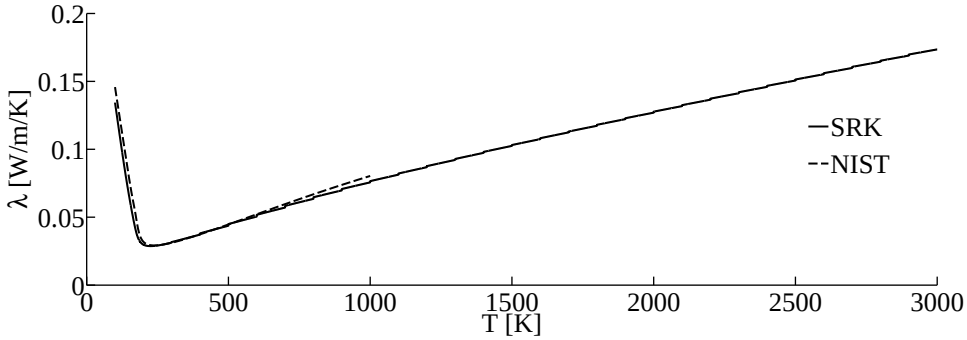

(b)

Figure 2.1: Transport coefficients for O_2 at 100 bar, showing the liquid-like to gas-like transition of thermo-physical properties . a) Dynamic viscosity b) Thermal conductivity.

presented in [Chung *et al.* 1984, Chung *et al.* 1988] which compares favorably to the NIST database [Lemmon *et al.* 2009].

The computation of the species diffusion coefficients D_k is a specific issue. These coefficients should be expressed as a function of the binary coefficients D_{ij} obtained from kinetic theory [Hirschfelder *et al.* 1954]. The mixture diffusion coefficient for species k, D_k, is computed as [Bird *et al.* 1960]:

$$D_k = \frac{1 - Y_k}{\sum_{j \neq k}^{N} X_j / D_{jk}} \tag{2.16}$$

The D_{ij} are functions of collision integrals and thermodynamic variables. In addition to the fact that computing the full diffusion matrix appears to be prohibitively expensive in a multidimensional unsteady CFD computation, there is a lack of experimental data to validate these diffusion coefficients. Therefore, a simplified approximation is used for D_k. The Schmidt numbers $S_{c,k}$ of the species are supposed to be constant so that the binary diffusion coefficient for each species is computed as:

$$D_k = \frac{\mu}{\rho \, S_{c,k}} \tag{2.17}$$

This is a strong simplification of the diffusion coefficients since it is well-known that the Schmidt numbers are not constant in a transcritical flame and can vary within several orders of magnitude between a liquid-like and a gas-like fluid [Oefelein 2006]. Models exist to qualitatively take into account this variation [Hirschfelder *et al.* 1954, Bird *et al.* 1960, Takahashi 1974], although no experimental data is available to validate them. However, the effects of the constant-Schmidt simplification on the flame structure is actually very small, as shown later on in Fig. 3.6, and thus appears to be reasonable for the present studies of combustion.

The diffusion coefficients of heat ($D_{th} = \lambda/\rho C_p$) and momentum ($\nu = \mu/\rho$) are submitted to large variations within the flow field, which have to be taken into account.

Due to the peak of C_p at the pseudo-boiling point, heat diffusivity is lower than species diffusivity, as shown in Fig. 2.2. The Lewis numbers ($Le_k = D_{th}/D_k$) are below one, and species gradients are likely to be smaller than temperature gradients in a transcritical mixing layer.

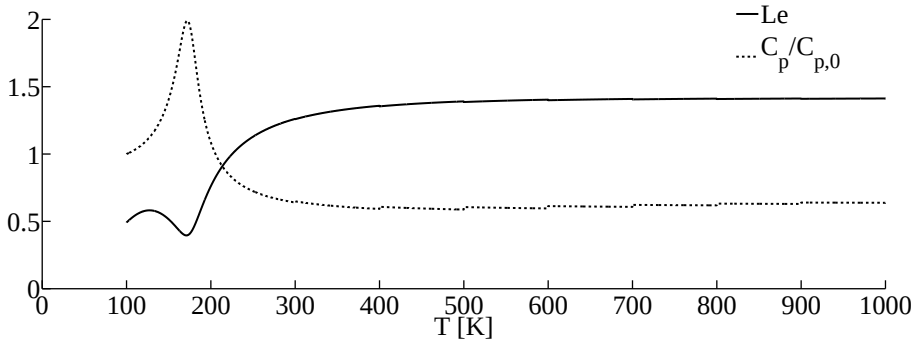

Figure 2.2: Evolution of the Lewis number and normalized heat capacity with temperature. $C_{p,0} = 1700$ J/K/kg. The peak of C_p at the pseudo-boiling point creates a local minimum in the Lewis number.

2.2 Filtered Equations for LES

The idea of Large-Eddy Simulation (LES) is to solve the filtered Navier-Stokes equation, modeling the small scales of turbulence, which are assumed to have a mere dissipation role of the turbulent kinetic energy. The derivation of the LES equations starts with the introduction of filtered quantities.

The filtered quantity $\overline{f}$ is resolved in the numerical simulation whereas the subgrid-scales $f' = f - \overline{f}$ are modeled. For variable density ρ, a mass-weighted Favre filtering of f is introduced such as:

$$\overline{\rho}\widetilde{f} = \overline{\rho f} \tag{2.18}$$

The conservation equations for LES are obtained by filtering the instantaneous equations 2.1, 2.2 and 2.3:

$$\frac{\partial \overline{\rho}\,\widetilde{u_i}}{\partial t} + \frac{\partial}{\partial x_j}(\overline{\rho}\,\widetilde{u_i}\,\widetilde{u_j}) = -\frac{\partial}{\partial x_j}[\overline{P}\,\delta_{ij} - \overline{\tau_{ij}} - \overline{\tau_{ij}}^t] \tag{2.19}$$

$$\frac{\partial \overline{\rho}\,\widetilde{E}}{\partial t} + \frac{\partial}{\partial x_j}(\overline{\rho}\,\widetilde{E}\,\widetilde{u_j}) = -\frac{\partial}{\partial x_j}[\overline{u_i\,(P\,\delta_{ij} - \tau_{ij})} + \overline{q_j} + \overline{q_j}^t] + \overline{\dot{\omega}_T} \tag{2.20}$$

$$\frac{\partial \overline{\rho}\,\widetilde{Y_k}}{\partial t} + \frac{\partial}{\partial x_j}(\overline{\rho}\,\widetilde{Y_k}\,\widetilde{u_j}) = -\frac{\partial}{\partial x_j}[\overline{J_{j,k}} + \overline{J_{j,k}}^t] + \overline{\dot{\omega}_k} \tag{2.21}$$

In equations 2.19, 2.20 and 2.21, there are now four types of terms to be distinguished: inviscid fluxes, viscous fluxes, source terms and subgrid-scale terms.

In this section, the subgrid-scale models for heat, mass and momentum fluxes are assumed to bear the same form as in the perfect-gas case.

Inviscid fluxes:

These terms are equivalent to the unfiltered equations except that they now contain filtered quantities:

$$\begin{pmatrix} \overline{\rho}\widetilde{u_i}\,\widetilde{u_j} + \overline{P}\,\delta_{ij} \\ \overline{\rho}\widetilde{E}\widetilde{u_j} + \overline{P\,u_j}\delta_{ij} \\ \overline{\rho}_k\widetilde{u_j} \end{pmatrix} \tag{2.22}$$

Viscous fluxes:

The viscous terms take the form:

$$\begin{pmatrix} -\overline{\tau_{ij}} \\ -(\overline{u_i\,\tau_{ij}}) + \overline{q_j} \\ \overline{J_{j,k}} \end{pmatrix} \tag{2.23}$$

Filtering the balance equations leads to unclosed quantities, which need to be modeled, as presented in Sec. 2.2.2.

Subgrid-scale turbulent fluxes:
The subgrid-scale fluxes are:

$$\begin{pmatrix} -\overline{\tau_{ij}}^t \\ \overline{q_j}^t \\ \overline{J_{j,k}}^t \end{pmatrix} \tag{2.24}$$

2.2.1 The filtered viscous terms

The laminar filtered stress tensor $\overline{\tau_{ij}}$ is given by the following relations (see [Poinsot & Veynante 2005]):

$$\begin{aligned} \overline{\tau_{ij}} &= \overline{2\mu(S_{ij} - \tfrac{1}{3}\delta_{ij}S_{ll})}, \\ &\approx 2\overline{\mu}(\widetilde{S}_{ij} - \tfrac{1}{3}\delta_{ij}\widetilde{S}_{ll}), \end{aligned} \tag{2.25}$$

and

$$\widetilde{S}_{ij} = \frac{1}{2}(\frac{\partial \widetilde{u}_i}{\partial x_j} + \frac{\partial \widetilde{u}_j}{\partial x_i}), \tag{2.26}$$

The filtered diffusive species flux vector is:

$$\begin{aligned} \overline{J_{i,k}} &= -\overline{\rho\left(D_k \tfrac{W_k}{\overline{W}} \tfrac{\partial X_k}{\partial x_i} - Y_k V_i^c\right)} \\ &\approx -\overline{\rho}\left(\overline{D}_k \tfrac{W_k}{\overline{W}} \tfrac{\partial \widetilde{X}_k}{\partial x_i} - \widetilde{Y}_k \widetilde{V}_i^c\right), \end{aligned} \tag{2.27}$$

where higher order correlations between the different variables of the expression are assumed negligible.

The filtered heat flux is :

$$\begin{aligned} \overline{q_i} &= -\overline{\lambda \tfrac{\partial T}{\partial x_i}} + \textstyle\sum_{k=1}^{N} \overline{J_{i,k} h_k} \\ &\approx -\overline{\lambda} \tfrac{\partial \overline{T}}{\partial x_i} + \textstyle\sum_{k=1}^{N} \overline{J_{i,k}}\, \widetilde{h}_k \end{aligned} \tag{2.28}$$

These forms assume that the spatial variations of molecular diffusion fluxes are negligible and can be modeled through simple gradient assumptions.

2.2.2 Subgrid-scale turbulent terms for LES

As highlighted above, filtering the transport equations yields a closure problem, which requires modeling of the Subgrid-Scale (SGS) turbulent fluxes (see Eq. 2.2).

The Reynolds tensor is :

$$\overline{\tau_{ij}}^t = -\overline{\rho}\,(\widetilde{u_i u_j} - \widetilde{u}_i \widetilde{u}_j) \tag{2.29}$$

where $\overline{\tau_{ij}}^t$ is modeled with the *turbulent-viscosity hypothesis* (or Boussinesq's hypothesis):

$$\overline{\tau_{ij}}^t = 2\,\overline{\rho}\,\nu_t \left(\widetilde{S}_{ij} - \frac{1}{3}\delta_{ij}\widetilde{S}_{ll}\right), \tag{2.30}$$

which relates the SGS stresses to the filtered rate of strain, mimicking the relation between stress and rate of strain (see Eq. 2.12). Models for the SGS turbulent viscosity ν_t are presented in Sec. 2.3.

The subgrid-scale diffusive species flux vector is:

$$\overline{J_{i,k}}^t = \overline{\rho}\left(\widetilde{u_i Y_k} - \widetilde{u}_i \widetilde{Y}_k\right), \tag{2.31}$$

$\overline{J_{i,k}}^t$ is modeled with a gradient-diffusion hypothesis:

$$\overline{J_{i,k}}^t = -\overline{\rho}\left(D_k^t \frac{W_k}{\overline{W}} \frac{\partial \widetilde{X}_k}{\partial x_i} - \widetilde{Y}_k \widetilde{V}_i^{c,t}\right), \tag{2.32}$$

with

$$D_k^t = \frac{\nu_t}{S_{c,k}^t} \tag{2.33}$$

The turbulent Schmidt number $S_{c,k}^t = 0.6$ is the same for all species. The turbulent correction velocity reads:

$$\widetilde{V}_i^{c,t} = \sum_{k=1}^{N} \frac{\mu_t}{\overline{\rho} S_{c,k}^t} \frac{W_k}{\overline{W}} \frac{\partial \widetilde{X}_k}{\partial x_i}, \tag{2.34}$$

with $\nu_t = \mu_t/\overline{\rho}$.

The subgrid-scale heat flux vector is:

$$\overline{q_i}^t = \overline{\rho}(\widetilde{u_i E} - \widetilde{u}_i \widetilde{E}), \tag{2.35}$$

where E is the total energy. The SGS turbulent heat flux $\widetilde{q}^t$ also bears the same form as its molecular counterpart (see Eq. 2.14):

$$\overline{q_i}^t = -\lambda_t \frac{\partial \widetilde{T}}{\partial x_i} + \sum_{k=1}^{N} \overline{J_{i,k}}^t \widetilde{h}_k, \tag{2.36}$$

with

$$\lambda_t = \frac{\mu_t \overline{C_p}}{P_r^t}. \tag{2.37}$$

The turbulent Prandtl number P_r^t is set to a constant value of 0.6.

The correction velocity for laminar diffusion then reads:

$$\widetilde{V}_i^{c} = \sum_{k=1}^{N} \frac{\overline{\mu}}{\overline{\rho} S_{c,k}} \frac{W_k}{\overline{W}} \frac{\partial \widetilde{X}_k}{\partial x_i.} \tag{2.38}$$

2.3 Models for the subgrid-stress tensor

Models for the subgrid-scale turbulent viscosity ν_t are an essential part of a LES. The SGS turbulence models are derived on the theoretical ground that the LES filter is spatially and temporally invariant. Variations in the filter size due to non-uniform meshes are not directly accounted for in the LES models. Change of cell topology is only accounted for through the use of the local cell volume, that is $\triangle = V_{cell}^{1/3}$.

2.3.1 Smagorinsky model

In the Smagorinsky model, the SGS viscosity ν_t is obtained from

$$\nu_t = (C_S \triangle)^2 \sqrt{2\, \widetilde{S}_{ij}\, \widetilde{S}_{ij}} \tag{2.39}$$

where C_S is the model constant set to 0.18 but can vary between 0.1 and 0.18 depending on the flow configuration. The Smagorinsky model [Smagorinsky 1963] was developed in the 1960s and heavily tested for multiple flow configurations. This closure is characterized by its globally correct prediction of kinetic energy dissipation in homogeneous isotropic turbulence. However, it predicts non-zero turbulent viscosity levels in flow regions of pure shear, which makes it unsuitable for many wall-bounded flows [Nicoud & Ducros 1999]. This also means that it is also too dissipative in transitioning flows [Sagaut 2002], such as turbulent jets.

2.3.2 WALE model

In the WALE model, the expression for ν_t takes the form:

$$\nu_t = (C_w \triangle)^2 \frac{(s_{ij}^d s_{ij}^d)^{3/2}}{(\widetilde{S}_{ij}\widetilde{S}_{ij})^{5/2} + (s_{ij}^d s_{ij}^d)^{5/4}} \tag{2.40}$$

with

$$s_{ij}^d = \frac{1}{2}\,(\widetilde{g_{ij}}^2 + \widetilde{g_{ji}}^2) - \frac{1}{3}\,\widetilde{g_{kk}}^2\,\delta_{ij} \tag{2.41}$$

$C_w = 0.4929$ is the model constant and $\widetilde{g}_{ij}$ denotes the resolved velocity gradient. The WALE model [Nicoud & Ducros 1999] was developed for wall bounded flows and allows to obtain correct scaling laws near the wall in turbulent flows. This model allows the transitioning of shear flows in LES.

2.4 Real-Gas Thermodynamics

The AVBP solver first have been adapted to the real-gas framework in [Schmitt 2009]. The thermodynamic derivations have been rephrased following [Meng & Yang 2003] and are synthesized herein. The advantage of the current formulation is that all partial derivatives are directly expressed as a function of transported variables, such as $\rho_k = \rho Y_k$ instead of molar or mass fractions.

2.4.1 Generalized Cubic Equation of State

Due to their computational efficiency, *cubic equation of states* have been chosen for implementation in the AVBP code. They allow a good overall description of supercritical fluid thermodynamics, although they are less accurate than more complex Equations Of States (EOSs) such as Benedict-Webb-Rubin (BWR) [Benedict *et al.* 1942]. However, the BWR EOS is mathematically uneasy to handle, and requires numerical approximations of the partial pressure derivatives used in a CFD code. The Soave-Redlich Kwong (SRK) [Soave 1972] and the Peng-Robinson (PR) [Peng & Robinson 1976] EOSs are widely used in the supercritical CFD community. They are very similar and can be written in the following generic form:

$$P = \frac{RT}{v-b} - \frac{\theta(T)}{v^2 + d_1 b v + d_2 b^2} \tag{2.42}$$

$$\text{PR} : (d_1, d_2) = (2,\, -1) \tag{2.43}$$

$$\text{SRK} : (d_1, d_2) = (1,\, 0) \tag{2.44}$$

where P is the pressure, T the temperature, v the molar volume ($v = W/\rho$), $\theta(T)$ and b are parameters computed with respect to the critical points ($T_{c,i}$, $P_{c,i}$) of the species contained in the mixture and their acentric factor ω_i. In order to simplify further derivations, the polynomial $D(v)$ is defined as:

$$D(v) = v^2 + d_1 b v + d_2 b^2, \tag{2.45}$$

and the EOS now reads:

$$P = \frac{RT}{v-b} - \frac{\theta(T)}{D(v)} \tag{2.46}$$

2.4.2 Primitive to conservative variables

The description of an initial solution for the conservation equations is generally easier with primitive variables (T,P,Y_k, u_i), whereas conservative variables are needed (ρE, ρ_k, ρ, ρu_i). Thus, the density and energy needs to be computed from the primitive variables, using the EOS.

Density ρ from (T, P, Y_k)

If Eq. 2.46 is multiplied by $(v-b)$ and $D(v)$, a cubic polynome in v appears (this is why these EOS are named *cubic*):

$$\begin{aligned} a_3 v^3 + a_2 v^2 + a_1 v + a_0 &= 0 \qquad (2.47)\\ \text{with } a_0 &= -b\left[\theta + (RT - b)\, d_2 b\right] \\ a_1 &= P d_2 b^2 - (RT - b)\, d_1 b + \theta \\ a_2 &= P d_1 b - (RT - b) \\ a_3 &= P \end{aligned}$$

The roots of this polynomial are found analytically, using Cardan's formula. This formula is derived in Appendix A.1. The molar volume is determined and the density is deduced as:

$$\rho = \frac{W}{v} \tag{2.48}$$

The SRK and PR EOSs are used to compute the density of oxygen at 10 MPa as a function of temperature, and are compared to the NIST database [Lemmon *et al.* 2009] in Fig. 2.3. The pseudo-boiling temperature (see Eq. 1.1) is $T_{pb} = 172$ K and is identified by a circle on Fig. 2.3. The SRK EOS is more accurate for $T < T_{pb}$ whereas the PR EOS is better for $T >= T_{pb}$. Thus, depending on the configuration, one EOS can be better suited than the other. The PR EOS is chosen to accurately predict transcritical densities in the DNS studies of Chap. 3. In Chap. 4, the SRK EOS is chosen to accurately predict the injection densities far below T_{pb}, giving more realistic injection velocities when imposing the mass flow rate of reactants.

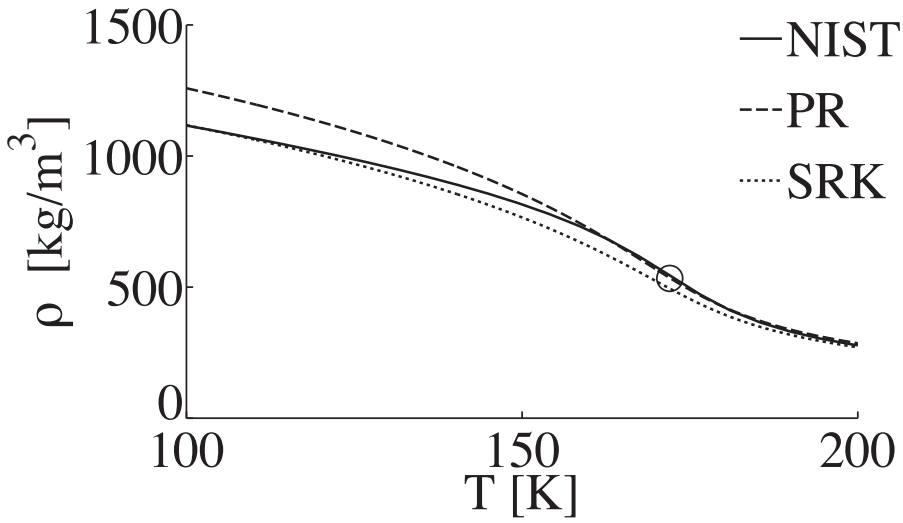

Figure 2.3: Density of oxygen as a function of temperature, at 10 MPa, computed with the Peng-Robinson and the Soave-Redlich-Kwong equations of state, and compared to the NIST database [Lemmon *et al.* 2009]. The circle at $T = 172$ K shows the pseudo-boiling point.

2.5 CPU cost

In order to obtain converged flow statistics in DNS and LES, a "sufficient time period" should be simulated, which is related to the time needed for the fluid to flow through the region of interest:

$$T_{ft} = \frac{L}{U} \tag{2.49}$$

with L the length of the region of interest and U a characteristic convection velocity. In practice, 5 to 10 flow-through times are needed to obtain converged statistics.

Then, the simulation time step dt determines how many temporal iterations $N_{n,ft}$ are needed to simulate the fluid flow during n T_{ft}:

$$N_{n,ft} = n \ \frac{T_{ft}}{dt} \tag{2.50}$$

The efficiency of a CFD solver can be measured with the time needed for a CPU to compute a temporal iteration per grid point. The order of magnitude of the CPU cost per iteration and per node of the AVBP solver is: $C_{i,n} = 100 \ \mu s$.

Thus the computational cost of an unsteady numerical simulation is:

$$C = N_{n,ft} \ N_{nodes} \ C_{i,n} \tag{2.51}$$

When a mesh is homogeneously refined by a factor of two in each direction, the number of nodes increases by a factor of $2^{n_{dim}}$ and the time step decreases by a factor of 2. Thus, the total CPU cost of a simulation increases by a factor of $2^{n_{dim}+1}$. This increased cost should always be kept in mind when conducting mesh convergence studies of unsteady simulations.

Chapter 3

A DNS study of turbulent mixing and combustion in the near-injector region of Liquid Rocket Engines

Contents

In the presence of high convection speeds inside the combustion chamber of a Liquid Rocket Engine (LRE), it is crucial that the flames stay anchored at the injector rim, to prevent blow-off and extinction. Understanding the flame stabilization mechanisms

is thus important for the design of rocket engines. The literature on flame stabilization is extremely large, with detailed investigations using both experiments and numerical simulations. The main parameter characterizing flame stabilization is the distance from the injector to the flame front, and a wide variety of phenomena have been reported with chemistry, transport and various sources of heat losses, possibly playing an important role.

In the pioneering numerical work of [Oefelein & Yang 1998,Oefelein 2001,Oefelein 2005, Oefelein 2006], important features of the flame stabilization mechanism in the context of LREs have been identified. For instance, it has been shown that the unsteady stagnation point behind the lip of a coaxial injection contains recirculated fuel-rich combustion products that supply heat to the flame tip and help stabilization.

However, there are still uncertainties on the flame stabilization mechanisms. Indeed, experimental studies of transcritical jet flames [Singla *et al.* 2005, Singla *et al.* 2007] have shown that the flame is stabilized at a small but finite distance from the injector rim, which indicates the presence of partial premixing. It is argued in [Oefelein 2005] that heat loss from the flame to the injector wall could provoke flame quenching in the experimental studies, which is not taken into account in the numerical simulations.

In addition, turbulent mixing processes in supercritical flows are not well known and understood, in particular, because their experimental observation is not easy. Therefore, it is proposed here to conduct a DNS of turbulent flame stabilization in conditions of LRE. The main objective is to clarify the discrepancies on flame stabilization distance mentioned above. Mixing and combustion regimes will be scrutinized in fully resolved simulations and driving mechanisms will be determined. This will also help to identify paths for improvement of turbulent mixing and combustion models for LES.

3.1 Configuration

The configuration chosen for the DNS study corresponds to a 2D cut through a LOx/GH_2 coaxial injector, representative of an injector of a LRE:

- the ambient pressure is high: $P = 10$ MPa, about twice as much as the critical point of O_2 (5.04 MPa)
- the inner dense oxygen jet has a low velocity
- the outer light hydrogen jet has a large velocity. The large shear, induced by the velocity difference between the jets, enhances strong turbulent mixing.
- the dimensions of the injector are small (a few millimeters), with a lip height of $h = 0.5$ mm.
- the inner O_2 tube is recessed from the injection plane, to enhance turbulent mixing.

A sketch of the computational domain is displayed in Figs. 3.1 a) and b).

This configuration is inspired from the previous numerical work of [Oefelein & Yang 1998, Oefelein 2005]. The chosen thermodynamic conditions (transcritical injection) are also

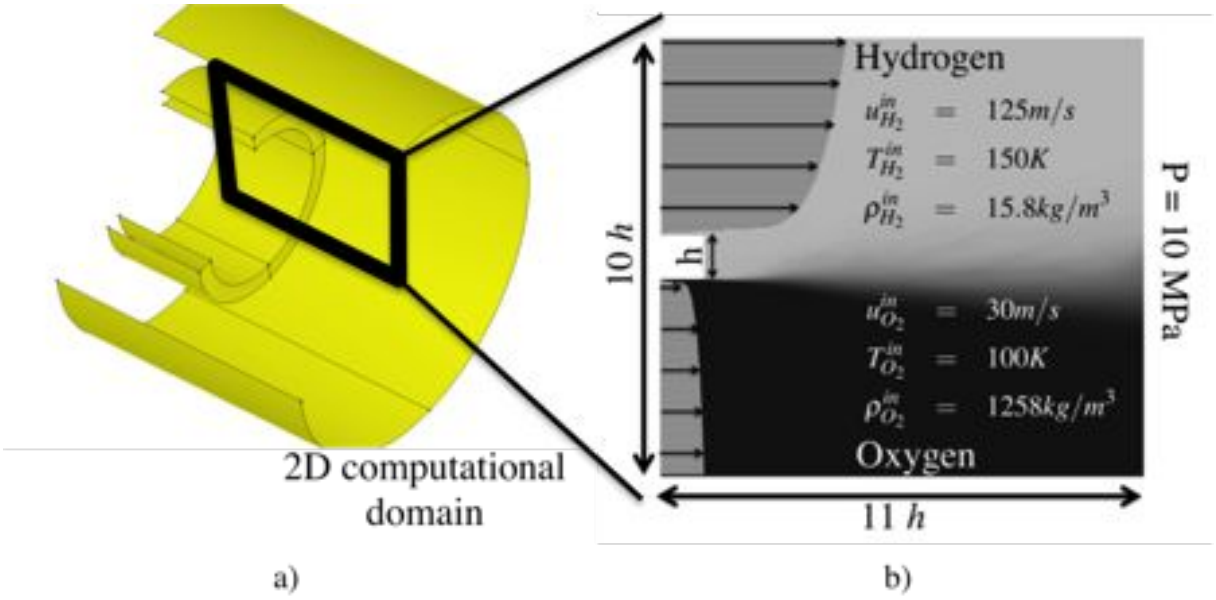

Figure 3.1: a) Typical coaxial injector of a LRE. b) Boundary conditions for the 2D computational domain

close to the experimental study of transcritical LOx/LCH_4 combustion from [Singla *et al.* 2007], and will enable a qualitative comparison with experimental data in Sec. 3.3.5. In [Zong & Yang 2006, Zong & Yang 2007], a supercritical LOx/LCH_4 coaxial flow with the same injection conditions as [Singla *et al.* 2007] has been studied. The present results will also be compared with this numerical work.

3.1.1 Thermodynamics

Cold flow case

Real-gas thermodynamics is accounted for through the PR EOS [Peng & Robinson 1976] (see Sec. 2.4.1) while transport coefficients are modeled based on the theory of corresponding states for the dynamic viscosity and the thermal conductivity (see Sec. 2.1.4) and constant Schmidt numbers (see Tab. 3.1). This overall numerical and modeling methodology has already been validated for non reacting flows [Schmitt *et al.* 2010b].

Reacting flow case

The critical-point coordinates of the combustion intermediate species OH, O, H, H_2O_2 and HO_2, for which no experimental data is available, is estimated using the Lennard-Jones potential-well depth σ_i, and the molecular diameter ϵ_i of the i-th species from the CHEMKIN transport coefficients of the San Diego Mechanism, according to the following

expression [Giovangigli *et al.* 2011]:

$$V_{c,i} = 3.29 N \sigma_i^3 \tag{3.1}$$

$$T_{c,i} = 1.316 \frac{\epsilon_i}{k} \tag{3.2}$$

$$\tag{3.3}$$

where N is the Avogadro number and k is the Boltzmann constant. The acentric factor ω_{ac} is set to zero for radical species. The numerical values for all species are summarized in Tab. 3.1.

Parameters	H_2	O_2	H_2O	O	H	OH	H_2O_2	HO_2
$T_{c,i}$ (K)	33	154.581	647.096	105.28	190.82	105.28	141.34	141.34
$P_{c,i}$ (MPa)	1.2838	5.0430	22.064	7.0882	31.013	7.0883	4.7861	4.7861
$V_{c,i}$ (cm^3/mol)	64.284	73.368	55.948	41.205	17.069	41.205	81.926	81.926
ω_{ac}	-0.216	0.0222	0.3443	0.0	0.0	0.0	0.0	0.0
Schmidt Number	0.28	0.99	0.77	0.64	0.17	0.65	0.65	0.65

Table 3.1: Species critical-point properties (temperature T, pressure P, molar volume V and acentric factor ω) and Schmidt numbers.

3.1.2 Boundary Conditions

The boundary conditions are represented on Fig. 3.1 b). A $1/7^{th}$ power law for the inlet boundary condition is used to mimic the mean turbulent velocity profile in a pipe flow:

$$u(y) = U^{inj} \left(\frac{y - y_{wall}}{4.5h} \right)^{1/7} \tag{3.4}$$

with U^{inj}, the bulk injection velocity (see Tab. 3.2) and $y - y_{wall}$, the distance to the injector wall.

The outlet pressure is imposed at 10 MPa, using the NSCBC formalism [Poinsot & Lele 1992, Baum *et al.* 1994] and accounts for both real-gas effects [Okong'o & Bellan 2002a] and transverse terms [Granet *et al.* 2010].

A $1h$-long sponge layer is placed at the exit of the computational domain, to prevent spurious acoustic wave generation due to the outgoing hydrodynamic structures. This makes the computational domain very compact ($10h \times 11h$) and results in a moderate CPU cost for the simulations (see Sec. 3.1.4).

The upper and lower boundaries are slipping walls while the splitter plate is an adiabatic no-slip wall.

No synthetic turbulence is added to the inflow boundary conditions, and yet, strong turbulence levels caused by vortex shedding are observed downstream the lip. This allows the development of a turbulent mixing layer and strong flame/turbulence interactions in the reacting case. It is believed that this 2D phenomenon (vortex shedding at the lip) drives the flame turbulence interaction, which justifies the 2D nature of the present computations.

3.1.3 Characteristic Numbers and Reference Scales

The main scales and non-dimensional numbers characterizing the flow are summarized in Tab. 3.2, where τ_R and Π_R (defined in Eqs. 1.9 and 1.10) are the reduced temperature and pressure, respectively.

	T [K]	ρ^{inj} [kg/m^3]	U^{inj} [m/s]	μ [Pa.s]	τ_R	Π_R	Re	Ma
O_2	100	1258	30	3.9 10^{-4}	0.65	2.0	9 10^5	0.04
H_2	150	15.8	125	5.1 10^{-6}	4.55	7.8	2 10^5	0.12

R_ρ	R_u	J
80	4	0.2

U_{conv} $[m/s]$	τ_{conv} $[\mu s]$	T_{ft} $[\mu s]$
39.6	12.5	125

Table 3.2: Characteristic flow quantities

A transcritical injection has been chosen ($\tau_R < 1$ at injection) to mimic realistic the injection conditions of a LRE. The resulting density ratio R_ρ (see Eq. 1.14) is very large and plays an important role in the turbulent mixing characteristics.

The PR EOS is chosen to accurately predict densities around and above the pseudo-boiling temperatures (see Fig. 2.3) that are encountered in the reacting case.

The momentum-flux ratio J, defined in Eq. 1.15, is much lower than typical LRE values, where J lies between 1 and 20. This stems from the high velocity of oxygen, which would be lower in a real LRE. However, this change of velocity lowers the computational cost to reach statistical convergence, by lowering the flow-through time, without dramatically changing the characteristic numbers. Indeed, with a more realistic momentum-flux ratio of 2, the oxygen velocity would be 3 m/s, which would result in a low Mach number of 0.004 and a large Reynolds number of 9 10^4.

The Mach number is rather small in both the LOx and GH_2 stream. Even in the reacting case, the Mach number stays below 0.2 so that compressibility effects are small.

The convective velocity of the coherent structures in the flow can be evaluated using the expression given in [Papamoschou & Roshko 1988] and also used for instance in [Raynal 1997]:

$$U_{conv} = \frac{U_{O_2}^{inj} + \left(\frac{\rho_{H_2}}{\rho_{O_2}}\right)^{1/2} U_{H_2}^{inj}}{1 + \left(\frac{\rho_{H_2}}{\rho_{O_2}}\right)^{1/2}} \tag{3.5}$$

This formula is derived with the assumption that in the moving reference frame of the shed vortices, a stagnation point exists between the two streams. Thus, using the Bernoulli formula, with equal dynamic pressures at the stagnation point, the above relation is deduced. This relation appears to be valid for the low Mach number considered herein, where compressibility effects are negligible.

This convective velocity, is used in conjunction with the splitter plate height h, to define a convective time:

$$\tau_{conv} = \frac{h}{U_{conv}} \tag{3.6}$$

3.1.4 Computational Grid

In the cold flow case, the main phenomenon to capture is the turbulent mixing of the two separated streams behind the lip, due to vortex shedding in the lip wake. In the hot flow case, the vortex shedding imposes a large and variable strain on the flame and the computational domain was successively refined in order to obtain at least 5 points in the radical species profile in the most stretched regions of the flame, ensuring a proper discretization of both the flame and the turbulence, leading to a mesh resolution of $\Delta = h/500$ ($= 1$ μm) This fine resolution is applied in a layer containing the lip wake, over a $3h$ vertical extent. Outside this zone, a transverse stretching factor of 1.02 is employed. The mesh finally contains 13.5 million nodes and quadrilaterals. As a comparison with previous efforts to compute such configurations [Oefelein 2005], the resolution is ten times greater.

The integral length scale is of the order of $l_t = h$ and the velocity fluctuations in the cold flow case are of the order of $u' = 0.3\ U_s$ (see Fig. 3.23). Using the kinematic viscosity of the hydrogen stream and assuming a fully developed 3D turbulent flow, the scale separation is:

$$\begin{aligned} \eta &= l_t\ Re_t^{-3/4} \\ &= 0.16\ 10^{-6}\ m \end{aligned} \tag{3.7}$$

Thus, $\eta \approx dx/6$. Since the present computation is 2D, there is no theoretical expression for scale separation, and the expression of scale separation is only used to assess spatial resolution requirements. Due to the high precision of the current numerical scheme, the mesh spacing does not need to be equal to the Kolmogorov scale but simply needs to be O(η) [Moin & Mahesh 1998], which is the case here. It is also checked *a posteriori* in Fig. 3.16 that no energy packs up at large wave numbers, which indicates that either turbulence has not yet developed, or that it has been dissipated by viscous forces at small resolved scales.

In order to compare cold and hot flow simulations, the same mesh was used for both cases.

Probe location

Fig. 3.2 shows the location of probes placed in the computational domain, which enable a time resolved analysis of all turbulent scales. The probe arrangement is a grid within the mixing layer.

3.1.5 Numerical Scheme

The compressible Navier-Stokes equations are solved using the AVBP code presented in Sec. 2. The TTG4A scheme is used in the cold and hot flow cases. This scheme is third

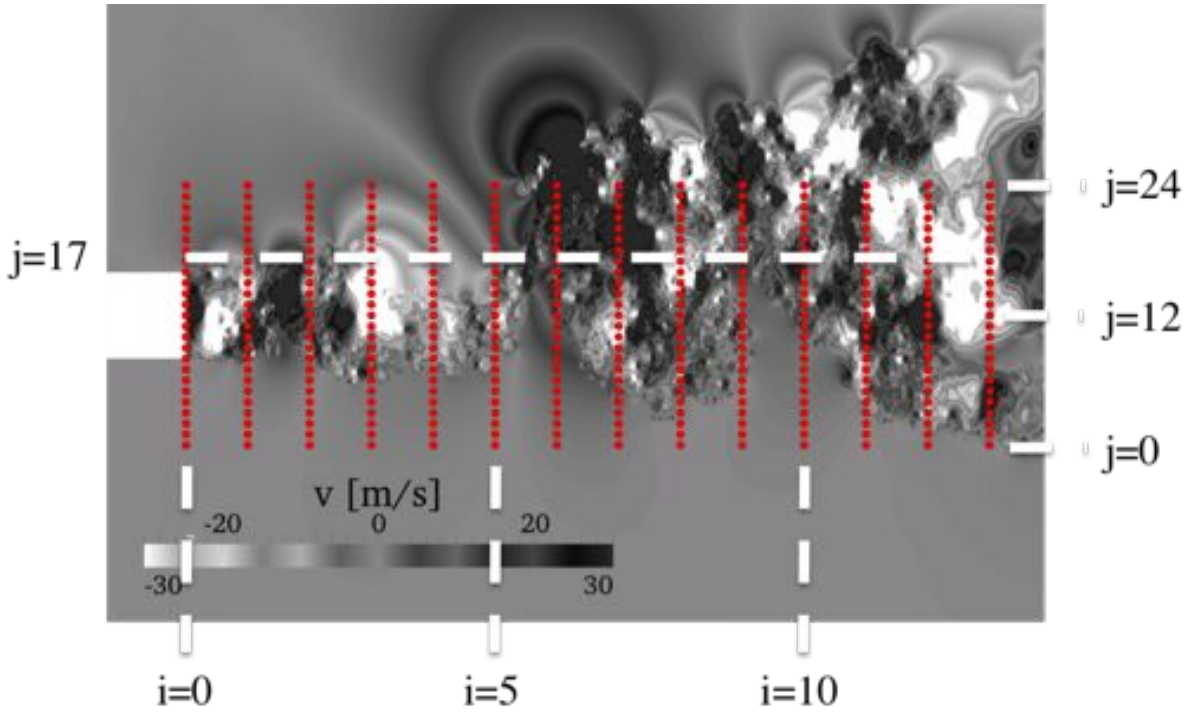

Figure 3.2: Probes located in the mixing layer.

order accurate in space and time. The transcritical density gradient requires numerical stabilization and artificial dissipation is added in this region, using the real-gas operator described in [Schmitt 2009]. The mesh convergence study conducted in Sec. 3.2.5 allows to verify *a posteriori* that numerical stabilization of the transcritical density gradient does not have an impact on the time-average solution and RMS fluctuations.

CPU cost

Using the length of the mixing layer $L = 10\ h$ in Eq. 2.49, the flow-through time of coherent structures is $T_{ft} = 125\ \mu$s (using Eq. 3.5).

In the non-reacting case and the reacting case, the time step is approximately $dt = 0.5\ 10^{-9} s$ and $dt = 0.3\ 10^{-9}\ s$, respectively. A total of $2\ 10^6$ temporal iterations were simulated in both cases, which corresponds to 8 T_{ft} and 5 T_{ft} for the non-reacting case and reacting case, respectively (see Eq. 2.50). These simulations have been conducted on the JADE supercomputer at CINES (Intel Quad-Core at 2.8 GHz), where the efficiency of AVBP is $C_{i,n} = 15\ \mu$s for the non-reacting case (2 species are transported) and $C_{i,n} = 45\ \mu$s for the reacting case (8 reacting species are transported). Thus, the simulation cost is approximately $100\ 10^3$ CPU hours and $300\ 10^3$ CPU hours for the non-reacting and reacting case, respectively.

3.1.6 Initial conditions

Both initial conditions for the non-reacting and reacting cases are described in this section.

Cold flow case

The initial solution is chosen to minimize the convergence time, using the boundary conditions swept through the whole domain. A hyperbolic tangent profile for the O_2 mass fraction and for the temperature is used behind the splitter plate, along with a zero velocity zone, as shown in Fig. 3.3. The thickness of the hyperbolic tangent profile is $\delta = h/4$, so that the oxygen and temperature gradient thicknesses are initially resolved on more than 100 grid points, and yet are steep enough to trigger the flow transition.

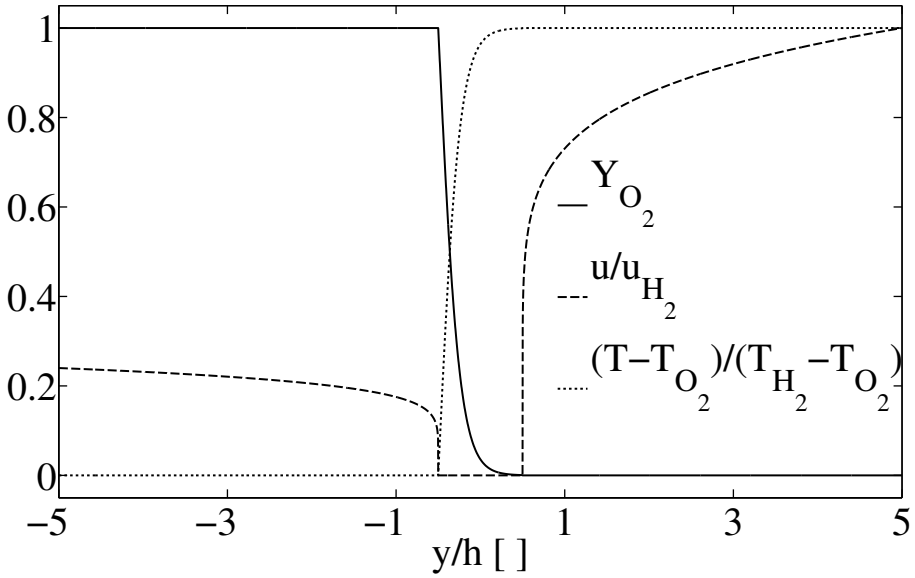

Figure 3.3: Transverse cut through the initial solution of the cold flow, downstream the lip.

Reacting flow case

Combustion is initiated in the computational domain with the following procedure:

1. first, the field of mixture fraction is computed from a non-reacting established flow,
2. then, the flame structure from a laminar diffusion flame is applied onto this field with subsequent replacement of the composition and temperature.

During this procedure, the cold-flow pressure and velocity fields are not altered. As expected, significant acoustic perturbations are generated when the flow adapts from the approximated to the exact solution of the conservation equations. However, the procedure is successful because the pressure waves eventually leave the computational domain and a stable combustion regime is reached, as shown in Fig. 3.4.

3.1.7 Chemical kinetics

The combustion of hydrogen and oxygen is modeled using a detailed scheme accounting for 8 species and 12 reactions [Boivin *et al.* 2011], which is derived from the San Diego

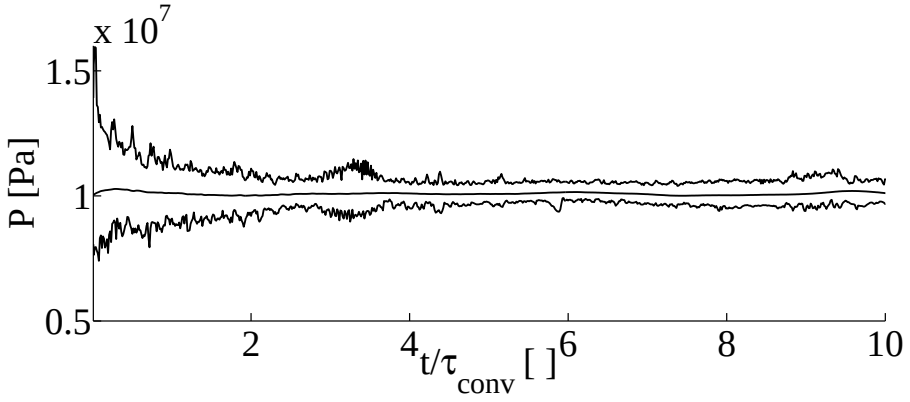

Figure 3.4: Temporal evolution of the minimum, mean and maximum pressures in the computational domain, after instantaneous ignition of the cold flow case.

mechanism [Petrova & Williams 2006]. The forward rate coefficients are given in Tab. 3.3. The backward reaction rates are classically computed using low-pressure entropy and enthalpy NIST/JANAF tables [Lemmon *et al.* 1998]. A more general treatment of the

	Reaction	A^{a}	n	E^{a}
1	$H+O_2 \rightleftharpoons OH+O$	$3.52\ 10^{16}$	-0.7	71.42
2	$H_2+O \rightleftharpoons OH+H$	$5.06\ 10^{4}$	2.67	26.32
3	$H_2+OH \rightleftharpoons H_2O+H$	$1.17\ 10^{9}$	1.3	15.21
4	$H+O_2+M \rightarrow HO_2+M^{\mathrm{b}}$	$4.65\ 10^{12}$	0.44	0.0
5	$HO_2+H \rightarrow 2OH$	$7.08\ 10^{13}$	0.0	1.23
6	$HO_2+H \rightleftharpoons H_2+O_2$	$1.66\ 10^{13}$	0.0	3.44
7	$HO_2+OH \rightarrow H_2O+O_2$	$2.89\ 10^{13}$	0.0	-2.08
8	$H+OH+M \rightleftharpoons H_2O+M^{\mathrm{c}}$	$4.00\ 10^{22}$	-2.0	0.0
9	$2H+M \rightleftharpoons H_2+M^{\mathrm{c}}$	$1.30\ 10^{18}$	-1.0	0.0
10	$2HO_2 \rightarrow H_2O_2+O_2$	$3.02\ 10^{12}$	0.0	5.8
11	$HO_2+H_2 \rightarrow H_2O_2+H$	$1.62\ 10^{11}$	0.61	100.14
12	$H_2O_2+M \rightarrow 2OH+M^{\mathrm{d}}$	$2.62\ 10^{19}$	-1.39	214.74

Table 3.3: Forward rate coefficients in Arrhenius form $k = AT^n \exp(-E/RT)$ for the skeletal mechanism.

[a] Units are mol, s, cm^3, kJ, and K.
[b] Chaperon efficiencies are 2.5 for H_2, 16.0 for H_2O and 1.0 for all other species.
[c] Chaperon efficiencies are 2.5 for H_2, 12.0 for H_2O and 1.0 for all other species.
[d] Chaperon efficiencies are 2.0 for H_2, 6.0 for H_2O and 1.0 for all other species.

reaction rates in the real-gas framework, using chemical potentials directly computed from the equation of state has been investigated by [Giovangigli *et al.* 2011]. However, the impact on the flame structure appears to be rather small and tends to indicate that the perfect-gas treatment of the reaction rates is a good approximation. This is mainly due to high temperatures and relatively low pressures (and hence perfect-gas behavior) at the flame location. Note that since high pressure is considered in the present study,

the high-pressure limit of the falloff reactions have been taken.

The validation of the implementation in AVBP is achieved by comparing the flame structure using CANTERA [Goodwin 2002] and AVBP in a counterflow flame configuration. The numerical setup is that of an opposed-jet flame [Pons *et al.* 2009] computed, in AVBP, on a simple square mesh of size h with a constant grid size identical to that of the splitter case. The left boundary condition is a symmetry, the right side an outlet, while hydrogen comes from the top and oxygen from the bottom. The boundary velocity are determined to impose a constant strain, a, on the flame:

$$u_{O_2}(x) = ax \tag{3.8}$$

$$v_{O_2}(y) = -ay \tag{3.9}$$

$$u_{H_2}(x) = ax\left(\frac{\rho_{O_2}}{\rho_{H_2}}\right)^{\frac{1}{2}} \tag{3.10}$$

$$v_{H_2}(y) = -ay\left(\frac{\rho_{O_2}}{\rho_{H_2}}\right)^{\frac{1}{2}} \tag{3.11}$$

$$\tag{3.12}$$

The hydrogen velocity is chosen so that the momentum flux ρu^2 is the same between the oxygen and hydrogen stream, to place the stagnation point in the middle of the computational domain. As for the value of the strain rate, a, the validation is conducted at a value based on the splitter height h and the mean velocity difference between the two streams at the injection, which yields $a = 3800\ \mathrm{s}^{-1}$. A typical result of such strained diffusion flame is presented in Fig. 3.5 showing streamlines superimposed on the temperature field.

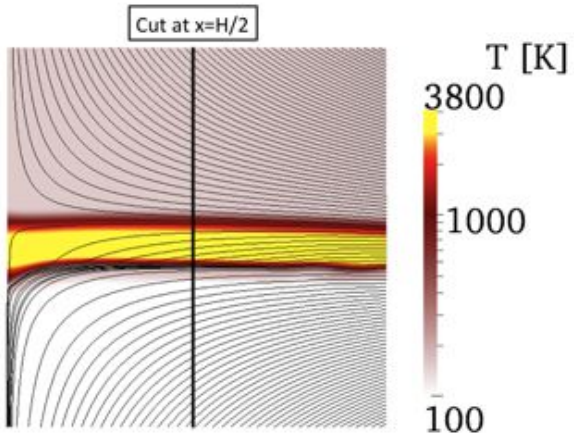

Figure 3.5: Strained diffusion flame computed in AVBP: streamlines superimposed on the temperature field. Thermodynamic conditions correspond to the splitter case: hydrogen at 150 K from the top, oxygen at 100 K from the bottom and ambient pressure is 10 MPa.

The validation procedure comprises three computations:

1. **CANT_PG**: a computation is performed using CANTERA using the perfect-gas equation of state. The temperature of the fresh gases is 300 K to limit real-gas effects.

2. **AVBP_PG**: this is the same computation as **CANT_PG**, performed in AVBP. Because CANTERA solves for the full transport matrices while AVBP assumes constant Schmidt numbers and mixture-averaged transport coefficients, this computation is both a validation of the implementation of the chemistry in AVBP as well as a validation of the simplified transport.

3. **AVBP_RG**: for this computation, the temperature of the fresh gases is lowered to match those of the splitter case and evaluate real-gas effects on the flame structure.

A cut through the flame at $x = h/2$ in the computational domain of AVBP is compared to the flame structure from CANTERA. Figure 3.6 shows the temperature and mass fraction of HO_2 (the main initiator of the combustion) versus the mixture fraction (see Eq. 1.3) for the three computations.

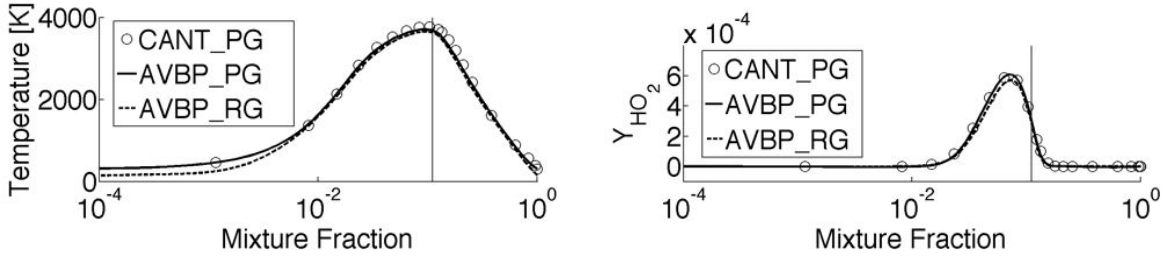

(a) (b)

Figure 3.6: Comparison of flame structure versus mixture fraction between AVBP and CANTERA. (a) temperature and (b) HO_2 mass fraction. The vertical bar indicates the stoichiometric mixture fraction.

First comparing simulations CANT_PG and AVBP_PG, the agreement between the two codes is excellent: the maximum discrepancy for the temperature is of the order of 70 K, which gives a relative error of 2 %. The differences for the mass fraction Y_{HO_2} are even smaller. This agreement validates the implementation in AVBP as well as the assumptions on the transport, for this temperature. The laminar flame in the thermodynamic conditions of the splitter case (AVBP_RG) is very similar to the higher-temperature computation (AVBP_PG) in the flame region. This conclusion is similar to that of [Ribert *et al.* 2008], justified by the fact that the combustion processes take place in hot regions where real-gas effects are negligible.

It is important to note, for later analysis of flame structures, that far from extinction, the structure of a non-premixed flame at a large Damköhler number is very close to the equilibrium lines, in the mixture fraction space. This is shown in Fig. 3.7, where the major species mass fractions are plotted against mixture fraction. It will thus be difficult to distinguish between a pure diffusion flame and a partially-premixed flame, solely looking

at the flame structure and local analysis in the physical space will have to be performed.

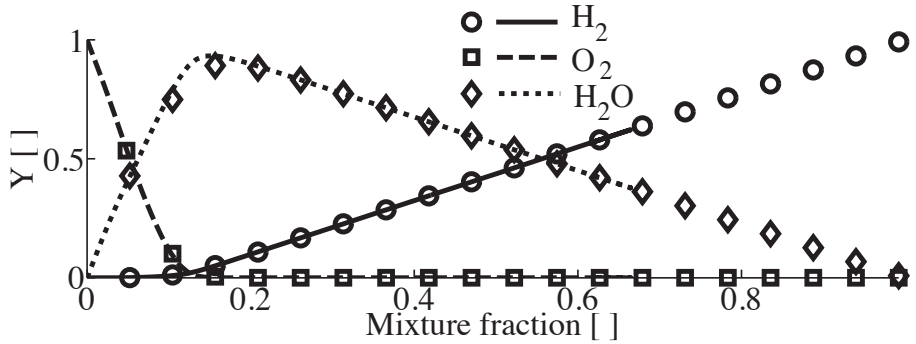

Figure 3.7: Major species mass fractions as a function of mixture fraction for the non-premixed counterflow flame configuration (lines) and equilibrium (symbols)

3.2 Cold Flow Results

In this section, the non-reacting flow is analyzed with specific attention to the interaction between turbulence and the large density gradients.

3.2.1 Vortex Shedding

Figure 3.8 shows an instantaneous axial velocity field. Small vortices are regularly shed from to the top corner of the lip, due to the shear-induced Kelvin-Helmholtz instability.

These vortices are either transported downstream, or trapped into the recirculation zone behind the lip. In both cases, many pairing events occur, as exemplified in Fig. 3.9, which ultimately forms large vortices having a length scale comparable to the splitter height. The dash lines follow the displacement of the small developing vortices, and allows to determine a visual convection speed of 5 m/s. This convection speed is smaller than the convection speed of the largest coherent vortices because, in the vicinity of the injector wall, the velocity magnitude is small (see Eq. 3.4). On the first four images of Fig. 3.9, the distance between vortices is approximately $h/8$. Using the convection speed of 5 m/s, the corresponding Strouhal number is equal to 1.0. Because of vortex merging, the distance between the vortices on the last four images of Fig. 3.9 is increased and equals $3h/8$, which corresponds to a Strouhal number of 0.3. Thus, subharmonics are created by vortex merging, which should be visible on the spectrum of the probe signals placed in the mixing layer. The vortex observed at the center of Fig. 3.8 results from this merging process.

Further downstream, the largest coherent vortices break down into smaller fluctuating motions, as observed at the right side of Fig. 3.8, while the flow transitions towards fully-developed turbulence.

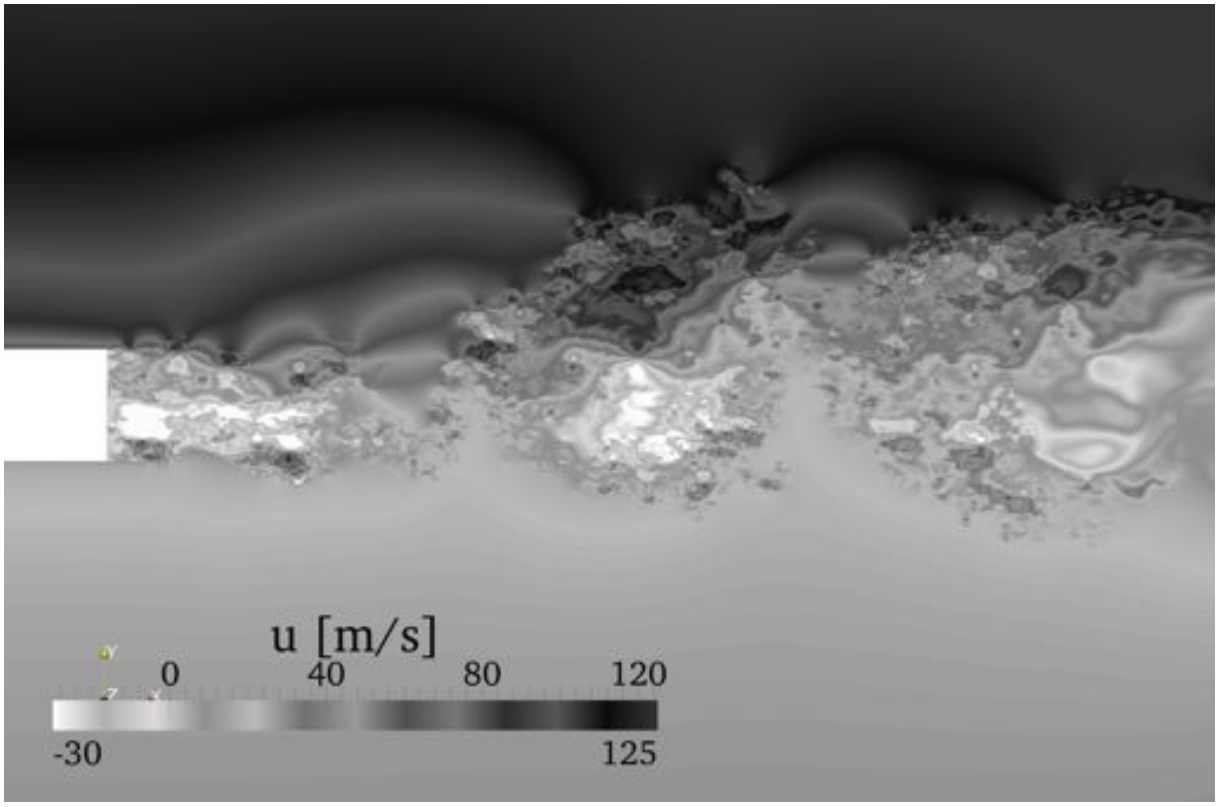

Figure 3.8: Non-reacting flow: axial velocity field, showing the shear-induced Kelvin-Helmholtz instability.

This large range of turbulent scales rapidly mixes the dense oxygen with the light hydrogen, as can be seen on the oxygen mass fraction field shown in Fig. 3.10.

Figs. 3.11 and 3.12 show a temporal evolution of the transverse velocity and the oxygen mass-fraction fields, respectively. The time interval between two snapshots is τ_{conv} and the dash lines follow the displacements of the largest coherent structures. These lines allow to determine a visual convection speed of the largest coherent structures $U_{conv,m}$ equal to 31 m/s. This value is slightly lower than the value of 39 m/s found using Eq. 3.5. However, using the phase velocity derived in [Juniper 2001]

$$U_p = \frac{U_{O_2}^{inj} + \frac{\rho_{H_2}}{\rho_{O_2}} U_{H_2}^{inj}}{1 + \frac{\rho_{H_2}}{\rho_{O_2}}}, \tag{3.13}$$

one finds exactly 31 m/s. In [Juniper 2001], it is conjectured that the convection speed of the coherent structures might start at U_p, given by Eq. 3.13 and tends towards U_{conv}, given by Eq. 3.5.

The wavelength of the largest coherent structures is approximately 5 h (distance between two dash lines). The time scale of the largest coherent structures is thus $\tau = 5h/U_{conv,m} \approx 6.5\ \tau_{conv}$, which correspond to a frequency of $f = 12$ kHz. The Strouhal

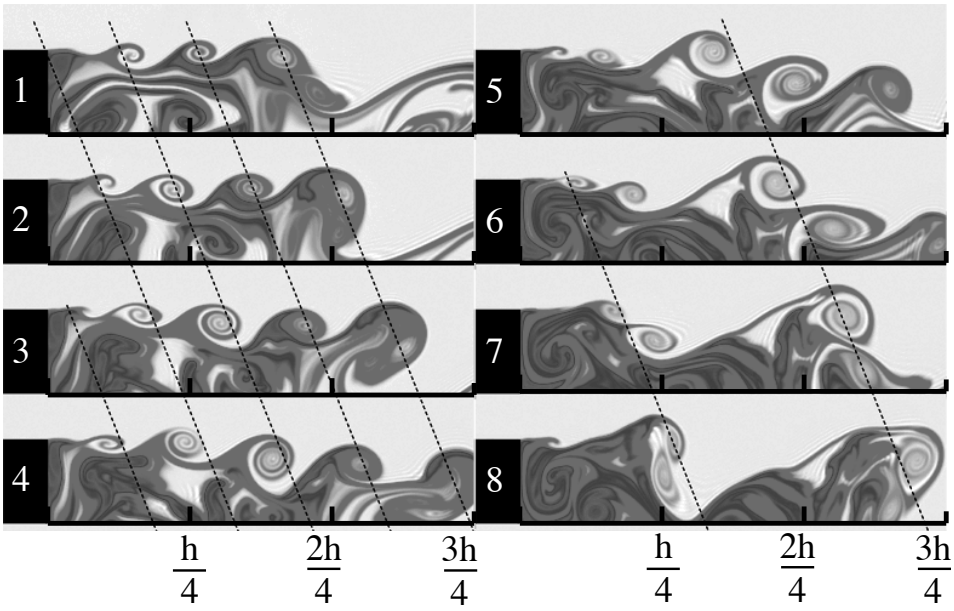

Figure 3.9: Non-reacting flow: oxygen mass fraction field at the H_2 corner of the lip, at successive instants. The time interval between frames is 10 μs

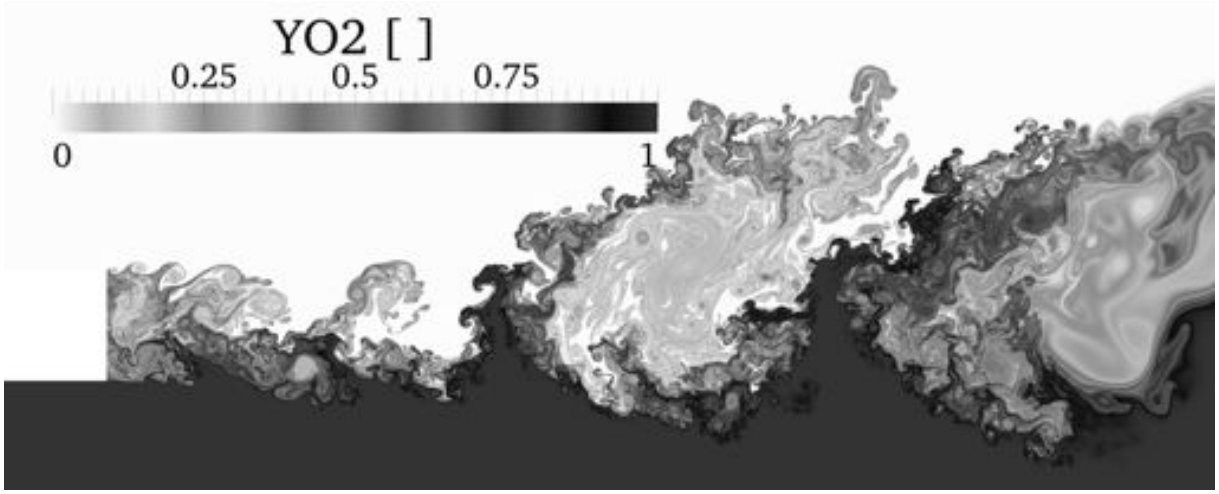

Figure 3.10: Non-reacting flow: O_2 mass fraction field, showing the rapid mixing of the two streams by a large range of vortical structures.

number, which is a non-dimensional frequency, is defined with the convective time:

$$St = f\tau_{conv} \tag{3.14}$$

The Strouhal number of the largest coherent structure, assessed visually, is thus $St = 0.15$.

Fourier transform

First, a single probe signal within the mixing region immediately before the outlet boundary condition (before the sponge layer, at i=10 and j=12 in Fig. 3.2) is plotted in the temporal and Fourier space, in Fig. 3.13. Although it is clear that a frequency dominates the signal ($St = 0.14$, the dash line plotted with the temporal signal), many secondary peaks are also observable. Note that the plotted power spectrum is actually a random variable and the average periodogram procedure [Oppenheim *et al.* 1989] must be used to reduce the variance of the spectrum estimate. Due to the small amount of time simulated, the Welch averaging procedure greatly deteriorates frequency resolution as shown in Fig. 3.14, for various numbers of windows. Since the total time simulated is 80 τ_{conv}, the strouhal number resolution is of the order of 10^{-2}, without spectrum averaging. Using 8 Welch windows approximately divides this resolution by 10, as shown in Fig. 3.14, but still enables the identification of a deterministic vortex shedding frequency: $St = 0.18$. This frequency is equal to the one determined visually, using Fig. 3.11.

The Fourier transform is then applied to the signals of the probes located at $j = 17$, between $i = 1$ and $i = 12$ on Fig. 3.2, which are located on the passage of the vortices shed from the H_2 corner of the lip. The axial evolution of the transverse velocity power density spectrum is plotted on Fig. 3.15. This figure shows that the vortex shedding strouhal number of the largest coherent structures (energy containing eddies) is $St \approx 0.2$, which is consistent with the previous visual observations and which is in the range of vortex shedding strouhal numbers observed in the range of 0.1 to 0.3 in multiple experimental studies at large Reynolds numbers (see [Roshko 1961] and [Williamson & Brown 1998], among others). In [Zong & Yang 2006, Zong & Yang 2007], a supercritical LOx/LCH_4 coaxial flow has been studied, and a frequency approximately equal to 0.2 was also found for vortex shedding, which is consistent with the present result. There are persisting strouhal number bands in Fig. 3.15 for $1 < St < 5$, which shows the existence of smaller coherent structures (subharmonics), as already observed in Fig. 3.9.

The power spectrum density of the squared transverse velocity ($E_{22} = u_2 u_2$, where E_{ij} is the Reynolds stress tensor) located at i=10, j=12 is shown in logarithmic scale in Fig. 3.16. For fully developed 2D turbulent flows, the spectrum inertial range exhibits a "-3 slope" [Rutgers 1998, Vallgren & Lindborg 2011]. A similar slope is observed in the present numerical simulation, which tends to indicate that the 2D turbulence is nearly developed at this location.

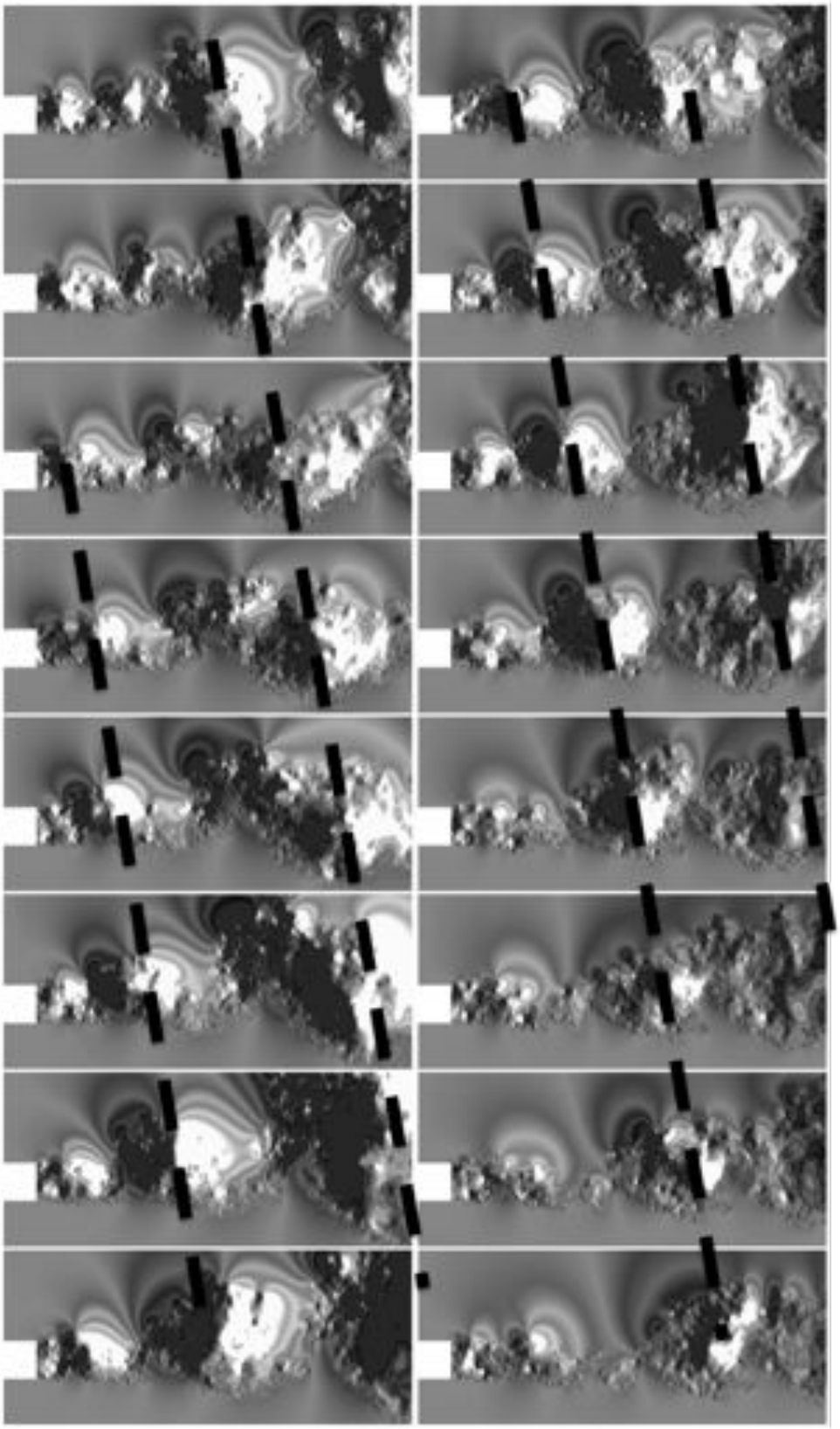

Figure 3.11: Non-reacting flow: temporal evolution of the transverse velocity field. The time interval between two snapshots is τ_{conv}

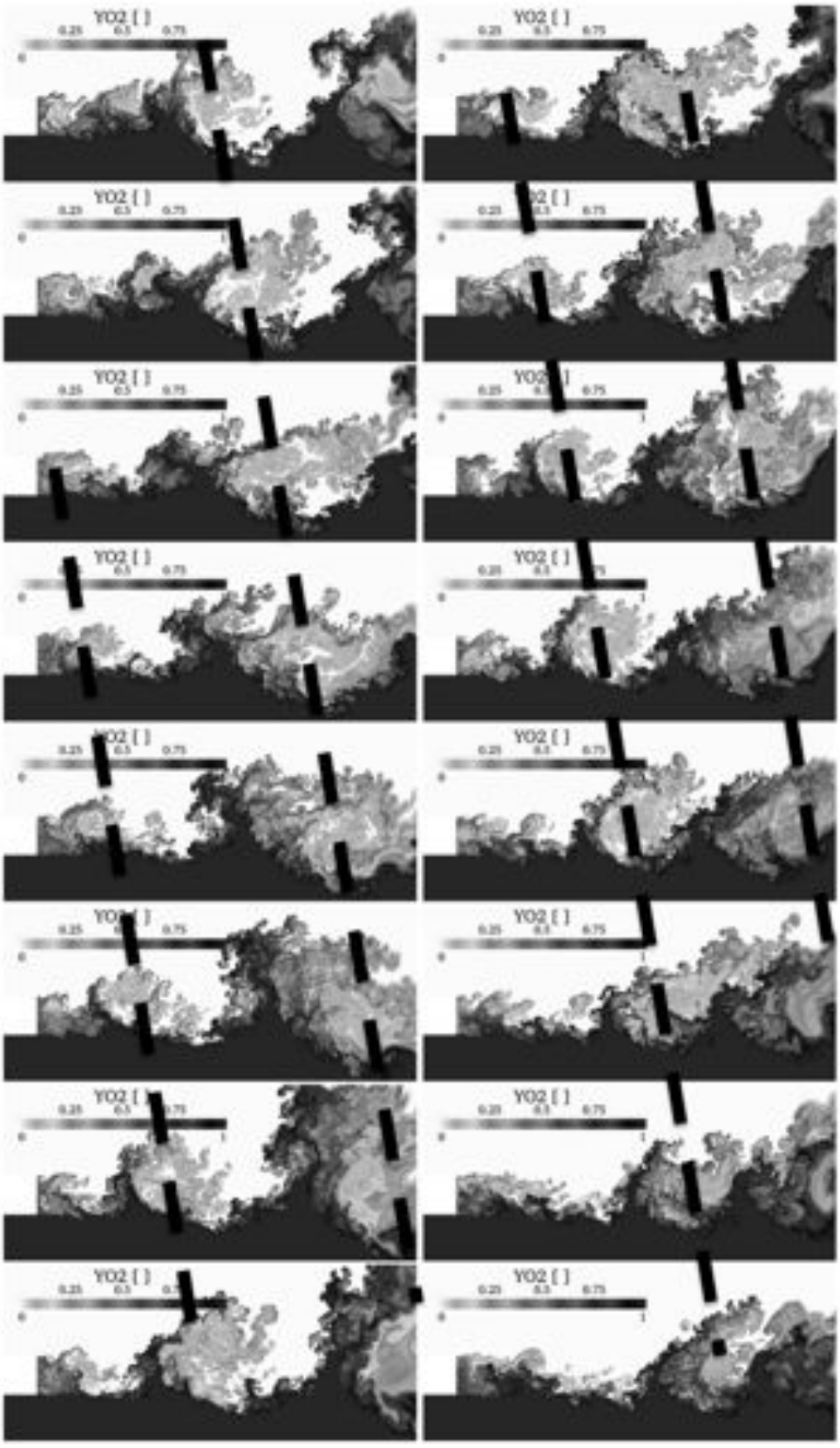

Figure 3.12: Non-reacting flow: temporal evolution of the oxygen mass-fraction field. The time interval between two snapshots is τ_{conv}

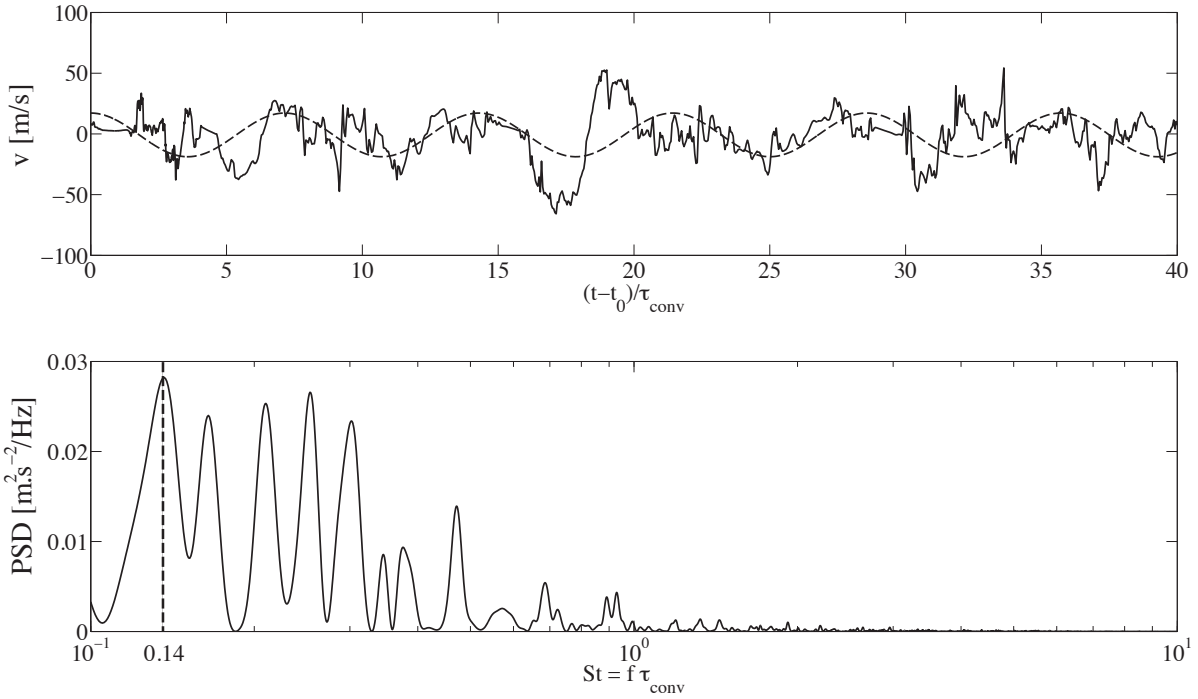

Figure 3.13: Non-reacting flow: transverse velocity signal analysis. Top) —— temporal signal; ---- dominant harmonic ($St = 0.14$). Bottom) Power Spectrum Density without spectrum averaging.

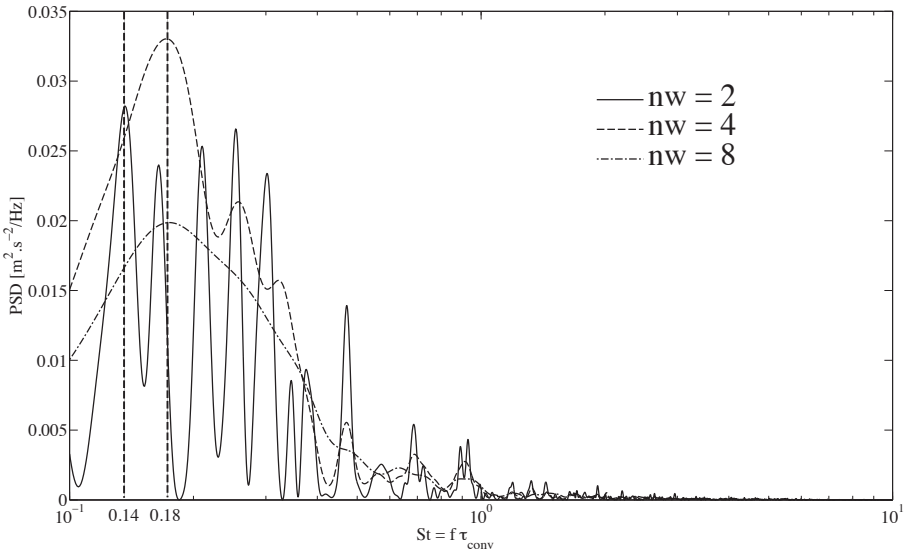

Figure 3.14: Non-reacting flow: effect of the Welch averaging procedure on the spectrum frequency resolution. Number of windows=2,4,8.

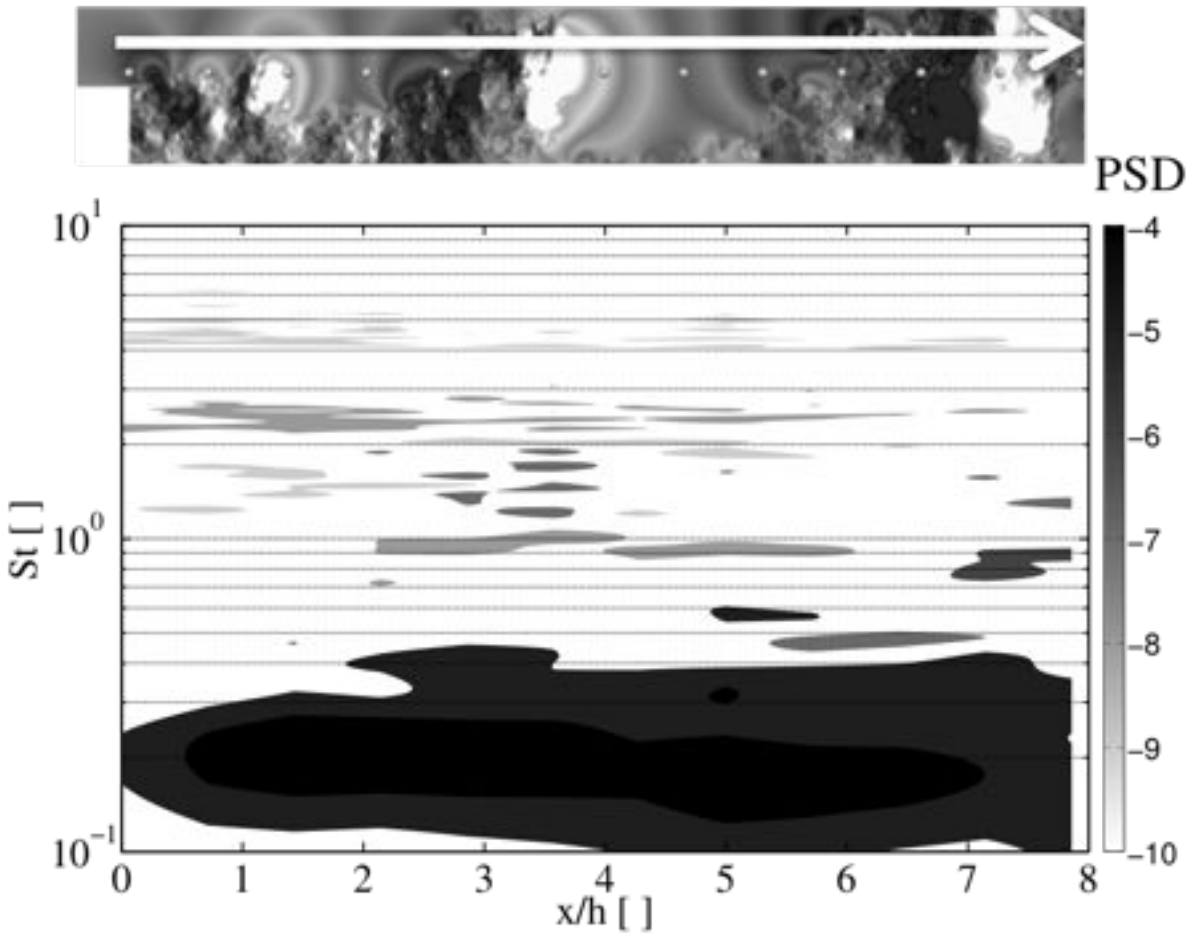

Figure 3.15: Non-reacting flow: spatial evolution of the transverse velocity spectrum in the wake of the lip. Eight Welch averaging windows are used.

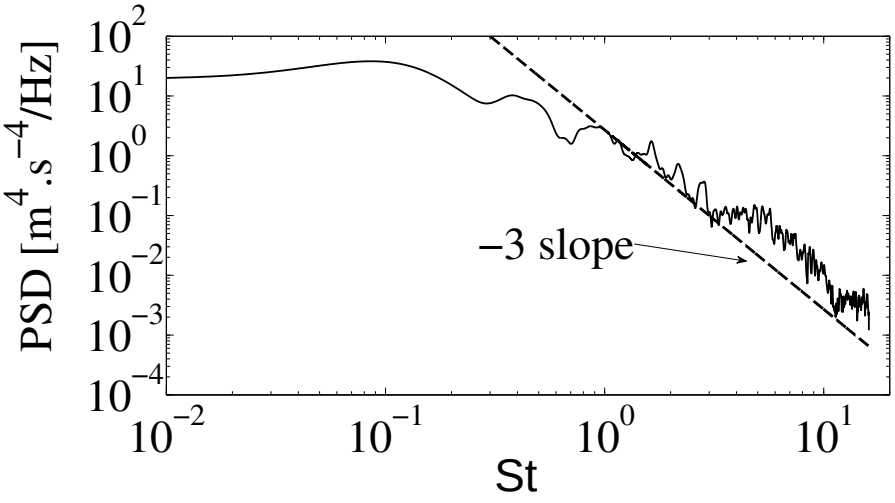

Figure 3.16: Non-reacting flow: power spectrum density of the squared transverse velocity at i=10, j=12. Eight Welch averaging windows are used.

3.2.2 Comb-like structures

Figure 3.17 shows the vorticity field superimposed on the high-density region (fluid regions with a density that is higher than $\rho_{0.5} = 0.5$ ($\rho_{H_2}^{inj} + \rho_{O_2}^{inj}$) are painted in black.). The emergence of low-speed oxygen fingers inside the high-speed hydrogen stream enhances shear-induced instability and creates small vortices. These small vortices increase the exchange surface between reactants, stretch the material interface and also feed large vortices through merging, which maintain the rise of the oxygen fingers. These finger-like structures are visually similar to experimental observations of transcritical mixing of coaxial jets (see Sec. 1.2.2, Fig. 1.6). In the absence of surface tension, the finger-like structures do not form droplets and are therefore further broken down by turbulence.

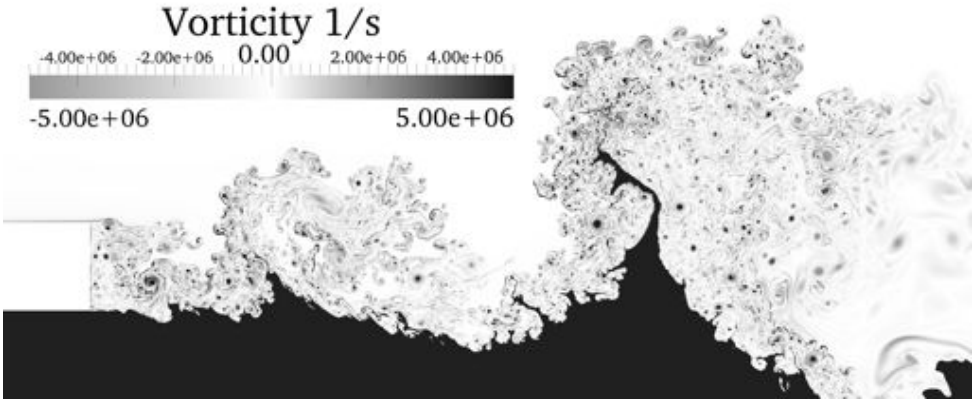

Figure 3.17: Non-reacting flow: vorticity field superimposed on the high-density region (fluid regions with a density that is higher than $\rho_{0.5} = 0.5$ ($\rho_{H_2}^{inj} + \rho_{O_2}^{inj}$) are painted in black.).

3.2.3 Scalar Dissipation Rate and turbulent mixing

The scalar dissipation rate χ, defined in Eq. 1.2, is a measure of the molecular mixing between hydrogen and oxygen. This mixing is favorable for combustion and is greatly enhanced by turbulence: the wrinkled exchange surface enables a larger total mass flux and strain locally steepens the composition gradients, which is also favorable for species diffusion.

Figure 3.18 shows a snapshot of the O_2 mass fraction, along with a grey isocontour of mid-density ($\rho = 637\ kg.m^{-3}$) and a white isocontour of high scalar dissipation rate ($\chi = 5\ 10^3\ s^{-1}$). This figure suggests that the majority of the scalar dissipation occurs on the light side of the fluid. The large molecular flux of oxygen leaving the dense LOx stream shifts the molecular mixing zone away from the transcritical density gradient. This figure is also a great example of the turbulence enhancement of mixing: the small vortices shed at the H_2 corner stretch the LOx/GH_2 material interface and merge to form larger vortices that roll-up the O_2 stream and traps pockets of H_2 in between two comb-like structures. At the right part of the figure, a dash circle shows a region where the scalar dissipation rate is low because mixing has already occurred.

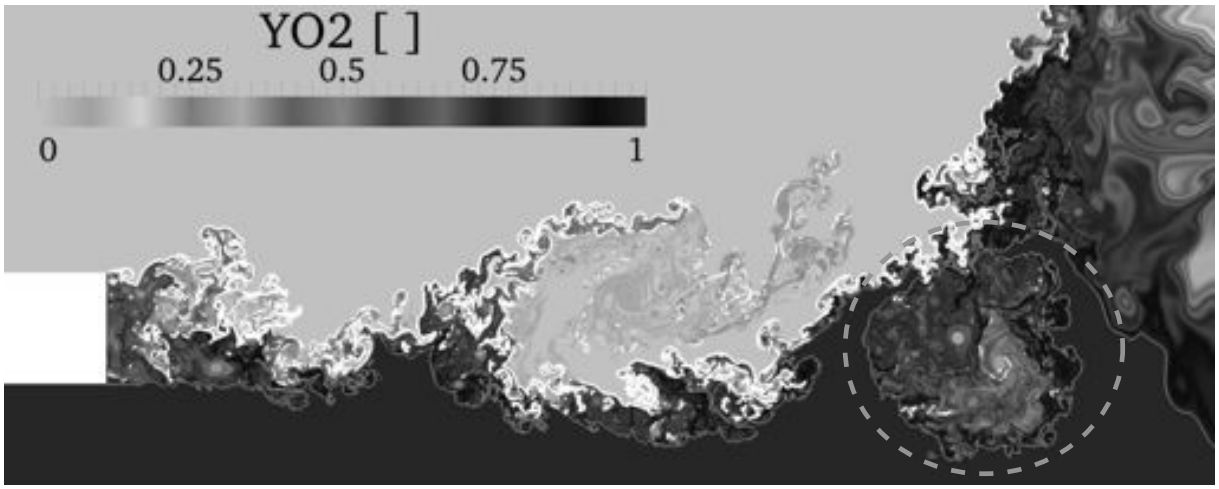

Figure 3.18: Non-reacting flow: O_2 mass fraction, along with a grey isocontour of mid-density ($\rho = 637$ kg.m^{-3}) and a white isocontour of high scalar dissipation rate ($\chi = 5\ 10^3$ s^{-1}). The dash circle shows a region of low scalar dissipation rate where mixing has already occurred.

To confirm that scalar dissipation rate is larger in the light part of the fluid, Fig. 3.19 shows the mean and maximum values of χ, conditioned on mixture fraction. It is notable that the maximum of scalar dissipation rate in the dense part of the fluid (below the stoichiometric mixture fraction $\mathcal{Z}_{st} = 1/9$) is several orders of magnitude lower than in the light part of the fluid ($\chi_{max} \approx 10^5\ s^{-1}$, at $\mathcal{Z} = 0.6$).

The scalar dissipation rate at the stoichiometric mixture fraction is of primary interest here, because it determines the order of magnitude of the flame thermal dissipation in the reacting case. At stoichiometry, the maximum scalar dissipation rate $\chi_{st,max} = 6\ 10^3$ s^{-1}

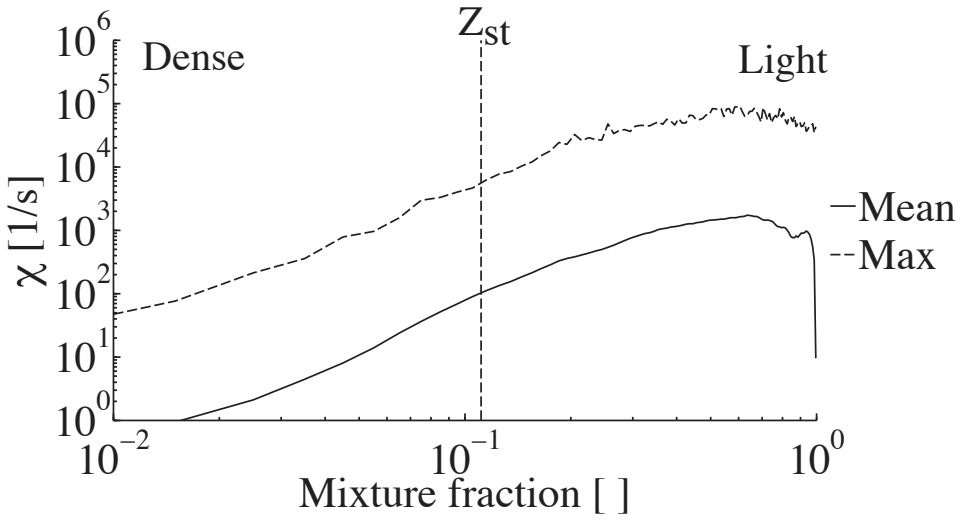

Figure 3.19: Non-reacting flow: conditioned average and maximum value of scalar dissipation rate as a function of mixture fraction.

is several orders of magnitude below the extinction scalar dissipation rate, which is approximately 3 10^6 s^{-1} [Kim *et al.* 2011]. The scalar dissipation rate at stoichiometry for the counterflow flame used for validation in Fig. 3.6 is 10^4 s^{-1} and is comparable to the maximum value encountered in this cold flow case.

3.2.4 Mean flow field

The observation of time-averaged solutions enables to quantify turbulent mixing.

Average solutions have been obtained sampling every 500 time steps ($\approx \tau_{conv}/50$), over a time period of approximately 8 T_{ft} (= 80 τ_{conv}) in the non-reacting case and 5 T_{ft} in the reacting case (see Sec. 3.1.4). In the non-reacting case, the statistical results stay qualitatively the same between 5 T_{ft} and 8 T_{ft} (not shown), thus only 5 T_{ft} are simulated in the reacting case.

Figure 3.20 shows the resulting average density field, using a logarithmic scale. On

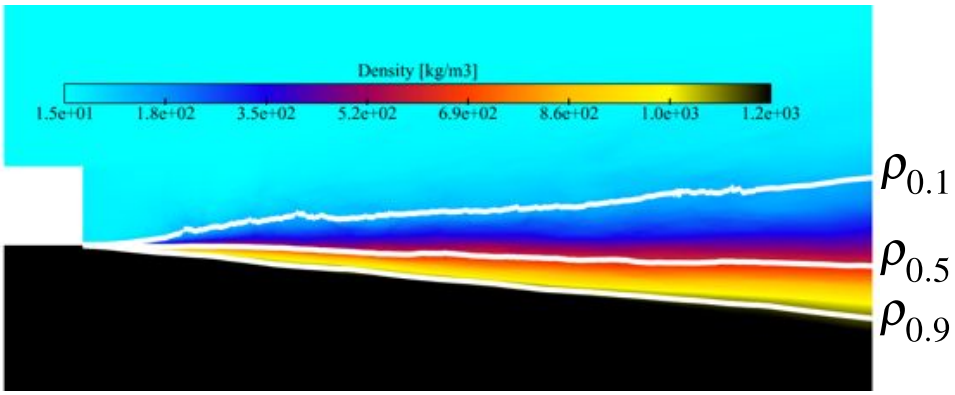

Figure 3.20: Non-reacting flow: average density field

Fig. 3.20, three iso-values of density are plotted at $\rho_{0.1}$, $\rho_{0.5}$ and $\rho_{0.9}$, where ρ_α is defined as

$$\rho_\alpha = \rho_{H_2}^{inj} + \alpha(\rho_{O_2}^{inj} - \rho_{H_2}^{inj}) \tag{3.15}$$

The location of the isoline at ρ_α may be determined as $y_{\rho,\alpha}(x)$, defined by:

$$\rho(x, y_{\rho,\alpha}(x)) = \rho_\alpha \tag{3.16}$$

The spreading angles of the LOx stream may then be calculated as:

$$\theta_{\rho,\alpha} = tan^{-1}(y_{\rho,\alpha}/x). \tag{3.17}$$

Fig. 3.21 shows the spreading angles for the 3 values of ρ_α of Fig. 3.20.

The spreading angles converge towards a constant value before the end of the computational domain, which tends to indicate a self-similarity state is reached. The $\rho_{0.1}$ isoline indicates the opening of the oxygen jet, and the spreading value of $+5°$ obtained in the numerical simulation is close to the value of 6 degrees found over a large range of density ratio in low pressure jets [Chen & Rodi 1980] and also well within the experimental scatter of transcritical injection experiments (see Fig. 14.b in [Schmitt *et al.* 2010b]). The $\rho_{0.9}$ isoline allows to determine a possible dense core length, although 2D turbulence is not the same as 3D turbulence, which is defined as:

$$L = R/tan(\theta_{\rho,0.9}). \tag{3.18}$$

With $R = 4.5\ h$ (radius of the oxygen injector) and $\theta_{\rho,0.9} = -5°$, $L \sim 10R$, which again is within the $10R$ to $20R$ range found in transcritical injection experiments (see Fig. 12b in [Oschwald *et al.* 2006]).

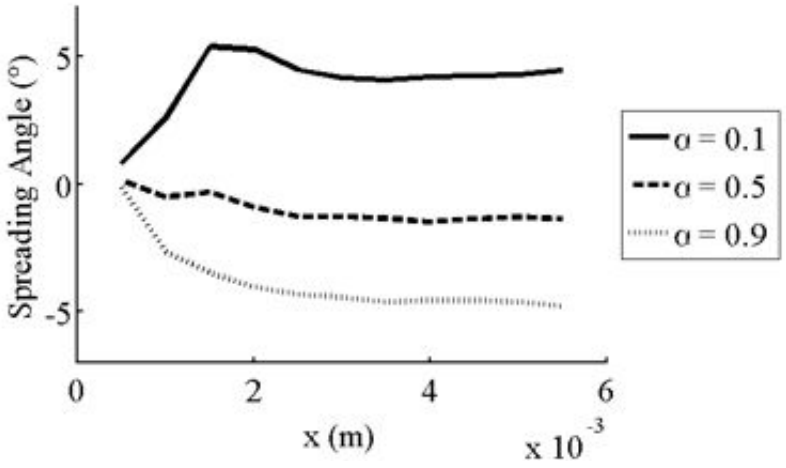

Figure 3.21: Non-reacting flow: spreading angles $\theta_{\rho,\alpha}$.

Transverse cuts through the average fields are plotted on Figs. 3.22, 3.23 and 3.24. Turbulent intensity reaches high values of about 30%, which is well above a typical 10% turbulent intensity in jet developed turbulence, because of the large coherent structures developing in the mixing layer. From the RMS plots of the axial and transverse velocity, one can see that the lower and upper boundary conditions are actually confining the jets, since u_{RMS} do not reach zero and since the v_{RMS} profile is obviously influenced by the upper boundary condition. This confinement influences the jet dynamics but is representative of a coaxial injector with a recessed LOx tube, as explained in Sec. 3.1. The RMS velocities are normalized by the velocity difference between the two streams:

$$U_s = U_{H_2}^{inj} - U_{O_2}^{inj}. \tag{3.19}$$

This correspond to the maximum fluctuation velocity for turbulent motions in a non-reacting flow. In terms of intensity, both components of the velocity reach similar values (~ 30 %) that are already attained at $x = h$. This highlights again the intense turbulent activity behind the splitter. As vortical structures are transported and grow downstream the splitter plate, fluctuations spread, with deeper penetration into the light hydrogen stream, which is consistent with the temporal mixing layer study of [Okong'o & Bellan 2002b].

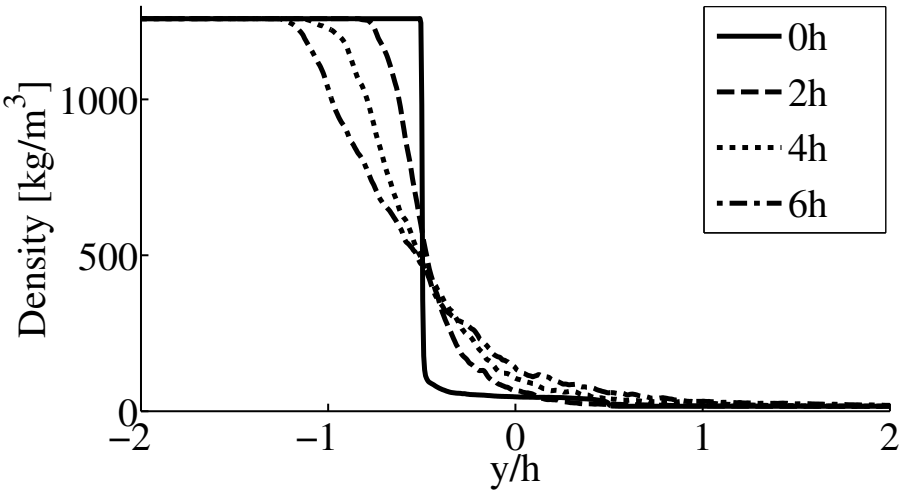

Figure 3.22: Non-reacting flow: transverse cuts of the density at 4 axial positions between x=0h and x=6h.

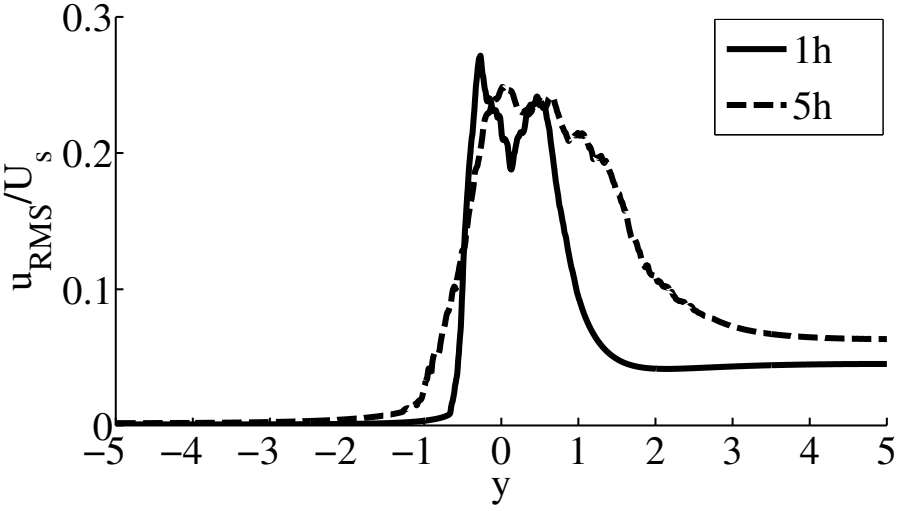

Figure 3.23: Non-reacting flow: transverse cuts of the RMS axial velocity normalized by the velocity difference $U_s = U^{inj}_{H_2} - U^{inj}_{O_2}$ at x=1h and x=5h.

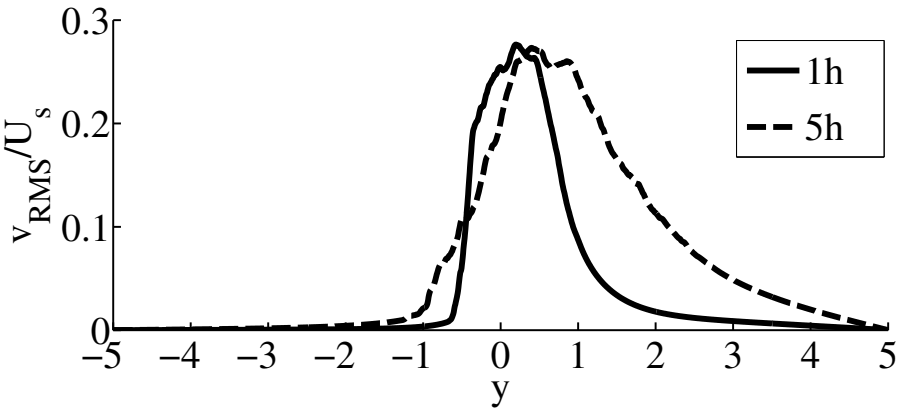

Figure 3.24: Non-reacting flow: transverse cuts of the RMS transverse velocity normalized by the velocity difference $U_s = U_{H_2}^{inj} - U_{O_2}^{inj}$ at x=1h and x=5h.

3.2.5 Influence of mesh resolution

In order to verify mesh convergence, a simulation with a coarser mesh has been conducted. With this coarse mesh, the splitter height h contains 100 grid points (instead of 500). In the following, the coarse and refined mesh are called 'h100 and 'h500', respectively.

Instantaneous visualization

Figure 3.25 shows instantaneous snapshots of the transverse velocity for the h100 and h500 meshes. Even though the smallest scales are missing from the h100 mesh, the flow fields are qualitatively similar, with small vortices shed at the H_2 corner of the lip, which merge further downstream and roll-up the oxygen stream.

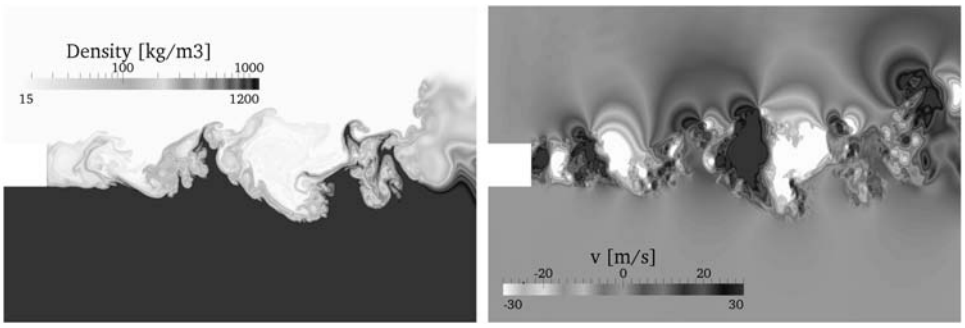

(a)

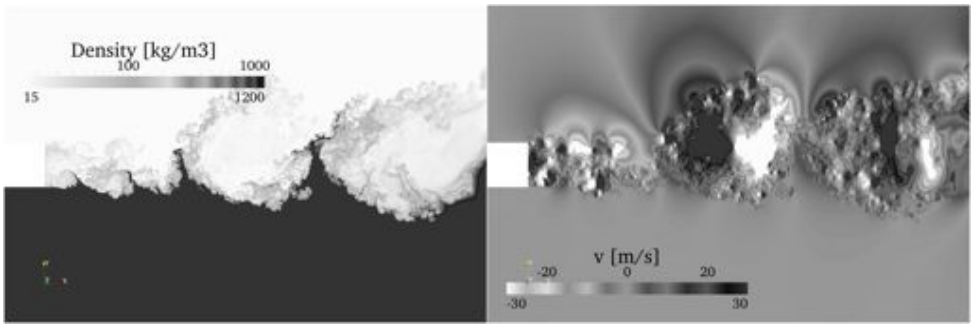

(b)

Figure 3.25: Instantaneous snapshots of the transverse velocity and the density for the (a) h100 and (b) h500 meshes.

Time-average solutions

Figure 3.26 and Fig. 3.27(a) show the mean and RMS profiles for the h100 and h500 meshes at $x = 5$h, which is located in between the injection and the outlet plane. The agreement between the h100 and h500 meshes for both the RMS and mean profiles is very good, which proves that mesh convergence is attained for the results presented in Sec. 3.2, in spite of the numerical stabilization of the transcritical density gradient.

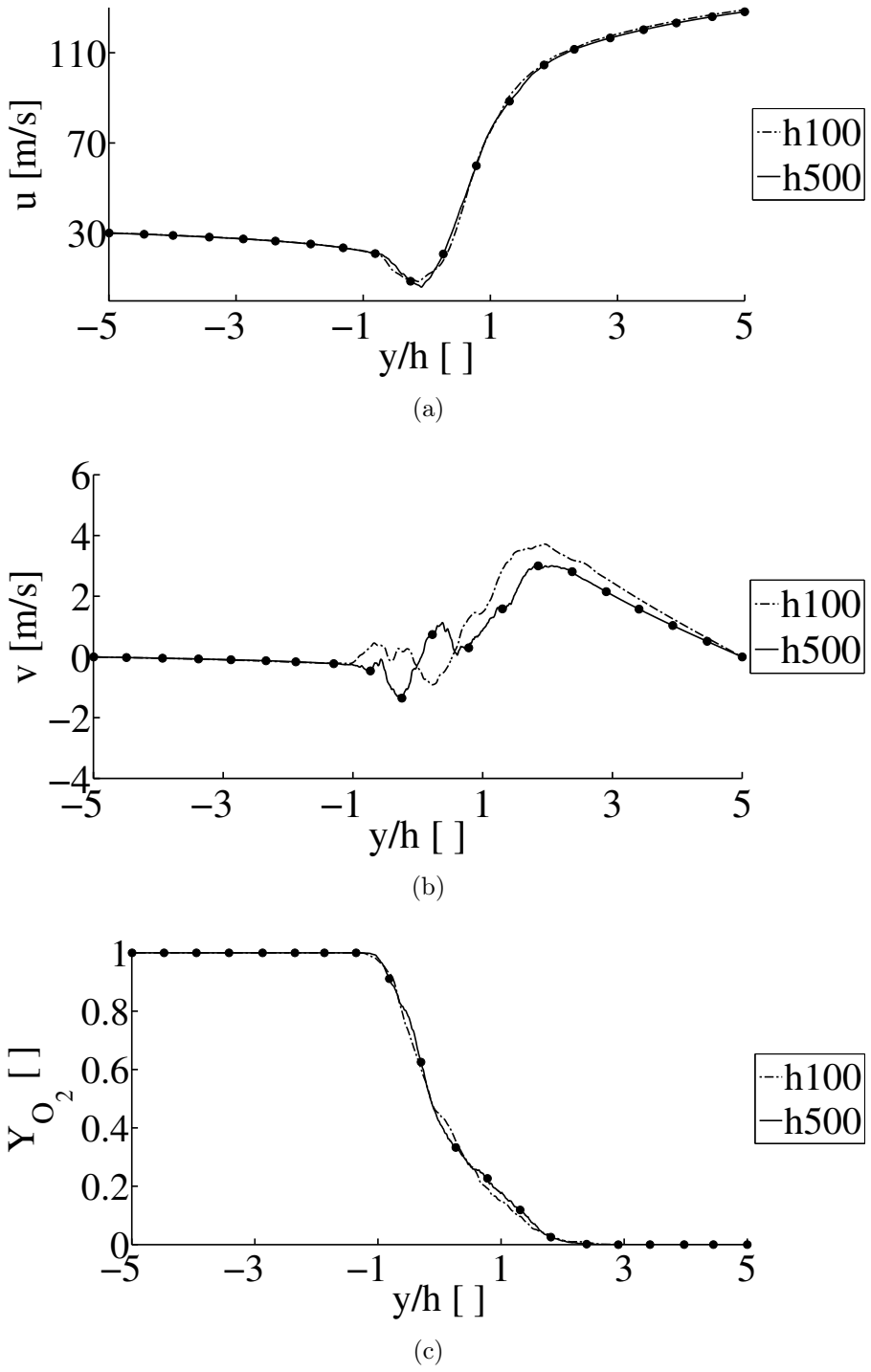

Figure 3.26: Mean profiles, at $x = 5$h for the h100 and h500 meshes of (a) axial velocity, (b) transverse velocity and (c) O_2 mass fraction

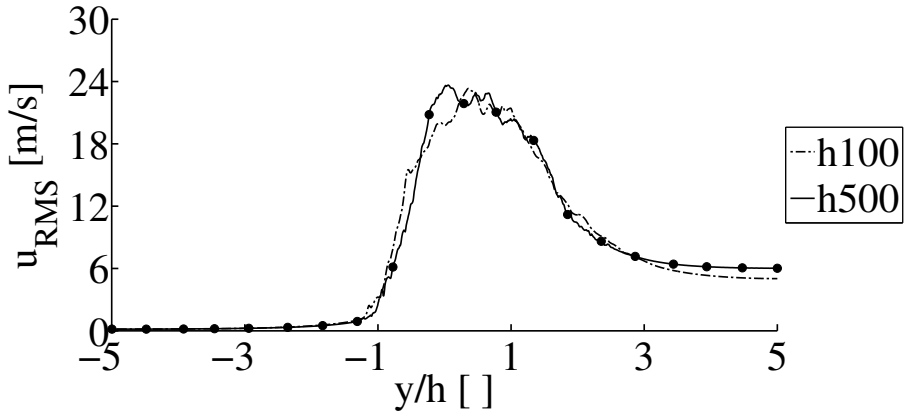

(a)

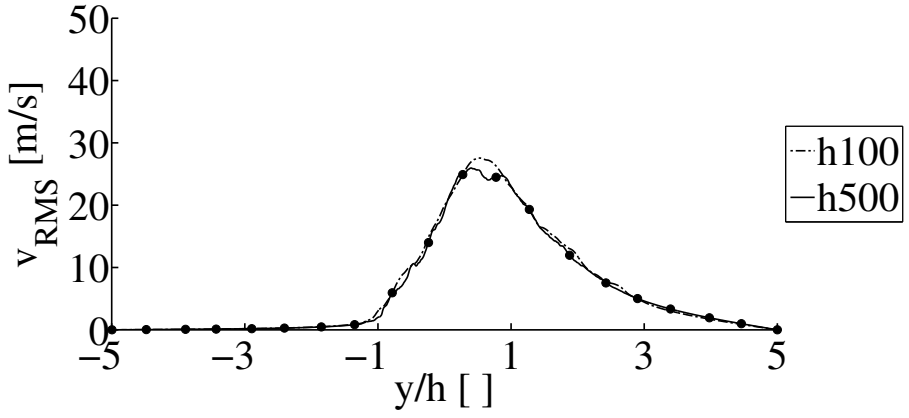

(b)

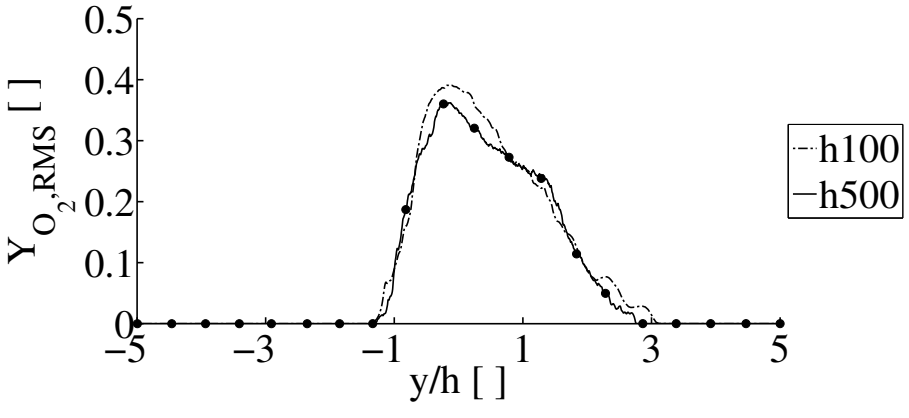

(c)

Figure 3.27: RMS profiles, at $x = 5$h for the h100 and h500 meshes, of (a) axial velocity, (b) transverse velocity and (c) O_2 mass fraction.

3.3 Reacting Flow

In this section, the reacting flow field is studied. The cold flow solution is instantly replaced by a hot flow field following the procedure detailed in Sec. 3.1.6. While keeping the main characteristics of the non-reacting flow in mind, the following questions are addressed:

- Where is the flame stabilized and how ?
- Although the reactants are non-premixed, is the turbulent flame a pure diffusion flame ? How can this flame structure be modeled in a LES computation ?
- Are the comb-like structures still forming in the reacting flow and if so, how do they interact with the flame ?

3.3.1 Flame stabilization

An instantaneous temperature field is presented in Fig. 3.28 with superimposed iso-contours of density gradient (green=4 10^7 kg/m^4) and heat release rate (grey=10^{12} W/m^3, black=10^{13} W/m^3). The flame is not lifted and the hot gases touch the splitter plate. This is partially due to the adiabatic boundary condition imposed at the solid boundary. However, H_2/O_2 flames are known to be extremely reactive and experimental evidence under comparable thermodynamic conditions showed that the flame is stabilized very close to the splitter [Singla *et al.* 2007].

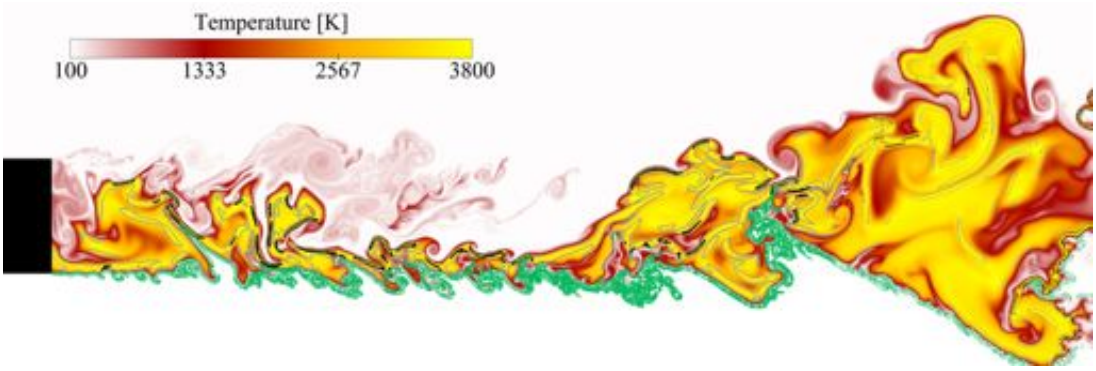

Figure 3.28: Temperature field with superimposed density gradient (green) and heat-release (black: max heat release rate of case AVBP_RG (=10^{13} W/m^3); grey: 10 % of case AVBP_RG (=10^{12} W/m^3).

The temperature field is much wrinkled on both oxygen and hydrogen sides. Pockets of oxygen are sometimes captured in the hot gases, especially in the second half of the computational domain. This observation allows to speculate that these pockets of warmed-up oxidizer could eventually enter the hydrogen stream and generate a corresponding unsteady heat release. The combustion modes will be studied in more details in Sec. 3.3.3.

The green iso-contour highlights the region of high density gradient and allows to distinguish the dense stream from the lighter regions.

A close-up view of the vicinity of the splitter is presented in Fig. 3.29. Regions of strong reaction rate are visible at the edges of the high-temperature pockets, both on the hydrogen and oxygen sides, which shows the importance of turbulent transport across the splitter height.

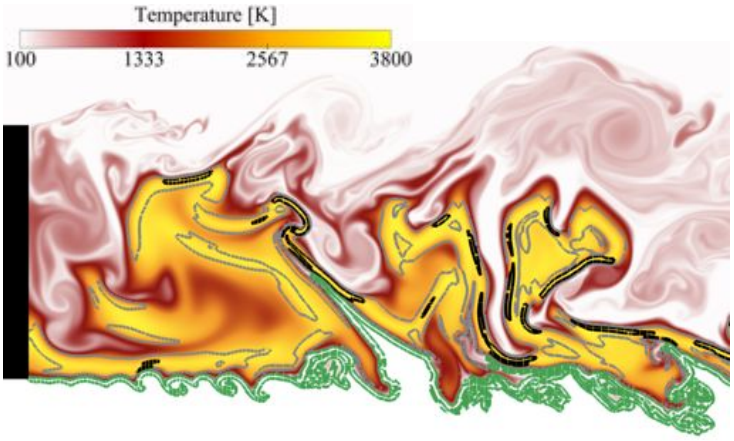

Figure 3.29: Close-up view of the flame stabilization zone behind the splitter. Temperature field with superimposed iso-contours of density gradient (green=4 10^7 kg/m^4) and heat-release rate (grey=10^{12} W/m^3, black=10^{13} W/m^3).

A schematic view of the flame splits it into two parts, as shown in Fig. 3.30:

- a near-injector steady diffusion flame between O_2 and a mixture of combustion products and fresh hydrogen (mainly H_2 + H_2O), at the LOx corner. The flame is quasi-laminar because it is not disturbed by the vortices shed at the H_2 corner.
- a turbulent diffusion flame developing further downstream.

3.3.2 Vortex shedding and comb-like structures

Figure 3.31 shows the density field for both the non-reacting and the reacting flow. The first striking feature is the difference between the LOx stream shapes: the LOx stream moves straight forward in the hot flow case whereas it is rolled up by the large vortices shed at the H_2 corner of the lip in the cold flow case. These complex flame/vortex interactions drive turbulent mixing. Such reduction in the vertical extent of the mixing layer under reacting conditions has already been observed at low pressure [Renard *et al.* 2000].

Curvature of the density field

In order to quantify the visual differences observed in the reacting and non-reacting cases, the probability density function (PDF) of the curvature of a density iso-surface is presented in Fig. 3.32. The value chosen for the curvature analysis is the iso-surface at

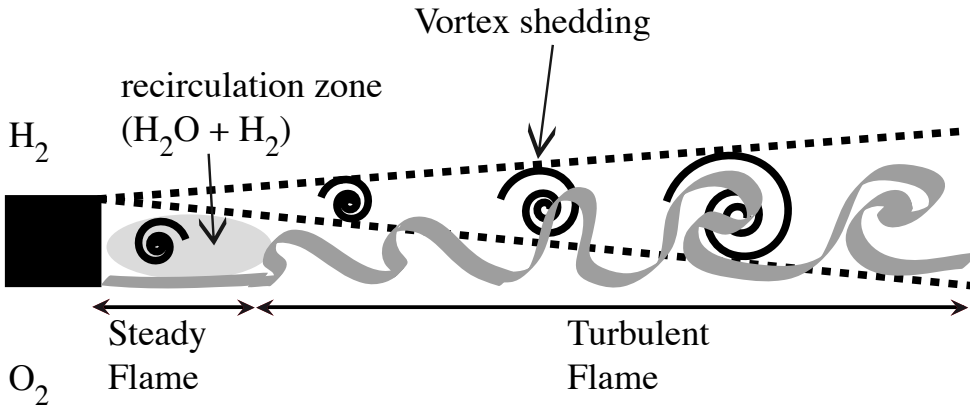

Figure 3.30: The flame/vortex interaction separates the flame into 2 zones, a near-injector steady diffusion flame between O_2 and a mixture of H_2 and H_2O, and a turbulent flame developing further downstream.

the intermediate density between the hydrogen and oxygen streams $\rho_{0.5}$ (~ 600 kg.m^{-3}), defined in Eq. 3.15. While the PDF for the reacting flow is roughly symmetric and centered around a zero value, the curvature PDF for the cold flow is double peaked: the peak at -10^4 m^{-1} corresponds to a concave radius of curvature of $h/5$ in the density isocontour. This indicates that although visually, the large density waves appears to have a characteristic radius of curvature of h, they actually consist in a collection of highly curved pieces. The difference between the hot and cold flow curvature PDF also confirms the visual observation that the density waves disappear in the hot flow. Note that the PDFs plotted in Fig. 3.32 are actually shown in the [-1 10^5, 1 10^5] subrange, which allows to clearly observe the double-peaked PDF in the cold case. The integrals of the PDFs between $-\infty$ and $+\infty$ are both equal to one.

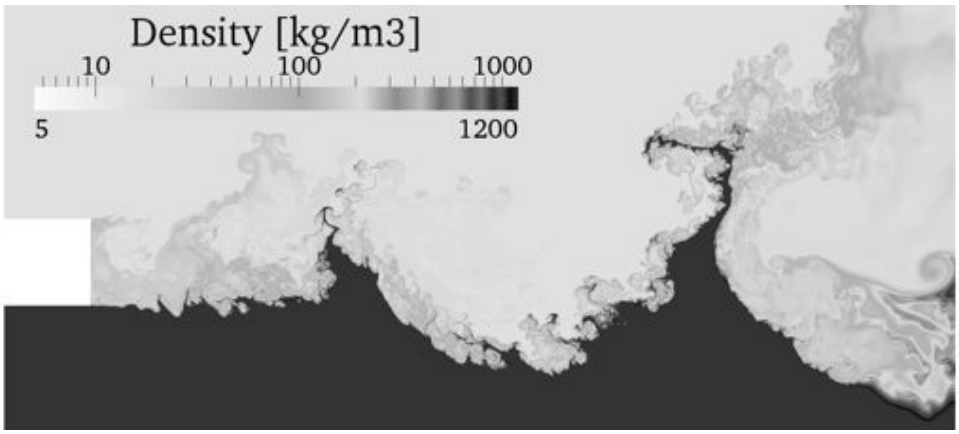

(a)

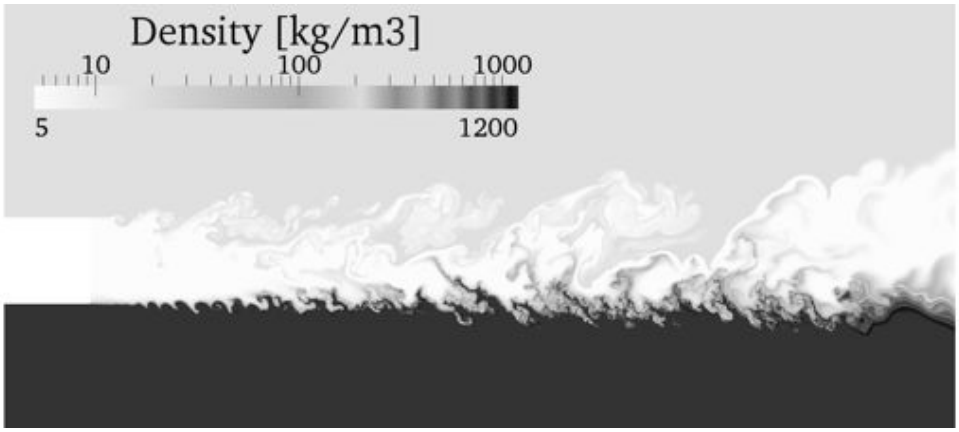

(b)

Figure 3.31: Comparison of the density fields between a) the non-reacting flow and b) the reacting flow

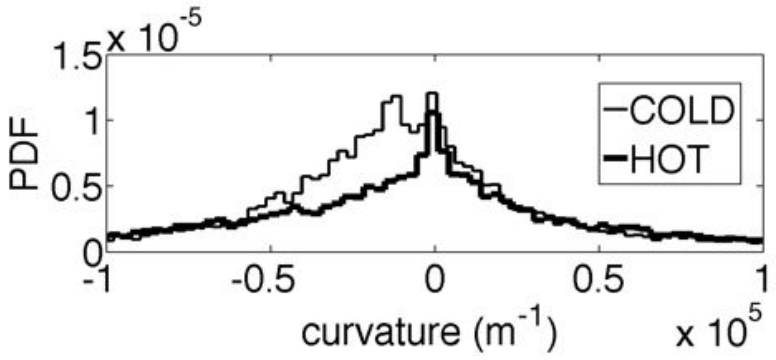

Figure 3.32: Curvature PDF of the median density ($\rho_{0.5}$ iso-contour for the cold and reacting flows.

3.3.3 Combustion Modes

Direct visualization

Figure 3.33 shows the fields of oxygen, hydrogen and water (major species), with superimposed stoichiometric mixture fraction isoline. The flame is predominantly composed of non-premixed flame elements located on the stoichiometric mixture fraction line, to which pure hydrogen flows against pure oxygen.

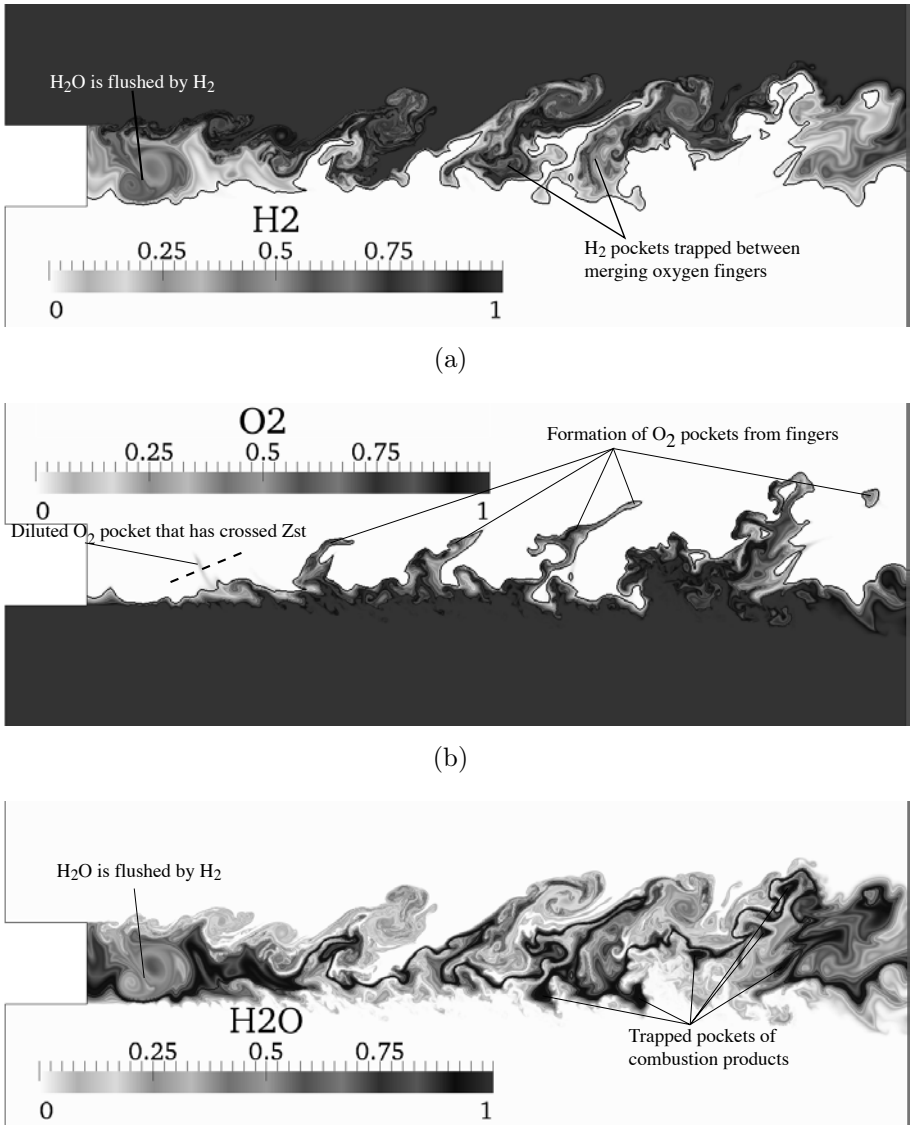

Figure 3.33: Reacting flow: instantaneous fields of (a) hydrogen (b) oxygen and (c) water mass fraction, with superimposed stoichiometric mixture fraction isoline (black). The dash line in (b) shows the location of the 1D cut that is used in Fig. 3.34.

In a similar manner as in the non-reacting flow, the passage of the vortices shed at the lip, rolls the oxygen stream and initiates the formation of oxygen fingers, as shown

in Fig. 3.33(b). The exchange surface between oxygen and hydrogen is thus increased, which enhances the consumption rate of reactants. The fingers of oxygen are sometimes sliced into isolated pockets, due to the joint action of turbulence and chemical reactions. A pocket of oxygen appears above the stoichiometric line on the left of Fig. 3.33(b) (dash line), because of dilution with the surrounding combustion products, as shown in Fig. 3.34.

Pockets of hydrogen and pockets of combustion products can also be trapped into the oxygen stream as shown in Fig. 3.33, for instance when two fingers of oxygen merge.

Immediately behind the lip, the fluid is composed of a large amount of recirculated combustion products and a small amount of fresh hydrogen that is continuously supplied by coherent structures. Intermittently, a large coherent structure can flush this pocket of combustion products which is replaced by fresh hydrogen, as shown in Fig. 3.33(a). Thus, the reservoir of fuel of the steady diffusion flame that is attached to the splitter plate, has a varying composition which induce an oscillatory flame structure.

As already observed in the non-reacting case, turbulence develops with the downstream distance of the lip which makes flame/turbulence more important. Before the end of the computational domain, this creates mixed combustion modes where pockets of hydrogen (or oxygen) trapped into the oxygen stream (or the hydrogen stream) can burn against a non-premixed flame element, which creates complex flame structures.

Flame structure in mixture fraction space

The reacting flow is now observed in the mixture fraction space, in Fig. 3.35, where the counterflow flame computed in Sec. 3.1.7 is also shown as a reference (dashed red line).

Consistently with the direct visualization of the flame, no extinction occurs and the great majority of points are located along the diffusion flame manifold. The adiabatic flame temperature for a stoichiometric mixture is approximately 3800 K and this value is reached at the stoichiometric mixture fraction.

From visual observations of the unsteady flame (not shown), it has been found that the points located above equilibrium are associated with highly curved pockets of reactants. The preferential diffusion effects, which are enhanced by curvature, can induce super-equilibrium states as shown for instance in [Gicquel *et al.* 2005]. Since far from extinction, the variation with strain rate of the maximum temperature in a high pressure H_2/O_2 counterflow diffusion flame is small ($\Delta T_{max} < 100\ K$ at 10 MPa, over 7 orders of magnitude of the strain rate [Ribert *et al.* 2008]), the points below the reference temperature are induced by dilution.

It is therefore concluded that even though chemistry plays a key role in the stabilization of such flame, turbulent transport is also active and influences the combustion modes. It is also foreseen that for fuels with less chemical activity, turbulence could become a key stabilization process.

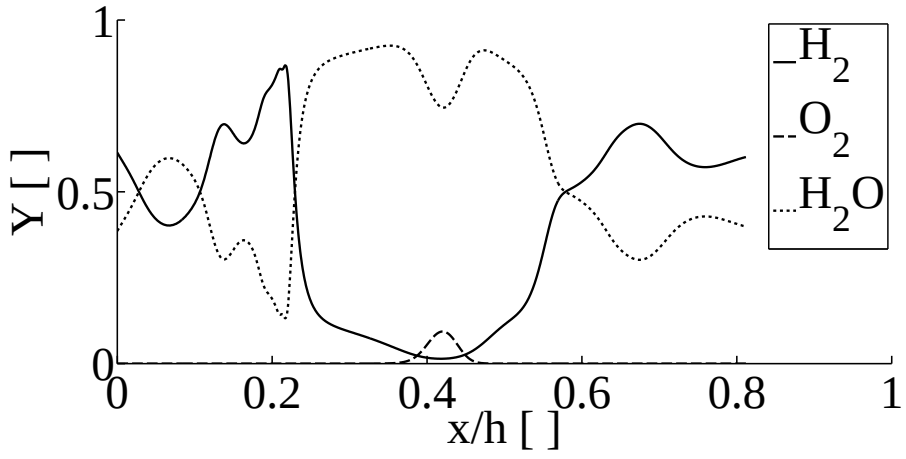

(a)

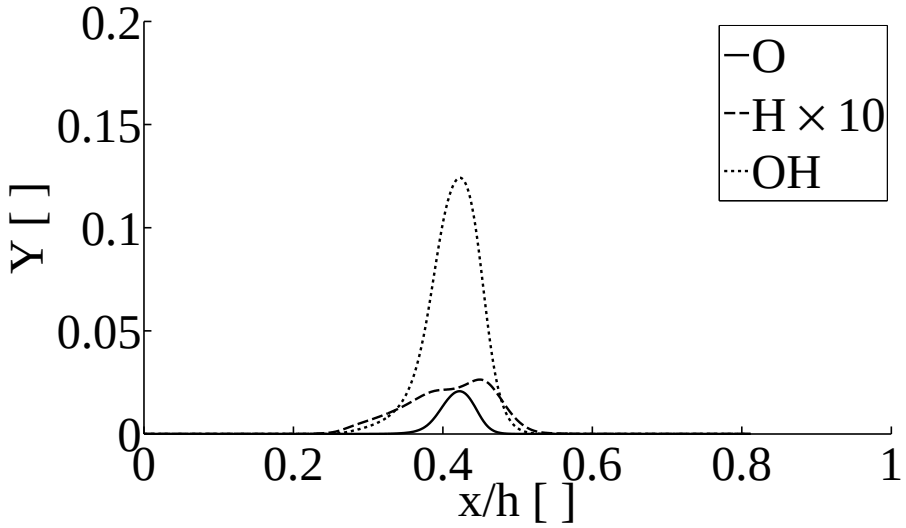

(b)

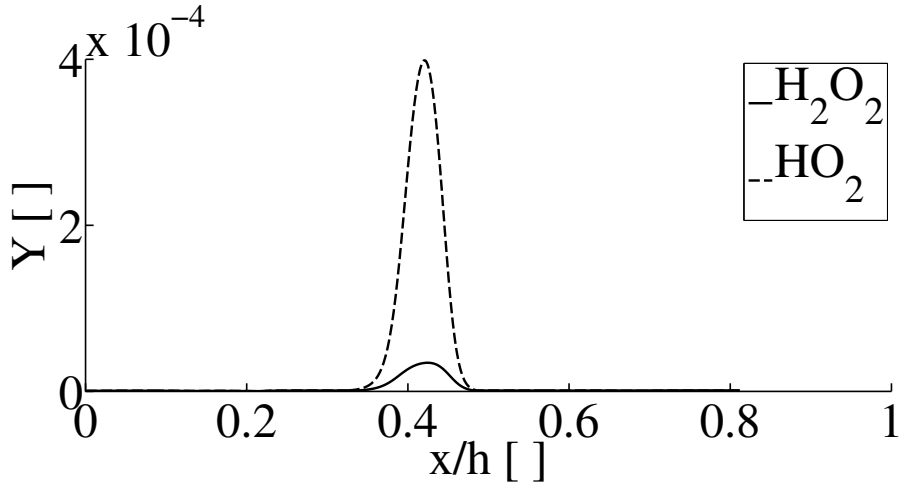

(c)

Figure 3.34: Cut through a pocket of oxygen diluted with combustion products. The location of the 1D cut is shown by a dash line in Fig. 3.33(b).

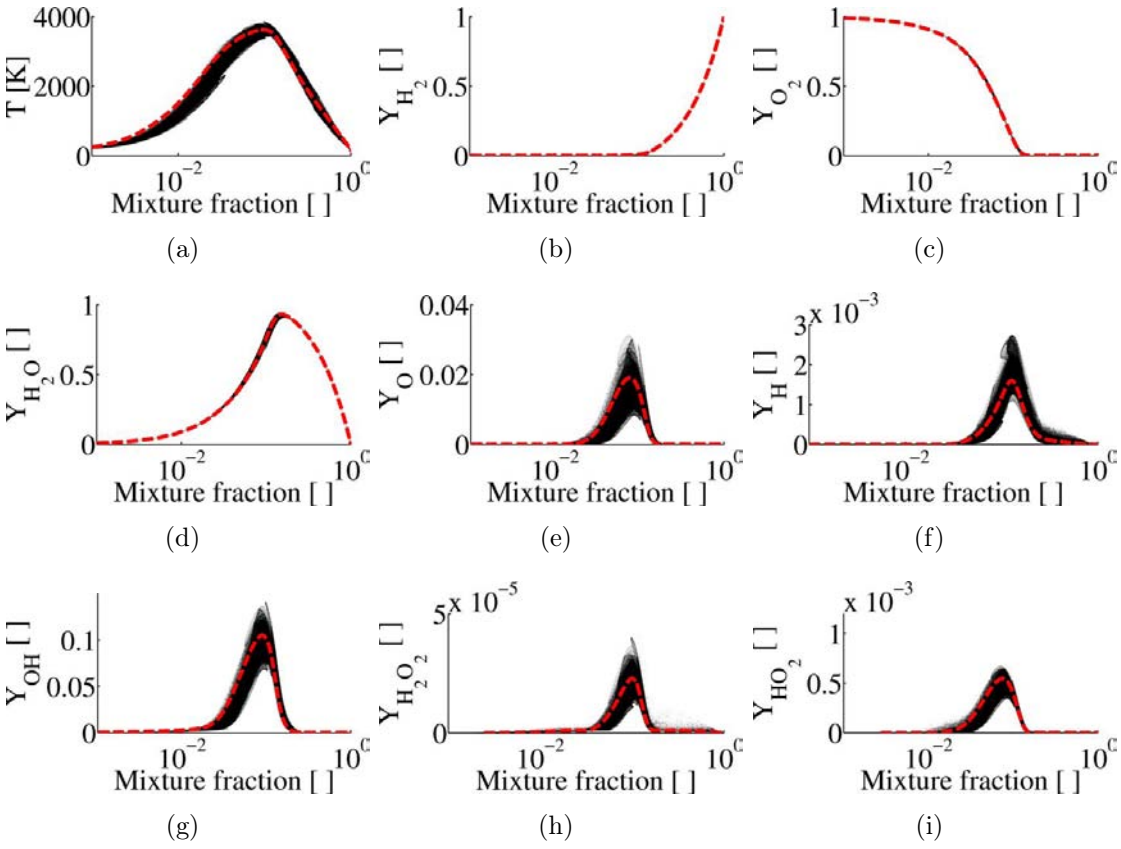

Figure 3.35: Flame structure in the mixture fraction space. ---- counterflow diffusion flame at $a = 3800$ s^{-1}, • scatter plot of the present turbulent flame.

3.3.4 Mean flow field

The reacting flow field was averaged over a period of 5 T_{ft} ($\approx$ 0.6 ms), which is large enough to observe the main characteristics of the mean field even though the statistics may not be fully converged. Figure 3.36 shows the resulting average density field, using the same logarithmic scale and iso-contour as for Fig. 3.20. The outlet region corresponding to the sponge-layer described in Sec. 3.1 is grayed out because the flame characteristics are not physical in this region. For the present reacting flow, the angle of the dense core is $\theta_{\rho_{09}} = -2°$, which corresponds to a dense core length $L \sim 30\ R$. This value, based on a relatively short computational domain, is three times larger than the cold flow. This is attributed to the heat release rate, which prevents the formation of the large vortices observed in the cold flow (c.f. Fig. 3.28).

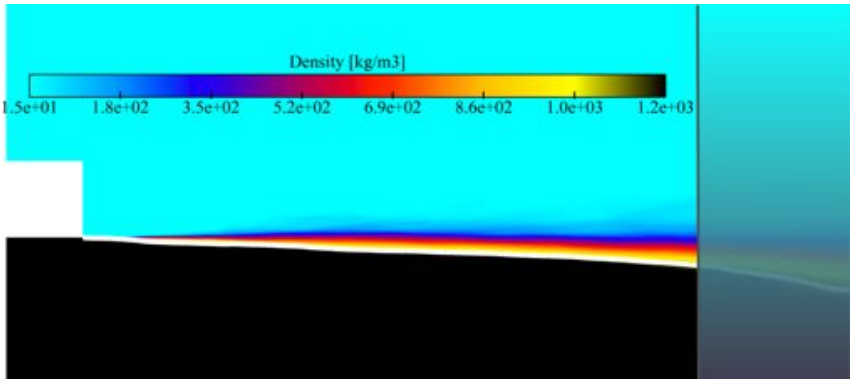

Figure 3.36: Average density field for the reacting flow. White iso-contour: $\rho = 0.9\ \rho^{in}_{O_2}$.

Figure 3.37(a) and Fig. 3.37(b) show the mean temperature and heat release rate fields, respectively. While the temperature is relatively homogeneous behind the splitter plate (because of turbulent mixing), the mean reaction rate clearly highlights two regions, as already depicted in Fig. 3.30: (1) a relatively steady flame is anchored at the lower corner of the lip (oxygen stream) and (2) an unsteady flame brush, with a vertical extent comparable to that of the splitter, is observed further downstream. It seems that in region (1), chemistry strongly dominates while in region (2), the turbulence level is high enough to control the flame front.

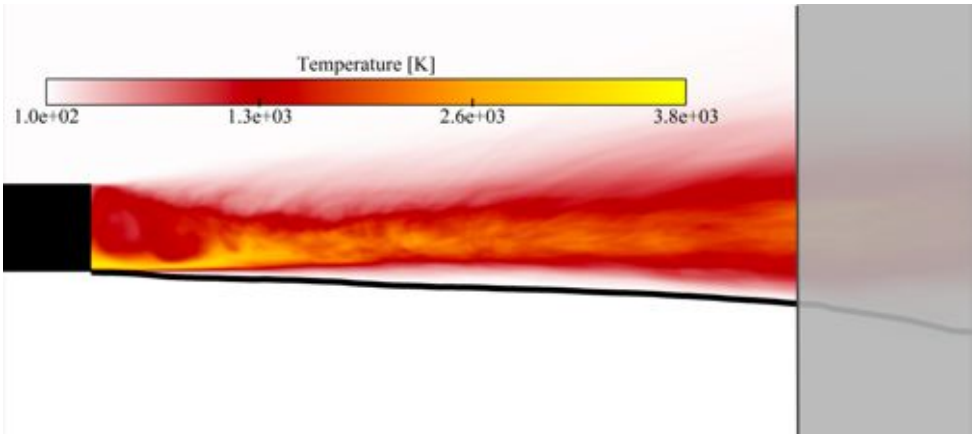

(a)

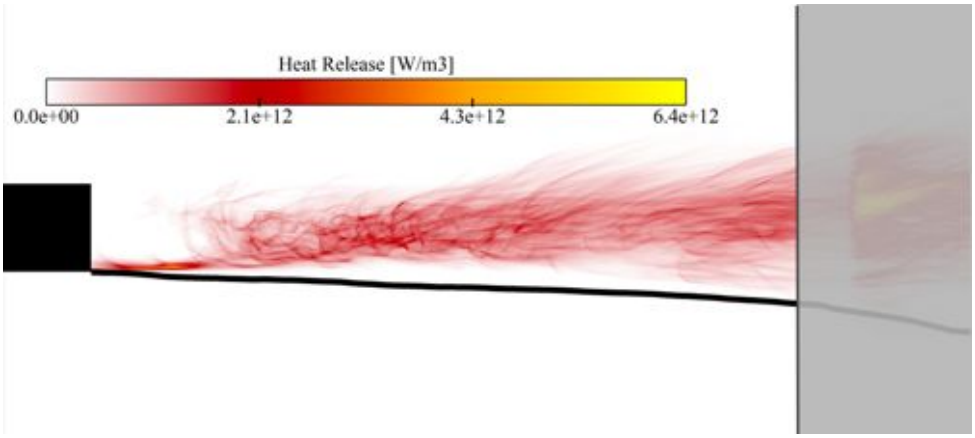

(b)

Figure 3.37: Average fields for the reacting flow. (a) Temperature. (b) Heat release rate. Black iso-contour: $\rho_{0.9}$.

3.3.5 Comparison of numerical results with existing experimental data

Observing the flame dynamics in a high-pressure environment is a difficult task and to the author's knowledge, only the research teams of the EM2C laboratory have been able to produce detailed measurements of both OH* and OH Planar Laser Induced Fluorescence (PLIF) for transcritical injections [Juniper *et al.* 2003,Singla *et al.* 2005,Candel *et al.* 2006, Singla *et al.* 2007].

In an attempt to compare the present numerical results with experimental flame visualizations, the OH mass-fraction fields at four instants is plotted in Fig. 3.38 and the OH-PLIF images of a transcritical H_2/O_2 flame at 6 MPa from [Singla *et al.* 2007] are shown in Fig. 3.39. In Fig. 3.38, the various combustion modes identified in Sec. 3.3.3 are clearly observed: strained-diffusion-flame elements and pocket combustion in the near-field region, and mixed combustion modes further downstream. In the PLIF images of Fig. 3.39, the flame appears much thicker and no such complex flame dynamics is observed. The numerical flame thickness is consistent with 1D laminar counterflow diffusion flames at strain rates comparable to the velocity gradient at injection that have a thickness ranging from $\delta = 80$ μm to $\delta = 30$ μm between $a = 19\ 10^3\ s^{-1}$ and $a = 190\ 10^3 s^{-1}$. Similarly, the numerical study of [Ribert *et al.* 2008] show that the flame thickness is small, even at low strain values (for instance, $\delta = 200$ μm, with $a = 2000$ s^{-1}, at 10 MPa) which is in the line of the present numerical results and tends to indicate that the flame should not be as thick as the splitter plate.

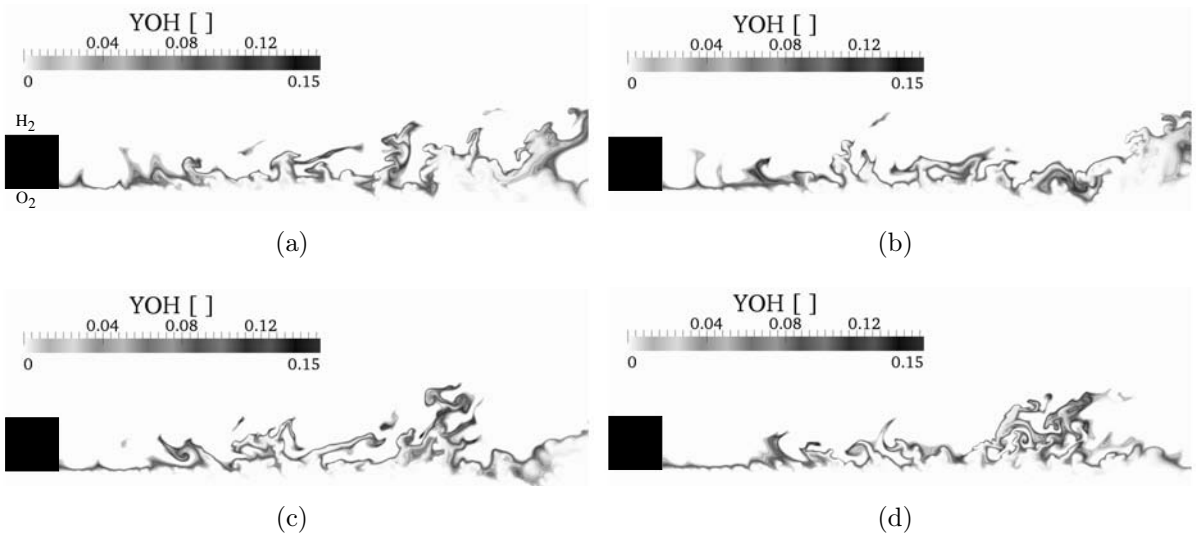

Figure 3.38: OH mass-fraction fields at four instants. Liquid oxygen and gaseous hydrogen are injected below and above the step, respectively.

To understand the discrepancy between simulation and experiment, it is then necessary to go back to the measurement technique. In a high-pressure reacting environment, due to the high Reynolds number, turbulent scales are smaller than at atmospheric pressure, and

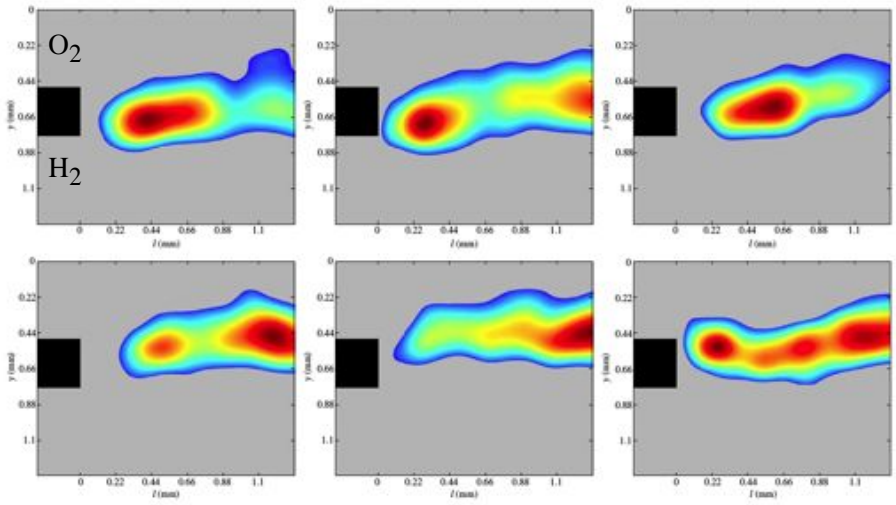

Figure 3.39: OH-PLIF images of the flame holding region. Liquid oxygen and gaseous hydrogen are injected above and below the step, respectively (opposite arrangement of Fig. 3.38). The OH distribution in the flame edge is shown on the standard color scale. p = 6.3 MPa (fig. 5 of [Singla *et al.* 2007])

require an increased level of spatial resolution and data acquisition rate. Unfortunately, optical diagnostics face several hurdles at high-pressures. The first one is light scattering due to large density gradients, which can deviate light path and thus optical signal. The second one is collisional quenching, which degrades the quality of PLIF. Due to the high density of cryogenic fluids, the excited state of radical species induced by laser sheet can relax to its equilibrium state without fluorescence emission, due to kinetic energy exchange while molecules are colliding together. This results in a low signal-to-noise ratio.

PLIF is also subject to blurring effects caused by curvature of the turbulent structures intercepted by the laser sheet, which is not infinitely thin. In [Singla *et al.* 2007], the thickness of the laser beam is 0.5 mm, which is equal to the splitter plate height in the present configuration.

Thus, to compare PLIF results with numerical results, the heat release rate should be integrated over a $1h$ distance in the spanwise direction. As the present computation is 2D, instead of a line-of-sight spatial average, a time average is shown in Fig. 3.40. The thickness of the time-averaged flame is now comparable to the splitter plate height, as in the experiment. This suggests that the PLIF measurements do not show a visualization of a cut through the flame front, but rather the flame brush due to spatial averaging in the spanwise direction. The thin diffusion flame located immediately behind the splitter plate, is very thin on the numerical results and may be within the noise of the PLIF signal. This could explain why the experiment seems to show a lifted flame, while the simulation shows an attached flame. However, further experimental studies would be needed to substantiate this claim.

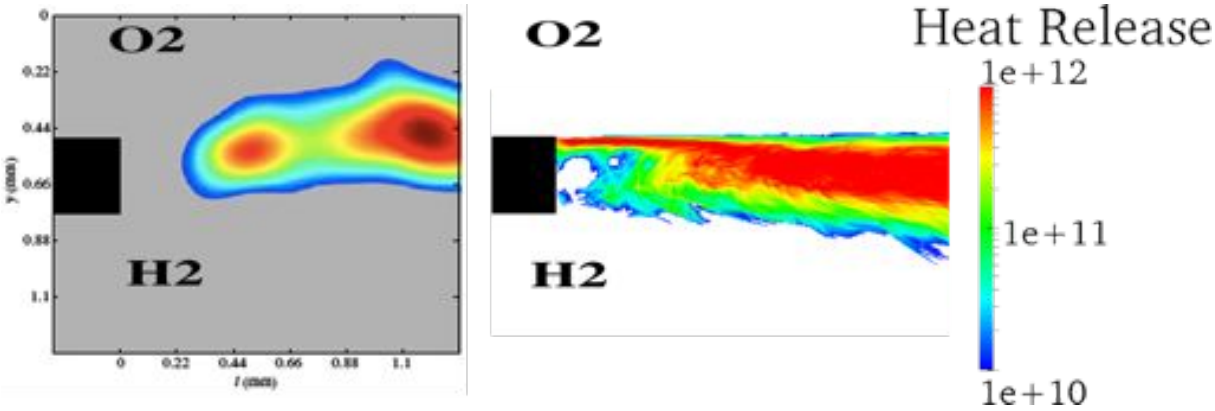

Figure 3.40: Comparison between experimental signal of OH PLIF [Singla *et al.* 2007] at transcritical conditions and time averaged heat release rate in the current simulation (the numerical visualization is upside down to compare with experimental visualization)

3.4 Conclusions

Simulations of a splitter-plate configuration representative of an injector of a Liquid Rocket Engine have been conducted. The dynamic and thermodynamic conditions are chosen to be representative of a real engine under steady operation. Both non-reacting and reacting configurations were computed, with a two-dimensional domain and full resolution of turbulence and chemistry.

Vortex shedding behind the injector lip has been shown to play an important role in the mixing of reactants, and is responsible for the formation of finger-like structures at the surface of the oxygen jet, which exhibits both large and small-scale structures. The Strouhal number of vortex shedding is $St = 0.2$, based on the convection speed of the coherent structures and their wavelength. In the non-reacting case, 100 grid points are sufficient to discretize the flow in the wake of the splitter plate and to obtain converged statistics.

In the reacting case, the large scale structures disappear in the presence of hot combustion products between the oxygen and hydrogen streams, which results in a less intense turbulent mixing that lowers the spreading angle of the oxygen jet. The flame is anchored at the splitter plate and is separated into two main regions: a steady diffusion flame between pure oxygen and a mixture of hydrogen diluted with combustion products, which sticks to the splitter plate, and a turbulent diffusion flame further downstream, containing strained non-premixed flame elements and burning pockets of reactants. The Damköhler number is sufficiently far from extinction so that the flame structure is similar to the H_2/O_2 non-premixed diffusion flame manifold, with a small scatter induced by dilution of the reservoirs by combustion products. This shows that one can legitimately use the equilibrium assumption in a turbulent combustion model for such a flow configuration.

The comparison of the present flame visualizations and OH-PLIF images tends to indicate that the flame thickness is actually much thiner than what is measured experimentally. This might stems from the finite-thickness of the laser sheet that induces a

spatial integration of the reaction zone in the spanwise direction.

Chapter 4

Large Eddy Simulations of a Transcritical H_2/O_2 Jet Flame Issuing from a Coaxial Injector, with and without Inner Recess

4.1 Introduction

Most high-performance Liquid Rocket Engines (LRE) are equipped with coaxial injectors, where a central dense jet is atomized by a high-speed outer jet, due to aerodynamic forces. The operating principle of these coaxial injectors is the same as air-blast atomizers, which are classical in aeronautical injection systems. As indicated by [Candel *et al.* 2006], systematic tests carried out on a wide variety of injection devices led to rapid adoption of such configurations, which ensure a smooth ignition transient and a stable nominal operation. In the past 50 years, most design parameters have been adjusted without a detailed understanding of flame dynamics, because of both limited experimental diagnostics and numerical capabilities.

About twenty years ago, a research-test facility for high pressure combustion of cryogenic propellants was built at ONERA (France) and incrementally upgraded over the years. Many experimental studies have been carried out in this facility, named Mascotte [Habiballah *et al.* 1996, Candel *et al.* 1998, Vingert *et al.* 1998, Habiballah *et al.* 1998, Haberzettl *et al.* 2000, Vingert *et al.* 2000, Pourouchottamane *et al.* 2001, CNES 2001, Vingert *et al.* 2002]. See [Habiballah *et al.* 2006] for a detailed description of the test bench, in its current version.

Taking advantage of the optical access to the combustion chamber, advanced laser techniques (mainly Coherent Anti-stokes Raman Spectroscopy (CARS) and Planar Laser Induced Fluorescence (PLIF)) and line-of-sight imaging (shadowgraphs and OH* emission) have allowed a precise monitoring of LOx/GH_2 and LOx/LCH_4 flame shapes and lengths, as well as an identification of controlling factors. Table 3 in [Candel *et al.* 2006] gives an overview of imaging studies conducted at Mascotte.

At supercritical pressure, the break-up of the LOx jet was shown to follow the fibrous regime, depicted in [Chigier & Farago 1992], where disturbances with small wavelengths develop at the LOx surface, due to the peeling induced by the high-speed outer jet. Two key parameters were identified: the momentum-flux ratio $J = \rho_{H_2} u_{H_2}^2 / \rho_{O_2} u_{O_2}^2$ and the recess length of the inner oxygen tube. Both an increase in J and in the inner recess length provokes a thicker flame brush and a shorter flame.

Above a critical value of the momentum-flux ratio, located around 10, combustion efficiency is greatly enhanced [Herding 1997].

The effects of the recess length have been studied in [Kendrick *et al.* 1999]. It was found experimentally that for operating points with a low momentum-flux ratio (the so-called 'C' operating points), recessing the inner LOx tube induced a better combustion efficiency, whereas such enhancement was not clearly observed on operating points with a high momentum-flux ratio ('A' operating points). A theoretical explanation has been proposed: the presence of the flame inside the recessed injector creates a reduction in the flow section of hydrogen, which results in an acceleration, increasing the momentum-flux ratio. This, in turn, greatly improves combustion efficiency if the $J = 10$ critical value is attained.

Another experimental and theoretical study from [Juniper *et al.* 2001, Juniper & Candel 2003b], has shown that even in the cold flow case, recessing the inner injection tube can trigger a wake-like absolute instability, which enhances far-field mixing and creates large sinuous wavelengths at the surface of the LOx surface.

On the numerical side, most studies have been conducted with RANS, to validate models against experimental results [Cheng & Farmer 2006, Poschner & Pfitzner 2009, Demoulin *et al.* 2009, Cutrone *et al.* 2010, Matuszewski 2011, Pohl *et al.* 2011]. Validating RANS models in the real-gas framework is crucial, since validated models can then be used for parametric design optimization in LRE development cycles. However, RANS is not able to capture unsteady features of the flow field which can have a great impact on the prediction of combustion efficiency, such as the wake-like absolute instability mentioned above, which justifies the use of LES in subsequent sections.

Only a few numerical studies have used LES as a tool for detailed understanding of flame dynamics inside LREs. For instance, [Masquelet *et al.* 2009] led a 2D-axisymmetric simulation of a multiple-injector combustor, and focused on wall heat flux induced by combustion. Transcritical LES of coaxial injectors have been conducted in [Schmitt *et al.* 2009, Schmitt *et al.* 2010a] and [Matsuyama *et al.* 2006, Matsuyama *et al.* 2010], where the flow complexity has been captured with great precision and good agreement with numerical experiments. These studies have shown the potential of LES in the context of LRE studies.

In [Schmitt 2009], the effects of the momentum-flux ratio increase between the A60 and C60 operating points were studied with LES, using the AVBP code, also used herein. The increased combustion efficiency in the A60 case was mainly attributed to an increased level of turbulent velocity fluctuations throughout the flame length, induced by the higher momentum-flux ratio. This shortens the dense core length by 20% as well as the flame length by 50%. Thus it has been found that both the near-field mixing and the far-field mixing are influenced by the momentum-flux ratio.

In the present chapter, the effects of the inner recess length on combustion characteristics is studied with two LES simulations, one without recess, and one with a recess length equal to one diameter of the LOx tube d_{O_2}, at the C60 operating point.

The objective is first to verify if, in agreement with theoretical derivations, an increase of momentum-flux ratio is indeed responsible for mixing enhancements. Then, a detailed description of the reacting flow field will complement the available experimental results

and provide more insight into turbulent combustion processes at stake inside a LRE.

4.2 Configuration and operating point

4.2.1 The Mascotte facility

In its current version, the Mascotte test bench enables the study of LOx/GH_2 , LOx/LH_2 and LOx/LCH_4 combustion at pressure ranging from 0.1 to 7 MPa. A square combustion chamber, with movable lateral windows, can be used for optical access to the combustion zone, as shown in Fig. 4.1. The combustion chamber is 400 mm long and the square section has a 50 mm side length. A coaxial injector is fed-in with oxygen at a maximum mass flow rate of 450 g/s, and a maximum hydrogen mass flow rate of 75 g/s. At the outlet, a chocked nozzle enables the adjustment of the chamber pressure. In the numerical simulations presented hereafter, this part is not included and pressure is imposed before the converging part of the nozzle.

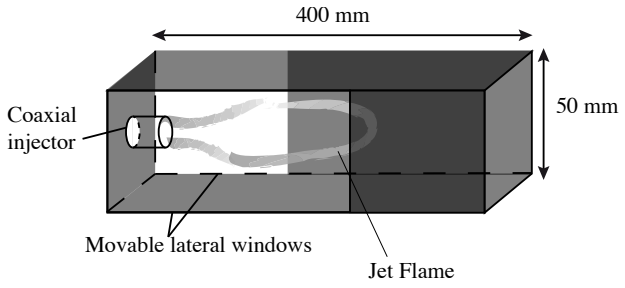

Figure 4.1: Square combustion chamber with optical access used in the Mascotte facility.

4.2.2 C60 operating point

For the C60 operating point, the combustion chamber pressure is 6 MPa, and the momentum flux ratio is below the $J = 10$ critical value. More details about the injection conditions is given in Sec. 4.3.2. The low momentum flux value of the C60 operating point makes the recess length effects more important, which is suitable to understand the basis mechanisms for combustion enhancement. The thermal power delivered by combustion at the C60 operating point is 1.5 MW ($= \dot{m}_{O_2} \frac{1+s}{s} \Delta h^0_{f,H_2O}$), which is representative of the power delivered by one of the 566 coaxial injectors of the Vulcain 2 engine ($= 1.5\ 10^9/566 = 2.6$ MW). Thus, understanding how the recess enhances combustion for this lab-scale flame might provide useful guidelines for the design of LRE injectors.

4.2.3 Characteristic numbers and scales

Figure 4.2(a) shows the dimensions of the non-recessed coaxial injector. The lip height has been increased from 0.3 mm in the experiments to 1.0 mm in the numerical simulations,

to allow a sufficient discretization of this flame stabilization zone and prevent numerical stiffness. If the oxygen flow is attached to the diverging part of the injector in the experiments, then the oxygen velocity would decrease and the momentum-flux ratio at the injection plane would be twice larger in the experiment than in the numerical simulation, although still smaller than the $J = 10$ critical value (see Tab. 4.1). This geometrical modification could thus have an impact on the near-injector flame dynamics, but still allows the study of the effects of recess. Moreover, a similar geometrical modification was done in [Schmitt *et al.* 2009] and have yielded good qualitative agreement with experimental results. The inner recess-length is shown on Fig. 4.2(b). It is the distance between the exit of the inner oxygen tube and the exit of the outer hydrogen tube. In what follows, 'NR' and 'R' will refer to the non-recessed and the recessed configurations, respectively.

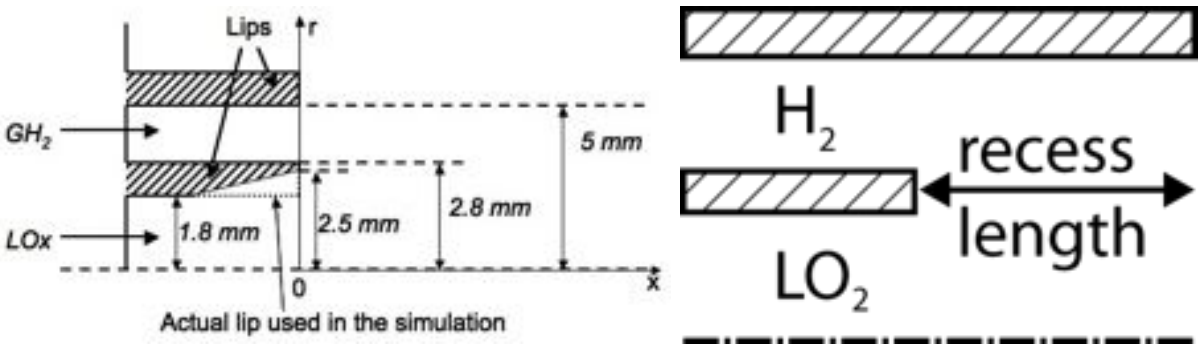

(a) (b)

Figure 4.2: Geometry of the coaxial injectors: a) dimensions and b) recess length.

Using Eq. 3.5, the convection speed of coherent structures in the inner shear layer is $U_{conv} = 23$ m/s. The characteristic convection time is: $\tau_{conv} = h/U_{conv} = 43$ μs.

4.3 Numerical setup

Mesh

Two different mesh resolutions have been used:

- a first mesh, called 'h5', with 5 cells within the lip height h and a total of 2 million nodes and 12 million tetrahedra, is used to compute the mean and RMS values for the whole flow field.
- a second mesh, called 'h10', with 10 cells within the lip height and a total of 21 million nodes and 120 million tetrahedra has then been used to check wether the global hydrodynamic instability, that is observed experimentally, is triggered with a finer mesh.

Figure 4.3 shows a cut of the h5 mesh, which is essentially composed of two regions: a near-injector region with a constant spacing $\Delta = h/5$ and a progressive mesh coarsening

following the opening of the hydrogen jet. Most of the grid points are placed in the near-injector region because the differences between the NR and R configurations presumably originate from this region. The h10 mesh is a homogeneous refinement of the h5 mesh, with characteristic lengths divided by 2 in each direction.

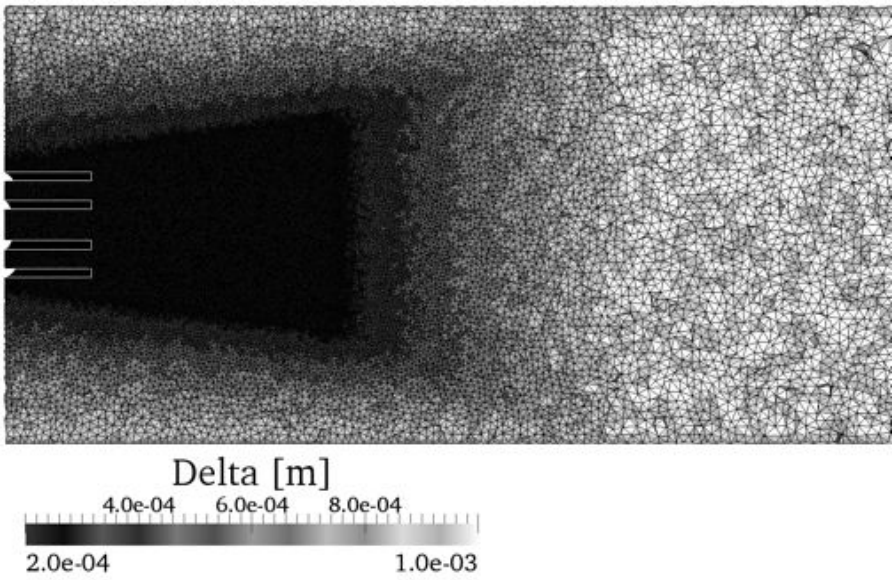

Figure 4.3: Cut of the h5 mesh, colored by $\Delta = V^{1/3}$, with V the local volume of cells.

Most numerical results shown in the present chapter uses the h10 mesh. When the h5 mesh is used, it is explicitly noted in the text and the legends of figures.

CPU cost

Using the flame length $L = 70\ d_{O_2}$ in Eq. 2.49, the hydrogen flow-through time is $T_{ft,H_2} = 10\ ms$ and the oxygen flow through time is $T_{ft,H_2} = 250\ ms$.

With the h5 mesh, the time step is $dt = 3.3\ 10^{-8} s$ and the number of iterations needed to simulate 30 T_{ft,H_2} ($\approx 1\ T_{ft,O_2}$) is $N_{30,ft,H_2} = 10^6$ (see Eq. 2.50). Thus, the simulation cost is approximately $50\ 10^3$ CPU hours (see Eq. 2.51), using the efficiency of AVBP on the VARGAS supercomputer at Idris (Power 6 processors at 4.7 GHz) $C_{i,n} = 70\ \mu s$.

With the h10 mesh, the cost is 2^4 times greater and requires $800\ 10^3$ CPU hours to obtain converged statistics throughout the flame length. At the moment, only $\tau = 2\ ms$ have been simulated. Thus, the length on which statistics are converged is smaller than $70\ d_{O_2}$:

$$\begin{aligned} L &= \frac{u_{H_2}}{10\tau} \\ &= 15\ d_{O_2} \end{aligned} \tag{4.1}$$

and only the statistics of the near-injector region will be analyzed with the h10 mesh.

Numerical scheme

A two-step Taylor-Galerkin finite-element scheme is used, called TTG4A [Colin & Rudgyard 2000]. It is third order in space and time.

4.3.1 Models

Equation of State (EOS)

The Soave-Redlich-Kwong (SRK) EOS is chosen here, because it allows a better representation of densities at low temperatures (far below the pseudo-boiling temperature) than the Peng-Robinson (PR) EOS (see Fig. 2.3). Thus, both the mass flow rate and the velocity of a transcritical injection are well represented using the SRK EOS. This would not be the case with the PR EOS as, due to the over-estimation of density, the injection velocity would be lowered to maintain the mass flow rate, possibly modifying the dynamic behavior of the coaxial jets.

Molecular Diffusion

As will be seen later on, the integral length scale is of the order of $l_t = h$ and the velocity fluctuations are of the order of $u' = 70$ m/s ($= 0.3\ u_{H_2}$) (see Fig. 4.12). Using the kinematic viscosity of the hydrogen stream and assuming a fully developed turbulent flow, the Kolmogorov scale is $\eta = 0.3\ 10^{-6}$ m (see Eq. 3.7).

On the other hand, the mesh filter size is $\Delta = 100\ \mu$m ($\Delta = 200\ \mu$m) for the h10 (h5) mesh. Thus $\Delta \gg \eta$, so that molecular diffusion is neglected in this chapter.

Turbulent Combustion Model

The turbulent combustion model that is used herein has been developed and validated in [Schmitt *et al.* 2010a], where both an atmospheric H_2/air and a transcritical LOx/GCH_4 jet flames have been convincingly compared to experimental data.

This model is based on the presumed beta function subgrid LES approach, including heat release in the fast chemistry limit [Peters 2001].

In Chap. 3, it has been shown that, at the stabilization point of a transcritical LOx/GH_2 flame, the scalar dissipation rate is sufficiently far from the extinction value, so that the flame structure is close to the non-premixed diffusion flame manifold and the equilibrium lines (see Figs. 3.35 and 3.7). Downstream of the stabilization point, scalar dissipation rates are lowered by turbulent mixing, as exemplified in Fig. 3.18. Thus, modeling combustion in the fast chemistry limit appears to be justified.

A single step reaction is assumed:

$$m_{H_2} + s\ m_{O_2} \rightarrow (1+s) m_{H_2O} \tag{4.2}$$

with m_k the mass of the k reactant and s the stoichiometric mass ratio (=8 for H_2/O_2 combustion).

For H_2/O_2 combustion considered herein, 3 species are transported: H_2, O_2 and H_2O. The mixture fraction is computed from the mass fractions of these species.

$$\mathcal{Z} = \frac{sY_{H_2} - Y_{O_2} + Y^0_{O_2}}{sY^0_{H_2} + Y^0_{O_2}}, \tag{4.3}$$

where the superscript 0 refers to the injection conditions.

For laminar flows, the Burke and Schumann solution [Burke & Schumann 1928] is directly used, where species mass fractions are piecewise-linear functions of the mixture fraction, as shown in Fig. 4.4. A source term is then computed for combustion products to relax the transported species mass fractions Y_k towards the equilibrium lines Y_k^e:

$$\dot{\omega}_k = \rho \frac{Y_k - Y_k^e}{\tau} \tag{4.4}$$

where τ is a relaxation time (a few acoustic time steps).

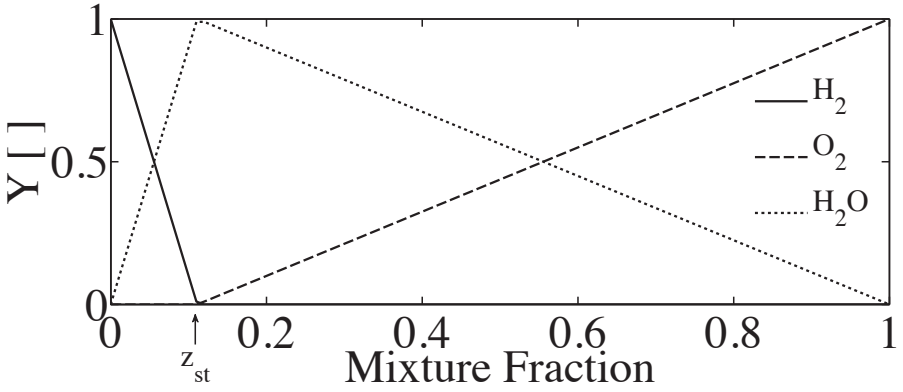

Figure 4.4: Species mass fraction as a function of mixture fraction, in the infinitely fast chemistry limit (Burke-Schumann solution).

For filtered turbulent flows, subgrid-scale flame/turbulence interactions are modeled by convolution of the Burke and Schmumann solution with the presumed-shape beta PDF P, that depends on the filtered mixture fraction $\widetilde{\mathcal{Z}}$ and on the subgrid-scale variance $\widetilde{\mathcal{Z}''}$:

$$\widetilde{Y_k^e}(\widetilde{\mathcal{Z}}, \widetilde{\mathcal{Z}''}) = \int_0^1 Y_k(\mathcal{Z}^*) P_{\widetilde{\mathcal{Z}}, \widetilde{\mathcal{Z}''}}(\mathcal{Z}^*) d\mathcal{Z}^* \tag{4.5}$$

The values of $\widetilde{Y_k^e}(\widetilde{\mathcal{Z}}, \widetilde{\mathcal{Z}''})$ are stored in a precomputed table that is accessed during the LES computation. The model requires to solve the transport equation for $\widetilde{\mathcal{Z}}$, while an algebraic expression is used to determine $\widetilde{\mathcal{Z}''}$ [Pierce & Moin 1998, Peters 2001]:

$$\widetilde{\mathcal{Z}''} = C\Delta^2 |grad(\widetilde{\mathcal{Z}})|^2 \tag{4.6}$$

with C a model constant. In [Schmitt *et al.* 2010a], the influence of this constant was shown to be small within the 0.1-0.5 range. Here, C is set to 0.05. Finally, the filtered species source terms are:

$$\overline{\dot{\omega}_k} = \overline{\rho} \frac{\widetilde{Y_k} - \widetilde{Y_k^e}}{\tau} \tag{4.7}$$

and the filtered heat-release rate is:

$$\overline{\dot{\omega}_T} = -\sum_{k=1}^{N} \Delta h_{f,k}^0 \overline{\dot{\omega}_k} \tag{4.8}$$

Note that this model is able to reproduce fast-burning stabilized flames only. Induction zones or dilution phenomena, as seen in Chap. 3, can not be reproduced.

Turbulent Viscosity

The subgrid-scale turbulence model is the WALE model, which is described in Sec. 2.3.2. This model sets turbulent viscosity to zero in pure-shear regions, which allows the development of coherent structures by shear instability and goes to 0 near walls. This is particularly important to capture the laminar to turbulent transition of jets. Turbulent viscosity is activated in regions with either large strain rates, large rotation rates, or both.

This model has been used in LES of supercritical and transcritical non-reacting nitrogen jets in [Schmitt *et al.* 2010b], as well as transcritical LOx/GCH_4 reacting flow [Schmitt *et al.* 2010a], in which numerical results have been favorably compared to experimental results.

4.3.2 Boundary Conditions

The pressure is imposed at 6 MPa, using NSCBC, before the converging nozzle, at the outlet of the combustion chamber shown in Fig. 4.1. The main scales and non-dimensional numbers characterizing the C60 operating point are summarized in Tab. 4.1. where τ_R

	T [K]	$\dot{m}$ [g/s]	ρ^{inj} [kg/m^3]	U^{inj} [m/s]	μ [Pa.s]	τ_R	Π_R	Re	Ma
O_2	83	100	1190	10	0.2 10^{-3}	0.5	1.2	1.8 10^5	0.01
H_2	275	45	5.1	234	7.4 10^{-6}	8.3	4.7	3.6 10^5	0.18

R_ρ	R_u	J	E
230	23	2.3	2.2

U_{conv} $[m/s]$	τ_{conv} $[\mu s]$	T_{ft,O_2} $[ms]$	T_{ft,H_2} $[ms]$
23	43	25	1.1

Table 4.1: Characteristic flow quantities for the C60 operating point

and Π_R (defined in Eqs. 1.9 and 1.10) are the reduced temperature and pressure, respectively. The oxygen flow-through time T_{ft,O_2} and the hydrogen flow-through time T_{ft,H_2}, are computed with $L = 70\ d_{O_2}$ and $U = U^{inj}$ in Eq. 2.50.

Oxygen is injected under transcritical conditions ($\tau_R < 1$, $\Pi_R > 1$), whereas hydrogen is supercritical ($\tau_R > 1$, $\Pi_R > 1$). This results in a large density ratio R_ρ of 80 (defined in Eq. 1.14).

The velocity ratio R_u (defined in Eq. 1.16) is large and induces fast-growing shear instabilities. The Mach number is very low in the oxygen stream and rather small in the GH_2 stream, so that compressibility effects are small.

The mixture ratio E, defined in Eq. 1.6, is lower than the stoichiometric mass ratio (s=8).

Inlet velocity fluctuations

Since the Reynolds number is very large, the flow inside the feeding lines is turbulent. The Kraichnan/Celik synthetic turbulence method is used to inject velocity fluctuations at the inlets of the simulation. This procedure was initially developed by [Kraichnan 1970, Smirnov *et al.* 2001] and has been adapted to compressible flows in [Guezennec & Poinsot 2009]. The mean and RMS velocity profiles imposed at the inlets have been determined by fitting 5^{th} order polynomials to the results of a companion LES of a fully-developed turbulent pipe flow at $Re = 10^5$. The normalized velocity profiles are plotted in Fig. 4.5. The polynomials for the mean axial velocity C_u and the RMS velocity fluctuations in cylindrical coordinates $C_{u_{RMS}}$, $C_{u_{r,RMS}}$, $C_{u_{\theta,RMS}}$ read:

$$\begin{aligned}
C_u(y_r) &= -30.21\ y_r^6 + 70.68\ y_r^5 - 62.39\ y_r^4 + 25.48\ y_r^3 - 4.921\ y_r^2 + 0.3395\ y_r + 0.9951 \\
C_{u_{RMS}}(y_r) &= -289.9\ y_r^6 + 724.1\ y_r^5 - 678.8\ y_r^4 + 296.8\ y_r^3 - 57.82\ y_r^2 + 4.657\ y_r + 0.9219 \\
C_{u_{r,RMS}}(y_r) &= -14.69\ y_r^6 + 47.1\ y_r^5 - 60.91\ y_r^4 + 34.45\ y_r^3 - 7.704\ y_r^2 + 0.7724\ y_r + 0.9843 \\
C_{u_{\theta,RMS}}(y_r) &= -70.71\ y_r^6 + 185.1\ y_r^5 - 187.1\ y_r^4 + 88.25\ y_r^3 - 18.07\ y_r^2 + 1.648\ y_r + 0.9685
\end{aligned} \tag{4.9}$$

where $y_r = (r - r^c)/R$ is a normalized distance from the injector wall, r is the distance from the injector axis and R is the feeding line half-height. In the oxygen stream, $r^c = 0$ and $R = d_{O_2}/2$. In the hydrogen stream, $r^c = (r_{o,H_2} + r_{i,H_2})/2$, $R = (r_{o,H_2} - r_{i,H_2})/2$, r_{i,H_2} and r_{o,H_2} are the inner and outer radius of the H_2 feeding line.

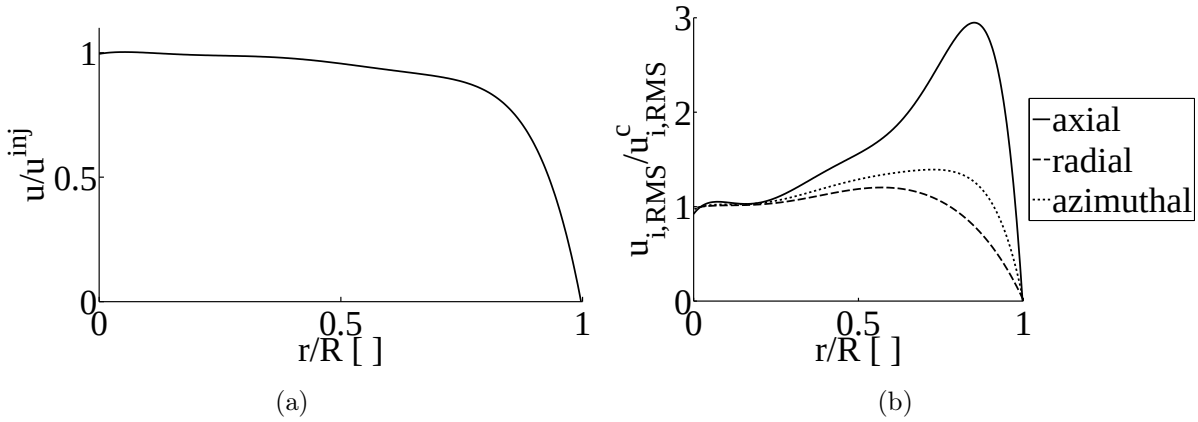

(a) (b)

Figure 4.5: Turbulence injection profiles: a) mean axial velocity and b) Root Mean Square velocity fluctuations. The superscript c refers to the centerline value.

The centerline mean axial velocity u^{inj} is given in Tab. 4.1 and is determined from the inlet mass flow rate. The centerline axial RMS velocities u^c_{RMS} are determined using a 4% turbulent intensity, which is the value obtained in the companion pipe flow LES:

$$I_t^c = \frac{u^c_{RMS}}{u^{inj}} \tag{4.10}$$

Finally, the ratio between axial and radial or azimuthal centerline velocity fluctuations is set to 0.65, which is the value obtained in the turbulent pipe flow LES.

Initial Solution

The combustion chamber is initially filled with H_2O at rest and at $T = T_{adiab}$ (T_{adiab} = 2200 K for the mixture ratio indicated in Tab. 4.1) and $P = 6$ MPa. Then H_2 and O_2 are progressively injected into the chamber. The reactants mix and burn when they reach the lip of the injector. The simulation is first run during 1 T_{ft,O_2}, which is the time needed for the oxygen jet to settle in the combustion chamber, and allows the domain-averaged quantities (mass fluxes, pressure, resolved kinetic energy, etc.) to reach a steady-state. The averaging of the flow is then started.

This procedure is only used for the h5 mesh. An established flow field from the h5 mesh is interpolated on the h10 mesh, and is used as an initial solution. The averaging of the flow is started directly after interpolation, since the flow field adapts rapidly to the increased resolution.

4.4 Results

First, the reference solution without recess is studied and validated against experimental results. The recessed configuration is then studied.

4.4.1 Reference solution without recess

First, instantaneous results are shown, to qualitatively describe the flow features. Then, time-averaged quantities are compared to experimental data.

4.4.1.1 Instantaneous Results

Fig. 4.6 shows cuts of instantaneous temperature and velocity fields. The flame is located between the high-speed outer hydrogen jet and the low speed central oxygen jet. There are essentially two regions in the flow field:

1. the near-injector region, in which the flame expands and pushes the hydrogen jet away from the axis of the oxygen jet. Vortical structures grow while convected downstream, as the hydrogen jet evolves towards fully-developed turbulence.

2. the far-field region, where vortical structures growth is prevented by the presence of the chamber walls and where the flame terminates.

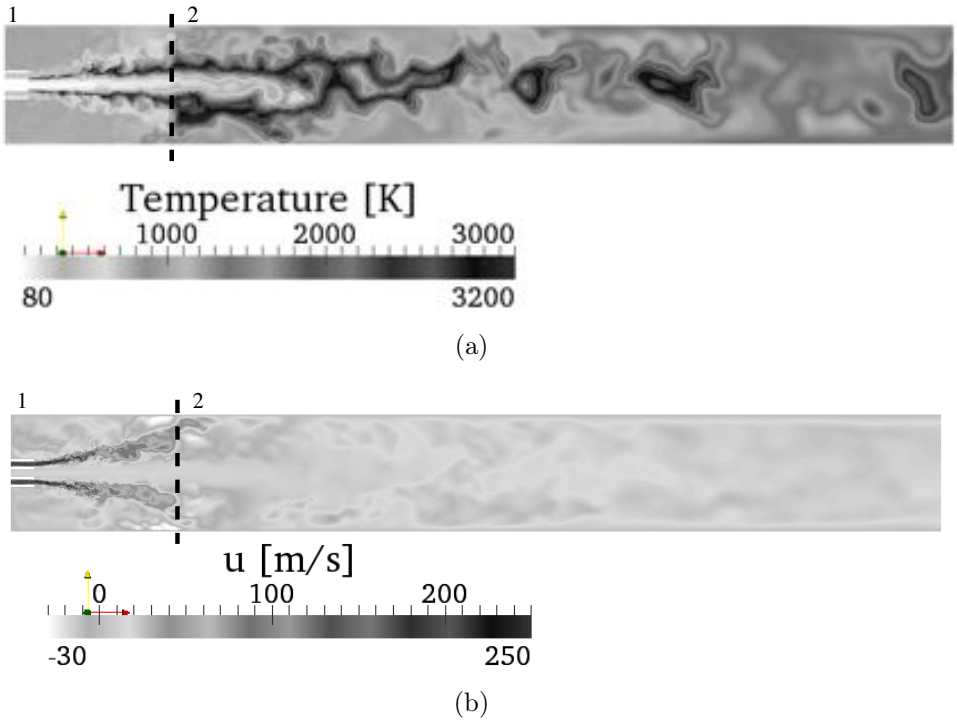

Figure 4.6: Instantaneous visualization of the reacting flow: a) temperature and b) axial velocity fields.

Due to the limited extent of the observation windows on the sides of the combustion chamber (see Fig. 4.1), only one of the two regions could be observed for a given hot fire test. Since in the second region, the flame expansion is hampered by the chamber walls, most of the imaging studies have been conducted with the observation windows mounted in front of the first region, where the flame expansion is driven by the injection conditions. Thus, in subsection sections, we will essentially focus on this first region.

A first qualitative comparison between the instantaneous numerical results and the experimental data presented in [Juniper 2001] is shown in Fig. 4.7. An OH^* field is compared to an iso-surface of temperature (T=1500 K) since they both represent the flame location. The flame is largely wrinkled in Fig. 4.7(b) and the visible wavelengths of the perturbations at the flame surface increase with axial distance, as the turbulent structures grow. The flame expansion appears to be retrieved in the numerical results. A shadowgraph is compared to the mixture fraction field since both of them locate the edges of the jets. The jets bear the same characteristics in the numerical simulation and in the experiment: the hydrogen jet rapidly transitions towards turbulence while the oxygen jet is more steady and largely penetrates the combustion chamber. Disturbances at the surface of the oxygen jet develop because of the turbulent motions.

Figure 4.8(a) shows a cut of an instantaneous velocity field in the near-injector region. Coherent structures develop in the inner and outer shear layers, due to the Kelvin-Helmholtz instability, which is qualitatively similar to what has been observed in the DNS studies of Chap. 3 (see Fig. 3.8). The two shear layers then merge and the hydrogen jet rapidly transitions towards developed turbulence, while the dense oxygen jet is very stable and is convected along the axis of the injector. The flame is located in the inner shear layer and is wrinkled by coherent structures and turbulence, as shown by a cut of an instantaneous temperature field in Fig. 4.8(b).

Figure 4.9 shows a comparison between instantaneous experimental and numerical results, showing the exit of the injector. Although a good qualitative agreement is obtained, the visual 'transition length' D, needed for the vortices to develop after the injection plane, seams slightly over-predicted.

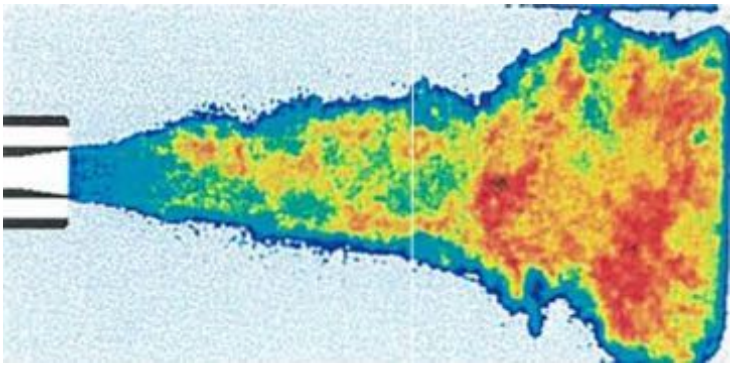

(a)

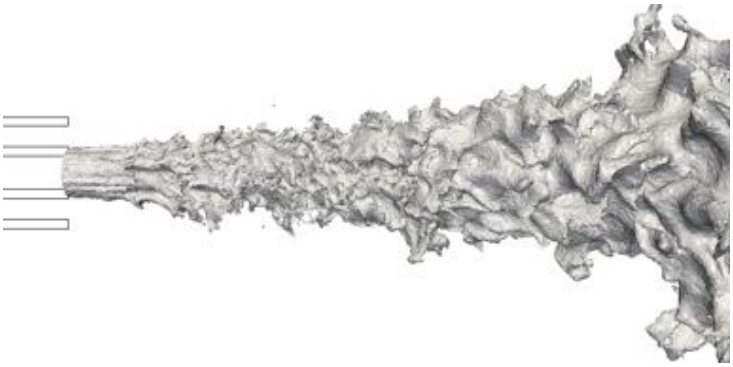

(b)

(c)

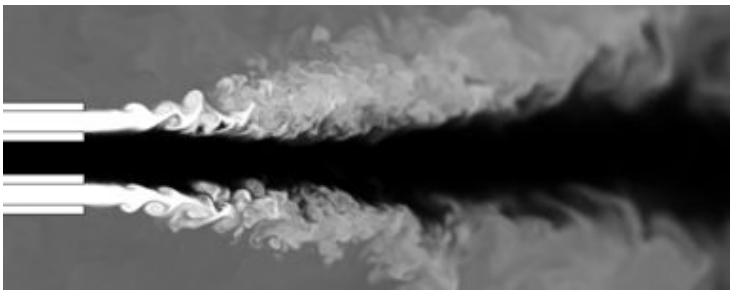

(d)

Figure 4.7: Qualitative comparison between instantaneous experimental ((a) and (c)) and numerical ((b) and (d)) visualizations of the reacting flow: (a) OH^* emission (b) $T = 1500$ K iso-surface (c) shadowgraph (d) mixture fraction between 0 (black) and 1 (white).

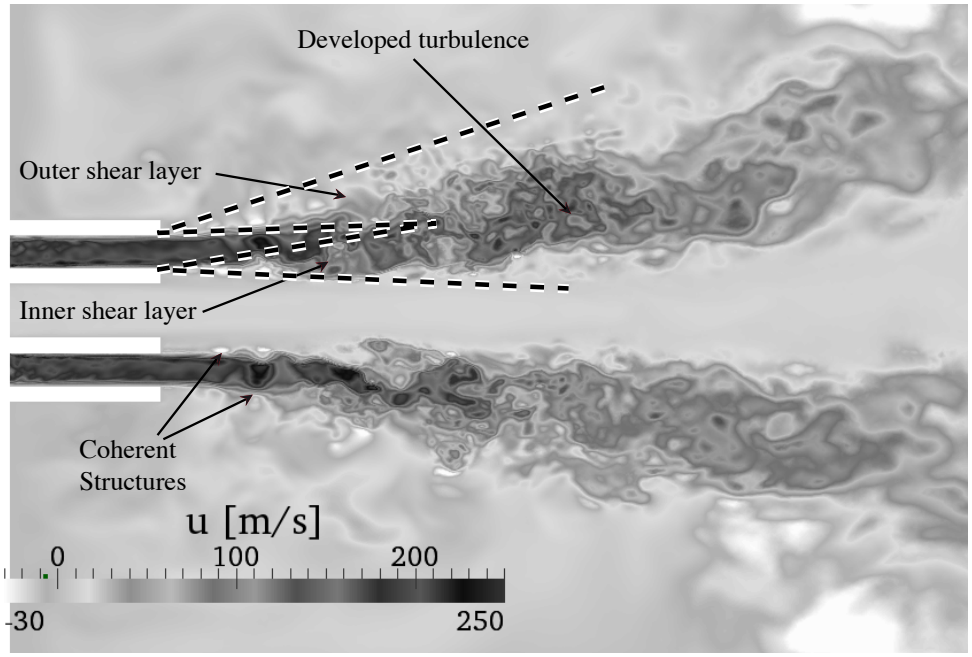

(a)

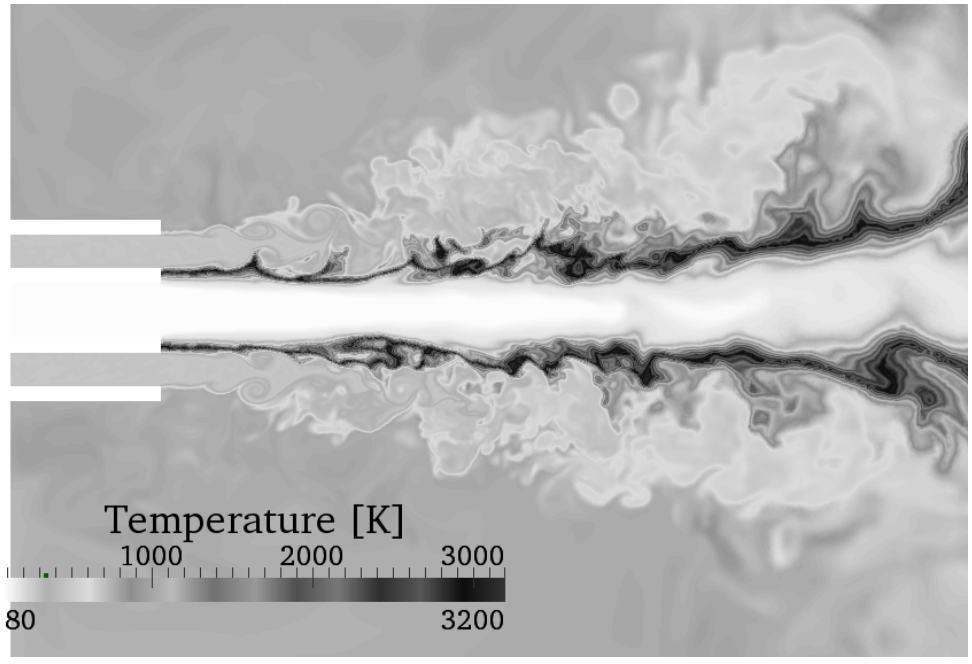

(b)

Figure 4.8: Instantaneous a) axial velocity and b) temperature cuts.

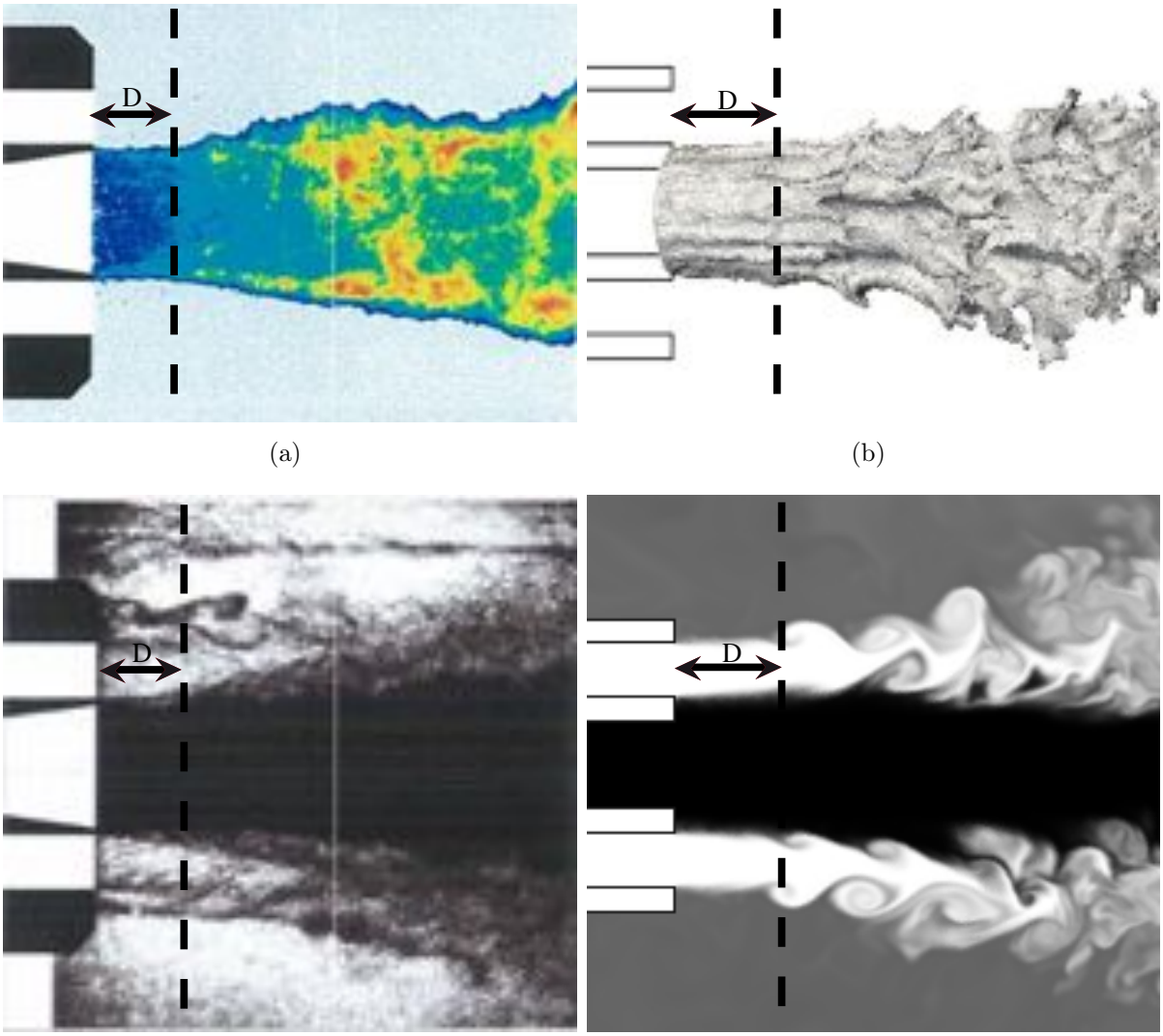

(a) (b)

(c) (d)

Figure 4.9: Qualitative comparison between instantaneous experimental ((a) and (c)) and numerical ((b) and (d)) visualizations of the near-injector region of the reacting flow: (a) OH^* emission (b) $T = 1500\ K$ iso-surface (c) shadowgraph (d) mixture fraction (black=0; white=1).

4.4.1.2 Time-averaged results

The objectives of this section are two fold. First, the comparison of time-averaged numerical and experimental results serves as a validation. Then, the comparison of numerical results obtained with the h5 and the h10 meshes allows to study the mesh convergence.

Figure 4.10 shows a cut of the average velocity magnitude (white=0 m/s; black=200 m/s) with superimposed streamlines in black and density iso-contours in grey (ρ=100, 500, 1000 kg/m^3) obtained with the h5 mesh. A corner and a central recirculation zone are generated by the impingement of the outer hydrogen jet on the chamber walls.

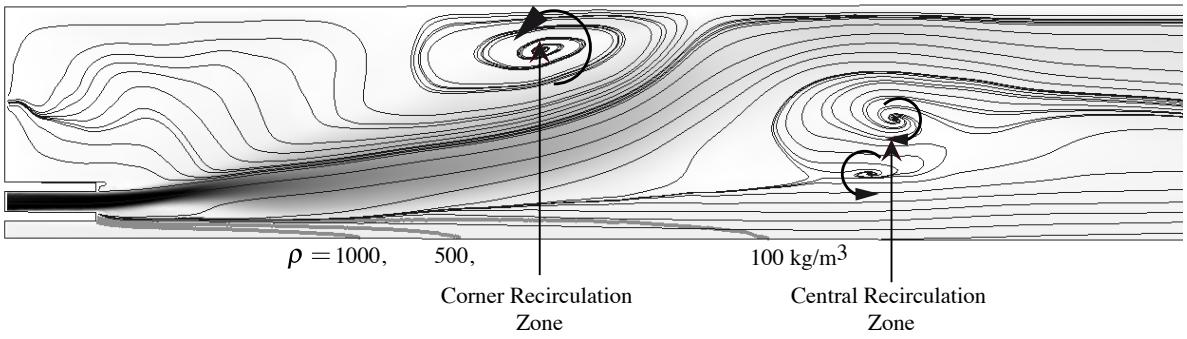

Figure 4.10: Cut of the average velocity magnitude (white = 0 m/s; black = 200 m/s) with superimposed streamlines in black and density iso-contours in grey (ρ=100, 500, 1000 kg/m^3), obtained with the h5 mesh.

The fields of mean temperature are shown in Figs. 4.11(b) and 4.11(c), for the h5 and h10 meshes and are compared to the Abel-transformed OH* emission of Fig. 4.11(a). The overall flame shape is correctly captured by both meshes, which tends to indicate that mesh convergence is already attained with the h5 mesh, for the NR configuration. There are three distinct zones in the flame:

- for $x < 2d_{O_2}$, the flame is largely stretched by developing coherent structures in the inner shear layer, and heat release is intense in this narrow region.
- for $2d_{O_2} < x < 20d_{O_2}$, a flame brush develops with turbulence.
- for $x = 20d_{O_2}$, because of the recirculation zones induced by the impingement of the hydrogen jet on the chamber walls (see Fig. 4.10) the flame expansion increases.

Figure 4.12 shows a cut of the RMS fluctuations of the axial velocity. The initial growth of the shear layers due to the formation of coherent structures is clearly observed, as well as vortex breakdown (local peak of RMS velocities $u_{RMS} \approx 70m/s$ at $x \approx 2d_{O_2}$). In the region of developed turbulence, the fluctuation levels slowly decrease as the turbulent structures grow. It is noteworthy that turbulence mostly develops outside the dense oxygen jet, in which the velocity fluctuations are very small. The density ratio between the oxygen and hydrogen jets clearly limits the turbulent mixing of the two reactants,

which is consistent with the DNS studies of Chap. 3 and with [Okong'o & Bellan 2002b].

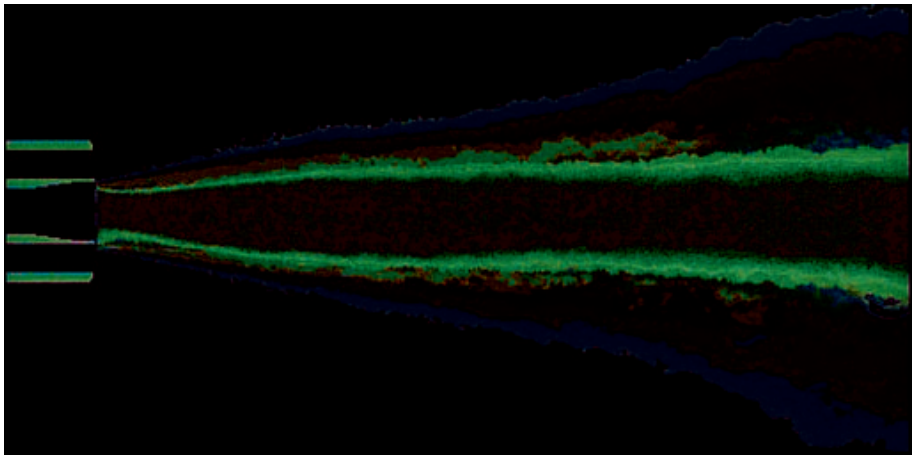

(a)

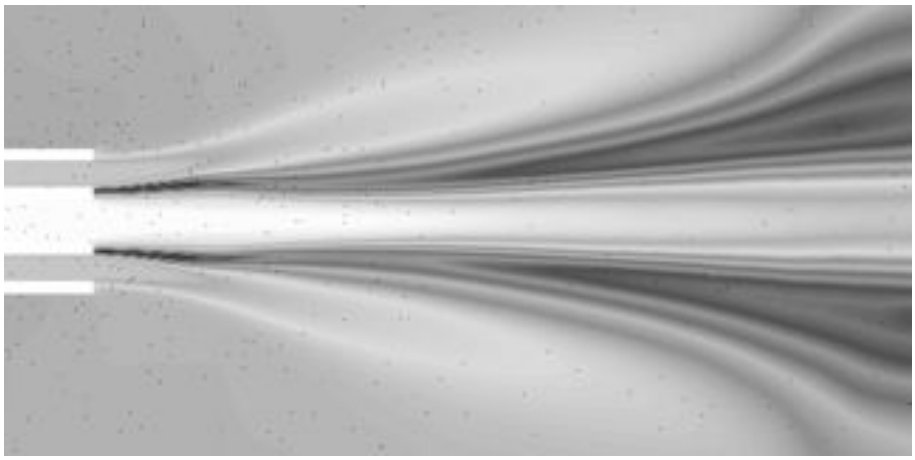

(b)

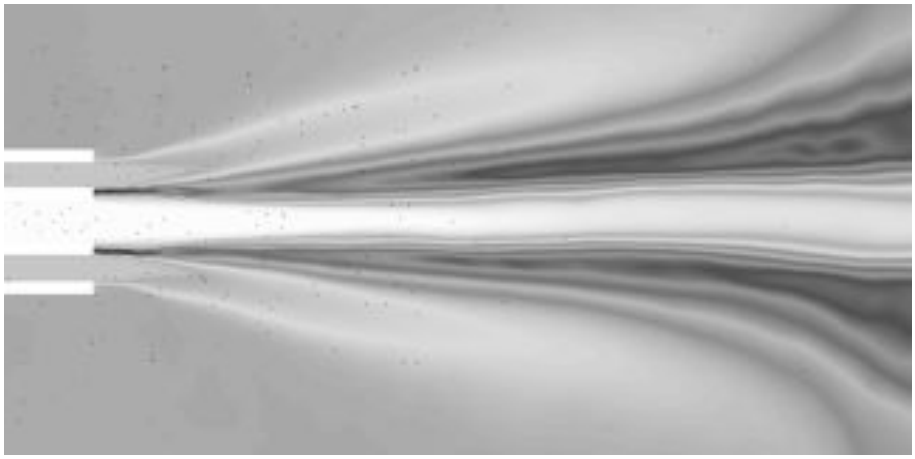

(c)

Figure 4.11: Time-averaged flame shapes, shown by (a) Abel-transformed OH^* emission, (b) mean temperature field with the h5 mesh, (c) mean temperature field with the h10 mesh (white=80 K; black=3200 K).

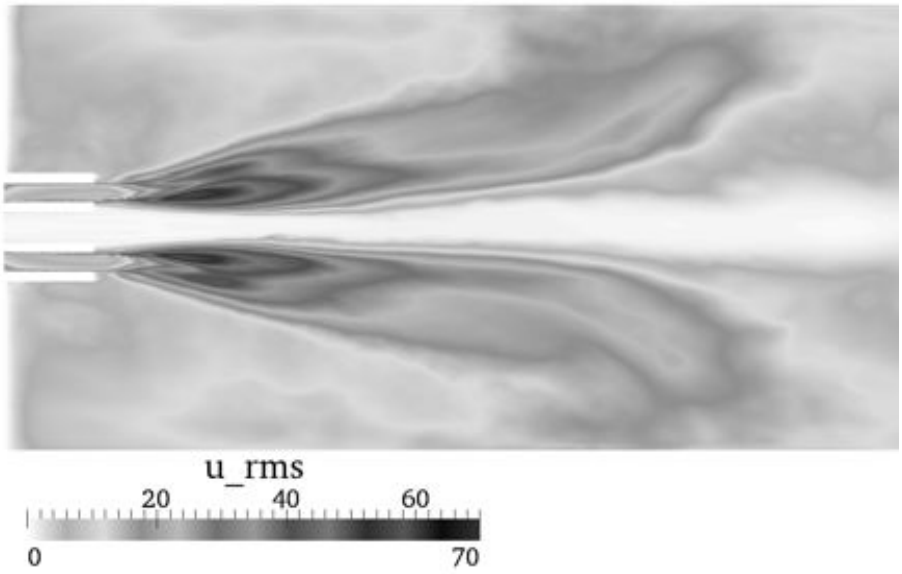

Figure 4.12: Cut of the RMS fluctuations of the axial velocity.

CARS measurements

In [Habiballah *et al.* 2006] and [Zurbach 2006], temperature measurements have been performed using Coherent Anti-Stokes Raman Spectroscopy (CARS), based on the spectral signature of hydrogen. The validation rate of these CARS measurements depends on the presence of hydrogen in the probe volume. Thus, the temperature measured by CARS is not exactly the time-averaged temperature, but a conditional time-averaged temperature T_α, which can be defined as the mean temperature given that the mass fraction of hydrogen Y_{H_2} is above a certain threshold α:

$$T_\alpha = \langle T | Y_{H_2} > \alpha \rangle \,, \tag{4.11}$$

where $\langle . \rangle$ is the time-average operator, and $|$ is the conditional statement. Here, T_α is obtained from 220 instantaneous temperature fields (with the h5 mesh), with α varied between 0 and 0.5, over a 12 ms period ($\approx 10\ T_{ft,H_2}$). The CARS mean temperature is obtained from 225 samples over a run of 15 s. The results are plotted on Fig. 4.13. The conditional mean temperature T_α is decreasing with α, since hydrogen is in excess in the combustion chamber and cools down combustion products.

From Fig. 4.13(a), it is clear that the probe lines at $y = 4\ mm$ and $x = 50\ mm$ cross the flame front, whereas the corresponding temperatures obtained by CARS (the circles in Figs. 4.13(b) and 4.13(d), respectively) do not seem to indicate the flame presence. With $\alpha = 0$ (time-averaged temperature), a peak in the temperature profile is indeed observed at the flame location. With $\alpha = 0.3$, the peak temperature is not observed anymore because of hydrogen dilution, and a good agreement with experimental data is obtained, which seems to indicate that the temperature measured by CARS is indeed a conditional temperature. The agreement between the conditional mean temperatures and the experimental data for the other probe lines, at $x = 15$ mm on Fig. 4.13(c) and $x = 100$ mm on Fig. 4.13(e) is less conclusive, although the shapes of the T_α profiles qualitatively follow the experimental trends.

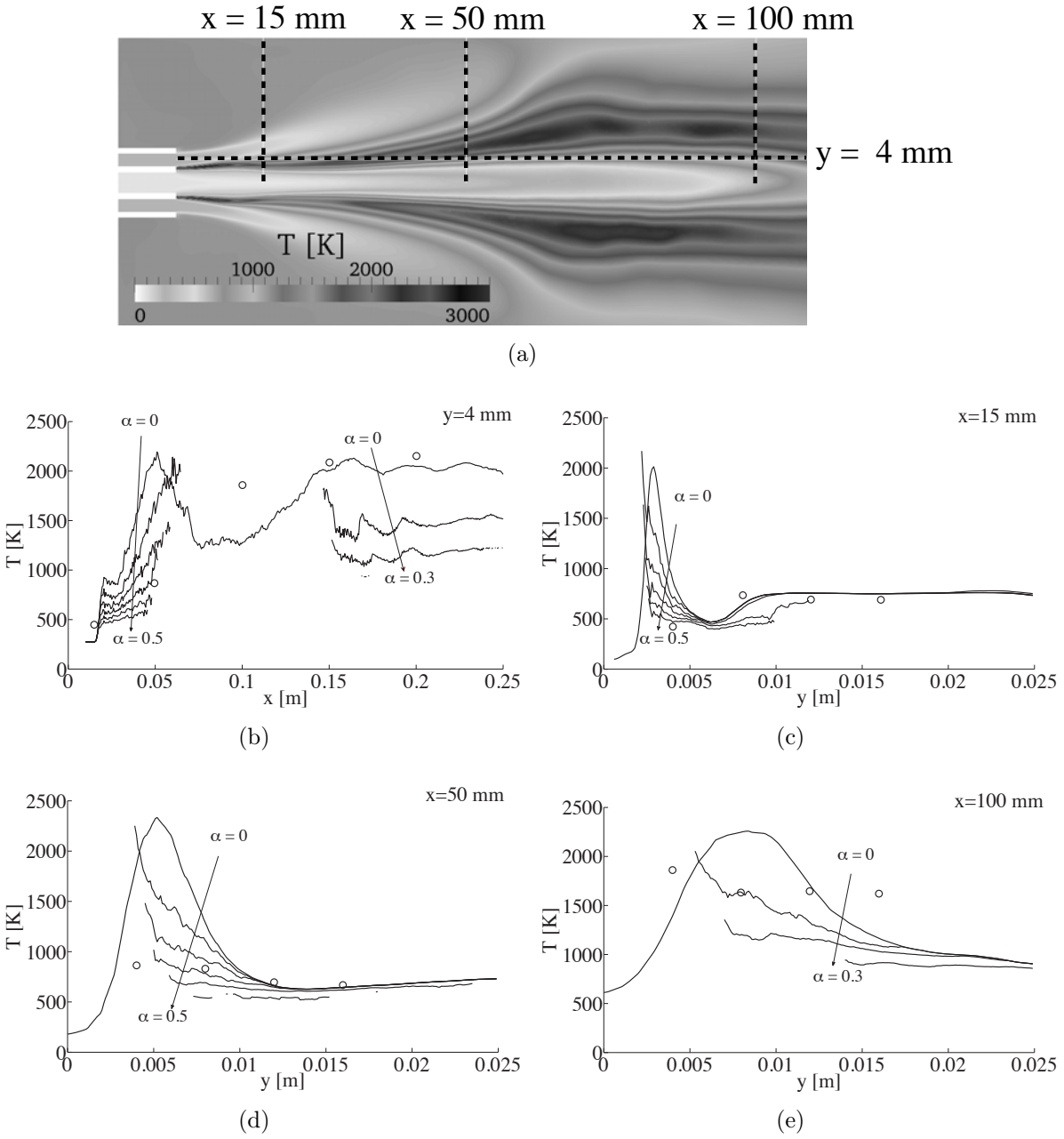

Figure 4.13: NR configuration: comparison between H_2 CARS measurements and conditional temperatures T_α, defined in Eq. 4.11. ○: CARS measurements from [Habiballah *et al.* 2006] and [Zurbach 2006]. (a) positions of the cuts (b) $y = 4$ mm, (c) $x = 15$ mm, (d) $x = 50$ mm, (e) $x = 100$ mm.

4.4.2 Effects of recess

Now that the flow field of the reference solution without recess has been characterized and validated against experimental data, the recessed configuration can be analyzed.

4.4.2.1 Instantaneous Results

Figure 4.14 shows an instantaneous iso-surface of temperature (=1500 K) and a cut of mixture fraction in the near-injector region of the R configuration. Coherent structures develop first in the recessed part of the inner shear layer and disturb the outer shear layer immediately at the injection plane. This provokes an early destabilization of the outer shear layer and a greater opening of the hydrogen jet.

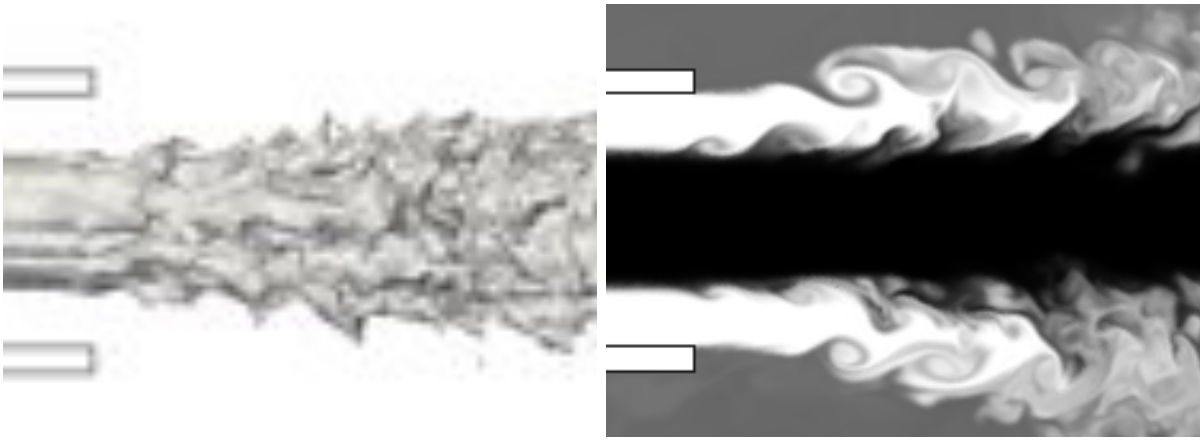

(a) (b)

Figure 4.14: Instantaneous visualization of the near-injector region in the R configuration: (a) iso-surface of temperature (=1500 K) and (b) mixture fraction field.

An instantaneous experimental shadowgraph from [Candel *et al.* 2006] is compared to the mixture fraction field in Figure 4.15. Although not as evidently as in the shadowgraph, large wavelengths are observable at the surface of the oxygen jet, whereas they are essentially absent from the NR configuration (see Fig. 4.7(d)).

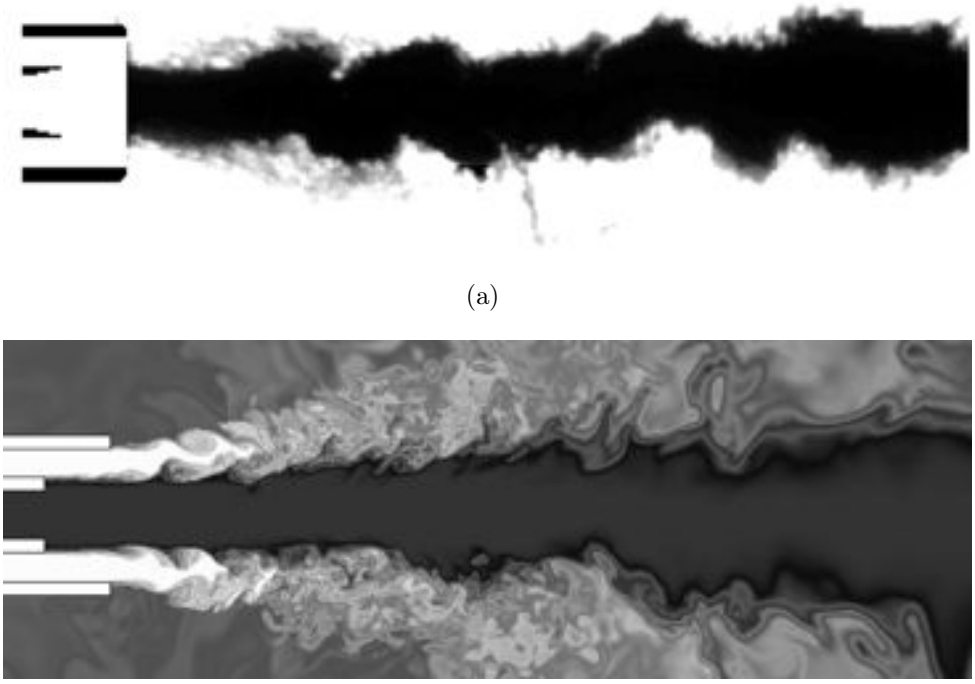

(a)

(b)

Figure 4.15: Qualitative comparison for the R configuration, between an instantaneous (a) experimental shadowgraph and (b) a mixture fraction field between 0 (black) and 1 (white).

4.4.2.2 Time-averaged Results

Figure 4.16 shows a comparison between time-averaged experimental and numerical results, in the near-injector region, for both the NR and R configurations. The recess length effects on the flow field in the near-injector region are qualitatively captured. In both the simulation and the experiment, the recess

- decreases the visual potential core length D of the outer hydrogen jet and
- increases slightly the opening angle of the outer hydrogen jet

The flame expansion is lower in the simulation than in the experiment. This might indicate that the flame brush is not well predicted in the near-field region, or that the mean temperature field do not directly correspond to the Abel-transformed OH^* emission.

To quantify the difference in combustion efficiency between the NR and R configuration, the local oxygen consumption rate is integrated in a small control volume, positioned at a varying distance x from the injector. The control volume is made of a slice perpendicular to the axis of the injector, that is swept on a distance equal to 1 d_{O_2}, as shown in Fig. 4.17(a). The integrated consumption rate of oxygen $\dot{\Omega}_{O_2}$ and the cumulated consumption rate of oxygen $I\dot{\Omega}_{O_2}$ read:

$$\dot{\Omega}_{O_2}(x) = \iiint_{V(x)} \dot{\omega}_{O_2} dV \tag{4.12}$$

$$I\dot{\Omega}_{O_2}(x) = \int_0^x \dot{\Omega}_{O_2}(x')dx', \tag{4.13}$$

and are plotted on Figs. 4.17(b) and 4.17(c). In Fig. 4.17(c), the cumulated consumption rate of oxygen is normalized by $I\dot{\Omega}_{O_2,max} = I\dot{\Omega}_{O_2}(x_{max})$, with x_{max} the maximum axial distance from the injector, in the simulation. Between $x/d_{O_2} = 0$ and $x/d_{O_2} = 2$, the consumption rate of oxygen increases very rapidly in both configurations, which corresponds to the initial roll-up of the flame front by coherent structures. At $x/d_{O_2} = 0$, a larger amount of oxygen is consumed in the R configurations because coherent structures develops earlier in the R configuration than in the NR configuration, as shown in Figs. 4.9(d) and 4.14(b), for instance. Between $x/d_{O_2} = 4$ and $x/d_{O_2} = 8$, the integrated consumption rate of oxygen is locally larger in the NR configuration than in the R configuration, which might come from a more intense vortex breakdown in the NR case. However, the oxygen consumption rate is overall larger in the R configuration, as indicated on the cumulated consumption rate of oxygen, on Fig. 4.17(c). Finally, the local consumption rate of oxygen slowly vanishes at the axial positions further downstream, as oxygen is depleted. It is clear from Fig. 4.17(c) that combustion efficiency is globally increased by the recess of the oxygen tube.

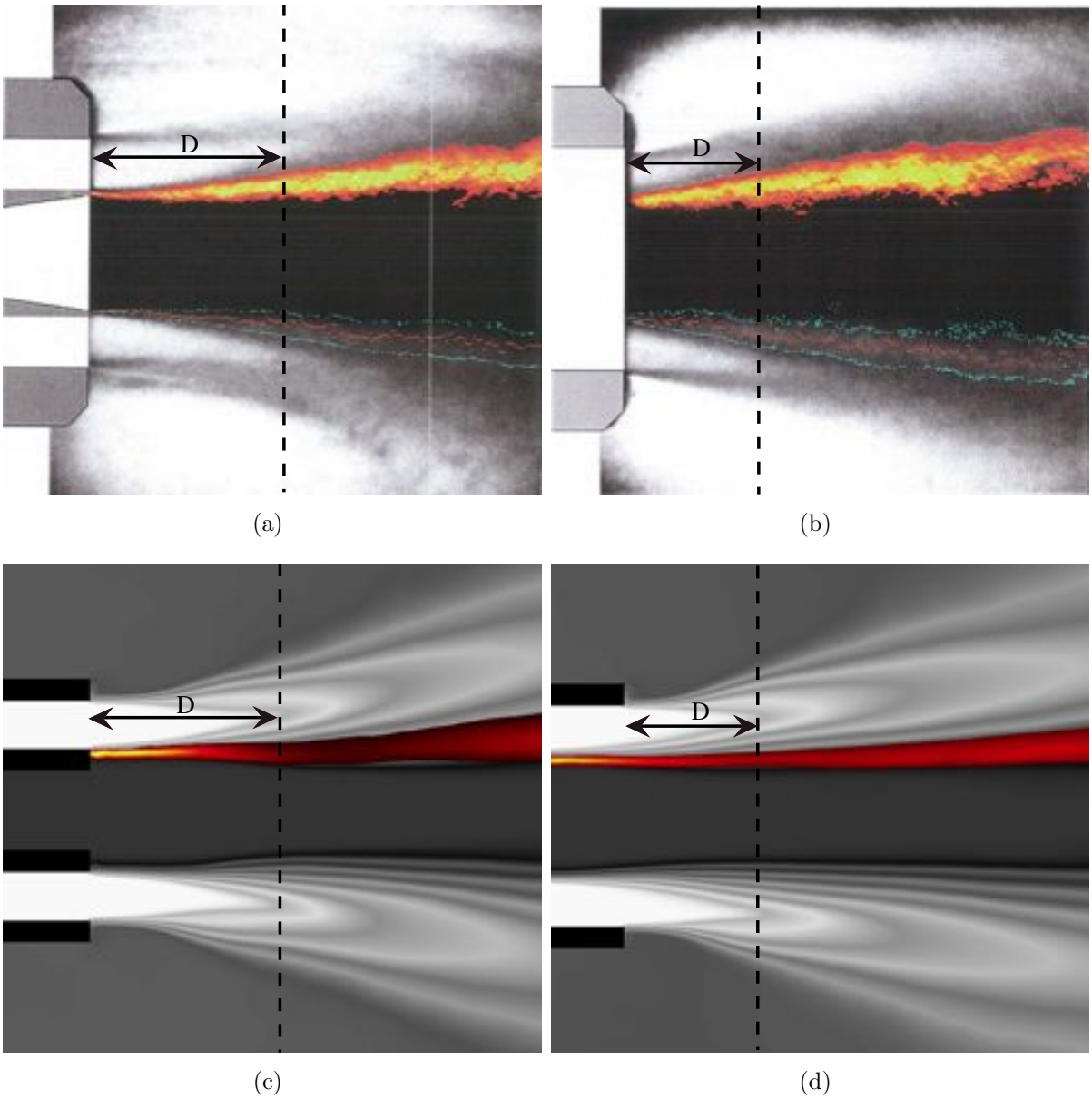

Figure 4.16: Time-averaged results. NR configuration (left) and R configuration (right): (a) and (b) are experimental shadowgraphs and Abel-transformed OH^* emissions, (c) and (d) are mixture fraction fields (black=0; white=1) and temperature fields (black=1000 K; yellow=3000 K).

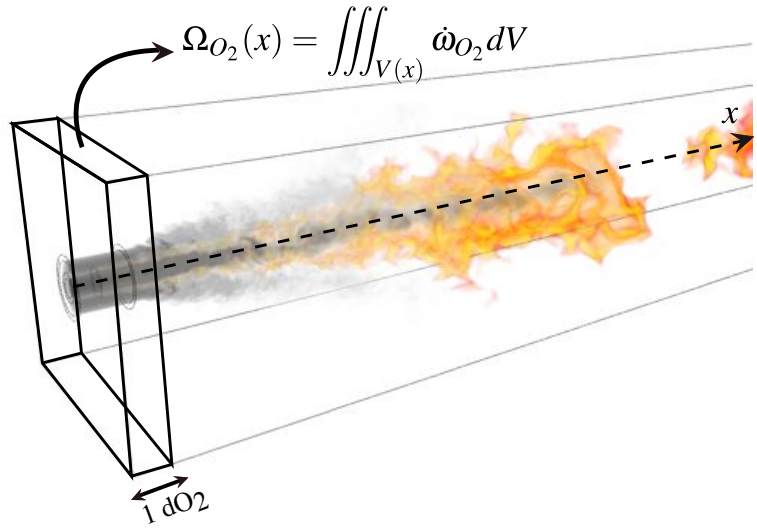

(a)

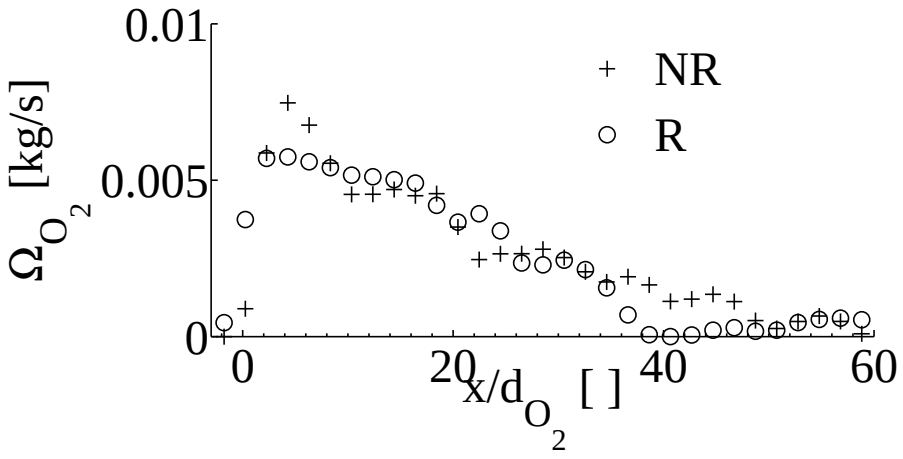

(b)

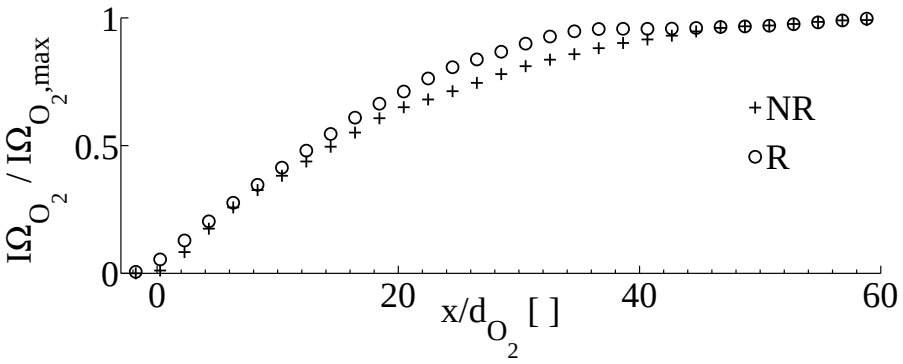

(c)

Figure 4.17: (a) Definition and (b) distribution of the integrated consumption rate of oxygen $\dot{\Omega}_{O_2}$. (c) Normalized and cumulated consumption rate of oxygen $I\dot{\Omega}_{O_2}/I\dot{\Omega}_{O_2,max}$ (defined in Eq. 4.13)

4.4.2.3 Characteristic Numbers impacted by the recess

Following the theoretical derivations of [Kendrick *et al.* 1999], the increase of momentum-flux ratio could provide an explanation for the enhancement of combustion efficiency in the R configuration. The local evolution of the momentum-flux ratio is thus plotted on Fig. 4.18(a), and the local velocity ratio is plotted on Fig. 4.18(b). 'Local' quantities are obtained by taking the value at the center of each stream, at a given axial position. Although the velocity ratio and the momentum-flux ratio are slightly increased at the injection plane in the R configuration, the critical $J = 10$ value is not crossed and is thus presumably not responsible for the combustion efficiency enhancement in the simulations.

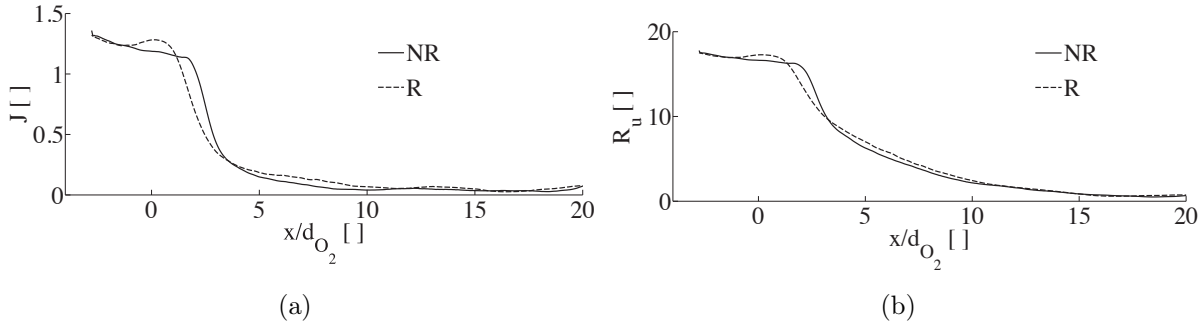

Figure 4.18: Axial evolution of (a) the momentum-flux ratio and (b) the velocity ratio.

4.5 Conclusions

Large Eddy Simulations have been conducted to study the effect of the recess of the inner oxygen tube on the combustion efficiency of a coaxial injector. First, the reference solution without recess have been validated against experimental data and have allowed a precise determination of the near-injector flame dynamics. Coherent structures develop in the inner and outer shear layers due to the Kelvin-Helmholtz instability. The outer hydrogen jet rapidly transitions towards turbulence whereas the oxygen jet penetrates deeply into the combustion chamber, because of the stabilizing effect of the large density ratio. The post-processing of the numerical results also tends to indicate that the temperature profiles measured by Coherent Anti-stokes Raman Spectroscopy (CARS) are conditional temperatures rather than time-averaged temperatures.

The enhancement of combustion efficiency have been retrieved in the numerical simulations of the recessed configuration. The effects of recess on the momentum-flux ratio is limited in the numerical simulations, and the most discernible effect is the shorter transition distance of the hydrogen jets, caused by the early development of coherent structures in the inner shear layer. This favors downstream mixing of hydrogen and oxygen and result in a better combustion efficiency.

Chapter 5
General Conclusions

The objective of the present work was to study the characteristics of reacting flows at operating conditions and in configurations relevant to Liquid Rocket Engines (LREs), with high-fidelity unsteady numerical simulations.

The first hurdle to overcome is the transport of transcritical density gradients, which requires numerical stabilization. This numerical filtering requires special attention in the real-gas framework because of the non-linearity of the equation of state, which can induce spurious velocity disturbances in the computed flow field. The solution that has originally been proposed in [Schmitt 2009], is based on a consistent thermodynamic treatment of the numerical dissipation terms and the theoretical background of this method has been reinforced here.

In Chap. 3, a Direct Numerical Study of turbulent mixing and combustion in the near-injector region of Liquid Rocket Engines has been conducted, at an unprecedented resolution. Vortex shedding behind the injector lip has been shown to play an important role in the mixing of reactants, and is responsible for the formation of finger-like structures at the surface of the oxygen jet. The Strouhal number of vortex shedding is $St = 0.2$, based on the convection speed of the coherent structures and their wavelength. This non-dimensional frequency might play an important role, if coupled with the eigen modes of the injection lines or the combustion chamber. In the reacting case, the flame stays attached to the injector rim by a steady-diffusion flame between the pure oxygen stream and a mixture of hydrogen diluted by a varying level of recirculated hot gases. Further downstream, the diffusion flame is wrinkled by vortex shedding and the forming finger-like structures are split into pockets of reactants that increase the reacting surface. Although the combustion modes are visually complex, the global flame structure stay close to the H2/O2 non-premixed manifold, with a small scatter induced by dilution of the unsteady reservoirs with combustion products.

In Chap. 4, two Large Eddy Simulations of a transcritical H_2/O_2 jet flame issuing from a coaxial injector, with and without inner recess have been conducted. The combustion enhancement induced by the inner recess of the oxygen tube has been retrieved in the simulations. The recess triggers the early development of coherent structures in the confined inner shear layer that induces a better turbulent mixing further downstream. This shows that LES is a promising tool for predicting in advance the effects of design parameters and might play an important role in the development of next-generation injectors.

Appendix A

Thermodynamic derivatives

A.1 Getting the density from (P,T,Y_i)

A.1.1 From the EOS to the cubic polynomial

Multiplying Eq. 2.46 by the two denominators of the RHS gives:

$$\begin{aligned} P\,(v-b)\,D &= RTD - \theta\,(v-b) \\ PDv - D\,(Pb+RT) + \theta v - \theta b &= 0 \end{aligned} \tag{A.1}$$

Introducing $e_n = (Pb + RT)$ and developing PDv gives:

$$\begin{aligned} PDv &= P\left(v^3 + d_1 b v^2 + d_2 b^2 v\right) \\ &= Pv^3 + Pd_1 b v^2 + Pd_2 b^2 v \end{aligned} \tag{A.2}$$

Gathering the coefficients gives:

$$Pv^3 + (Pd_1 b - e_n)\,v^2 + \left(Pd_2 b^2 - e_n\,d_1 b + \theta\right) v - e_n\,d_2 b^2 - \theta b = 0 \tag{A.3}$$

The final cubic polynome reads:

$$\begin{aligned} a_3 v^3 + a_2 v^2 + a_1 v + a_0 &= 0 \\ \text{with } a_0 &= -b\,(\theta + e_n\,d_2 b) \\ a_1 &= Pd_2 b^2 - e_n\,d_1 b + \theta \\ a_2 &= Pd_1 b - e_n \\ a_3 &= P \end{aligned} \tag{A.4}$$

NB : When using the perfect gas EOS, the coefficients given in Eq. A.4 cannot be used. Indeed, $D = 1$ in the perfect gas case, which totally changes the distribution of the polynome coefficients.

A.1.2 The Cardan method

The Cardan method gives the root of any third order polynome, so one can solve Eq. 2.47 directly to get the molar volume v. Although the solution of the Cardan Method is well known (see for instance [Polyanin & Manzhirov 2007]), the demonstration is recalled here:

Start from a third order polynome with real coefficients a_i

$$a_3 x^3 + a_2 x^2 + a_1 x + a_0 = 0 \tag{A.5}$$

Divide by a_3 to obtain the normalized form

$$x^3 + b_2 x^2 + b_1 x + b_0 \quad \text{with} \quad b_i = \frac{a_i}{a_3} \tag{A.6}$$

Substitute $x = y - b_2/3$ to eliminate the quadratic term

$$y^3 + py + q = 0 \tag{A.7}$$

$$\text{with } p = b_1 - \frac{b_2^2}{3} \tag{A.8}$$

$$q = 2\left(\frac{b_2}{3}\right)^3 - \frac{b_1 b_2}{3} + b_0 \tag{A.9}$$

Two new variables u and v are defined, so that:

$$y = u + v \tag{A.10}$$

where v is NOT the molar volume here. As a new degree of freedom is introduced, a relation between u and v must be introduced later. Inserting Eq. A.10 into Eq. A.9 gives:

$$\begin{aligned} u^3 + 3uv\,(u+v) + v^3 + p\,(u+v) + q &= 0 \\ u^3 + v^3 + (3uv + p)\,(u+v) + q &= 0 \end{aligned} \tag{A.11}$$

Following Cardan's idea, let's impose $(3uv + p) = 0$, in order to simplify Eq. A.11. This condition has the following consequences:

$$(3uv + p) = 0 \;\Leftrightarrow\; uv = -\frac{p}{3} \tag{A.12}$$

$$\Rightarrow\; u^3 v^3 = -\left(\frac{p}{3}\right)^3 \tag{A.13}$$

Inserting Eq. A.12 into Eq. A.11 gives:

$$u^3 + v^3 = -q \tag{A.14}$$

The sum and the product of u^3 and v^3 are known using Eq. A.13 and Eq. A.14. Hence, u^3 and v^3 are the roots of the second order polynome

$$Z^2 + qZ - \left(\frac{p}{3}\right)^3 = 0 \tag{A.15}$$

(because $(Z - u^3)(Z - v^3) = Z^2 - (u^3 + v^3)Z + u^3 v^3$).

The discriminant of Eq. A.15 is

$$\Delta = q^2 + 4\left(\frac{p}{3}\right)^3 \tag{A.16}$$

so that

$$\text{if } \Delta \geq 0 \quad u^3 = -\frac{q}{2} + \frac{\sqrt{\Delta}}{2} \quad \text{and} \quad v^3 = -\frac{q}{2} - \frac{\sqrt{\Delta}}{2} \tag{A.17}$$

$$\text{if } \Delta < 0 \quad u^3 = -\frac{q}{2} + \frac{i\sqrt{-\Delta}}{2} \quad \text{and} \quad v^3 = -\frac{q}{2} - \frac{i\sqrt{-\Delta}}{2} \tag{A.18}$$

As u and v are complex numbers, there are 3 solutions for u and v in Eq. A.17 and also 3 solutions for u and v in Eq. A.18.

$$u_k = \left(u^3\right)^{1/3} exp(i\frac{2k\pi}{3}) \quad k = 0, 1, 2 \tag{A.19}$$

For example, if $\Delta > 0$, Eq. A.17 implies

$$u_1 = \left(-\frac{q}{2} + \frac{\sqrt{\Delta}}{2}\right)^{1/3} \quad \text{or} \quad u_2 = u_1 exp(i\frac{2\pi}{3}) \quad \text{or} \quad u_3 = u_1 exp(i\frac{4\pi}{3}) \tag{A.20}$$

$$v_1 = \left(-\frac{q}{2} - \frac{\sqrt{\Delta}}{2}\right)^{1/3} \quad \text{or} \quad v_2 = v_1 exp(i\frac{2\pi}{3}) \quad \text{or} \quad v_3 = v_1 exp(i\frac{4\pi}{3}) \tag{A.21}$$

However, two constraints lower the number of possible solutions for y:

$$y = u + v \quad \text{is a real number} \tag{A.22}$$

$$uv = -\frac{p}{3} \tag{A.23}$$

If $\Delta > 0$

Then only the main roots (u_1, v_1) (which are expressed in Eqs. A.20 and A.21) simultaneously satisfy the constraints of Eq. A.22 and Eq. A.23. Hence, if $\Delta > 0$ there is only one real root:

$$X_1 = u_1 + v_1 - \frac{b_2}{3} \tag{A.24}$$

$$X_1 = \left(-\frac{q}{2} + \frac{\sqrt{\Delta}}{2}\right)^{1/3} + \left(-\frac{q}{2} - \frac{\sqrt{\Delta}}{2}\right)^{1/3} - \frac{b_2}{3} \tag{A.25}$$

If $\Delta < 0$

First, let's notice that $\Delta = q^2 + 4\left(\frac{p}{3}\right)^3 < 0$ implies $p < 0$.

Then, let's express u^3 in Eq. A.18 under exponential form:

$$u^3 = U_3 exp(i\phi) \tag{A.26}$$

$$U_3 = ||u^3|| = \sqrt{\left(\frac{q}{2}\right)^2 - \frac{\Delta}{4}} = \sqrt{-\left(\frac{p}{3}\right)^3} \tag{A.27}$$

$$\phi = arccos\left(Re(u^3)/||u^3||\right) = arccos\left(-\frac{q}{2}/\sqrt{-\left(\frac{p}{3}\right)^3}\right) \tag{A.28}$$

. So that the main cubic root of u^3 reads:

$$\left(u^3\right)^{1/3} = U_3^{1/3} exp(i\phi/3) \tag{A.29}$$

$$= \sqrt{-\left(\frac{p}{3}\right)} exp(i\phi/3) \tag{A.30}$$

Then Eq. A.19 can be written under exponential form:

$$u_k = \sqrt{-\left(\frac{p}{3}\right)} exp\left(i\frac{\phi + 2k\pi}{3}\right)$$

As y is a real number and is a sum of two complex numbers ($y = u + v$) then v is the complex conjugate of u

$$y = u + \bar{u}$$

. There are thus three real roots:

$$\begin{aligned} y_k &= u_k + \bar{u_k} \quad k = 0, 1, 2 && \text{(A.31)} \\ &= 2Re(u_k) \quad k = 0, 1, 2 && \text{(A.32)} \\ &= 2\sqrt{-\frac{p}{3}} cos\left[\left(\frac{\phi + 2k\pi}{3}\right)\right] \quad k = 0, 1, 2 && \text{(A.33)} \end{aligned}$$

Consequently, Eq. A.23 is satisfied

$$\begin{aligned} u_k v_k &= u_k \bar{u_k} = ||u_k||^2 \quad k = 0, 1, 2 && \text{(A.34)} \\ &= -\frac{p}{3} && \text{(A.35)} \end{aligned}$$

Finally, if $\Delta < 0$, the three real solutions of Eq. A.5 are:

$$\begin{aligned} X_k &= 2\sqrt{-\frac{p}{3}} cos\left(\frac{\phi + 2k\pi}{3}\right) - \frac{b_2}{3} \quad k = 0, 1, 2 && \text{(A.36)} \\ \text{with } \phi &= arccos\left(-\frac{q}{2}/\sqrt{-\left(\frac{p}{3}\right)^3}\right) && \text{(A.37)} \end{aligned}$$

If $\Delta = 0$

Then the roots u_k and v_k are equal. The main roots read

$$u_1 = v_1 = -\left(\frac{q}{2}\right)^{1/3} \tag{A.38}$$

As $\Delta = 0$,

$$\begin{aligned} q^2 + 4\left(\frac{p}{3}\right)^3 &= 0 \\ \left(\frac{q}{2}\right)^2 &= -\left(\frac{p}{3}\right)^3 \\ \left(\frac{q}{2}\right)^{2/3} &= -\frac{p}{3} \end{aligned} \tag{A.39}$$

. Thus

$$u_1 v_1 = u_1^2 = \left(\frac{q}{2}\right)^{2/3} = -\frac{p}{3} \tag{A.40}$$

and a first root is found:

$$\begin{aligned} y_1 &= u_1 + v_1 && \text{(A.41)} \\ y_1 &= -2\left(\frac{q}{2}\right)^{1/3} && \text{(A.42)} \end{aligned}$$

As $u_2 v_3 = u_3 v_2 = u_1^2 = -p/3$, a second real root exists:

$$\begin{aligned} y_2 &= u_2 + v_3 = u_3 + v_2 && \text{(A.43)} \\ &= u_2 + \bar{u_2} && \text{(A.44)} \\ &= 2Re(u_2) && \text{(A.45)} \\ &= 2u_1 cos\,(2\pi/3) && \text{(A.46)} \\ &= -u_1 && \text{(A.47)} \end{aligned}$$

Finally, if $\Delta = 0$, the two solutions of Eq. A.5 are:

$$\begin{aligned} X_1 &= -2\left(\frac{q}{2}\right)^{1/3} - \frac{b_2}{3} && \text{(A.48)} \\ X_2 &= \left(\frac{q}{2}\right)^{1/3} - \frac{b_2}{3} && \text{(A.49)} \end{aligned}$$

Bibliography

[Astrium 2011] Astrium. *Vulcain 2 Rocket Engine - Thrust Chamber: http://cs.astrium.eads.net/sp/launcher-propulsion/rocket-engines/vulcain-2-rocket-engine.html*, 2011. (Cited on pages 5 and 3.)

[AVBP 2011] AVBP. *AVBP Code: www.cerfacs.fr/cfd/avbp_code.php and www.cerfacs.fr/cfd/CFDPublications.html*, 2011. (Cited on page 19.)

[Baum *et al.* 1994] M. Baum, T. J. Poinsot and D. Thévenin. *Accurate boundary conditions for multicomponent reactive flows.* J. Comput. Phys. , vol. 116, pages 247–261, 1994. (Cited on page 36.)

[Bellan 2000] J. Bellan. *Supercritical (and subcritical) fluid behavior and modeling: drops, streams, shear and mixing layers, jets and sprays.* Progress in energy and combustion science, 2000. (Cited on pages 4 and 13.)

[Bellan 2006] J. Bellan. *Theory, modeling and analysis of turbulent supercritical mixing.* Combust. Sci. Tech. , vol. 178, pages 253–281, 2006. (Cited on pages 4 and 13.)

[Benedict *et al.* 1942] M. Benedict, G.B. Webb and L.C. Rubin. *An Empirical Equation for Thermodynamic Properties of Light Hydrocarbons and Their Mixtures II. Mixtures of Methane, Ethane, Propane, and n-Butane.* The Journal of Chemical Physics, vol. 10, page 747, 1942. (Cited on page 29.)

[Bird *et al.* 1960] R.B. Bird, W.E. Stewart and E.N. Lighfoot. Transport phenomena. John Wiley & Sons, New York, 1960. (Cited on pages 23 and 24.)

[Boivin *et al.* 2011] P. Boivin, C. Jiménez and A. L. Sánchez F.A. Williams. *An explicit reduced mechanism for H2-air combustion.* Proceedings of the Combustion Institute, vol. 33, pages 517–523, 2011. (Cited on page 40.)

[Branam & Mayer 2003] R. Branam and W. Mayer. *Characterisation of Cryogenic Injection at Supercritical pressure.* J. Prop. Power , vol. 19, no. 3, pages 342–355, May-June 2003. (Cited on page 7.)

[Burke & Schumann 1928] S. P. Burke and T. E. W. Schumann. *Diffusion flames.* Industrial and Engineering Chemistry, vol. 20, no. 10, pages 998–1005, 1928. (Cited on page 83.)

[Candel *et al.* 1998] S. Candel, G. Herding, R. Snyder, P. Scouflaire, J.C. Rolon, L. Vingert, M. Habiballah, F. Grisch, M. Pealat, P. Bouchardy*et al.* *Experimental investigation of shear coaxial cryogenic jet flames.* Journal of propulsion and power, vol. 14, no. 5, pages 826–834, 1998. (Cited on pages 4 and 77.)

[Candel *et al.* 2006] S. Candel, M. Juniper, G. Singla, P. Scouflaire and C. Rolon. *Structure and dynamics of cryogenic flames at supercritical pressure.* Combustion Science and Technology, vol. 178, no. 1, pages 161–192, 2006. (Cited on pages 4, 73, 77 and 98.)

[Chehroudi & Talley 2001] B. Chehroudi and D. Talley. Interaction of acoustic waves with a cryogenic nitrogen jet at sub-and supercritical pressures. Storming Media, 2001. (Cited on page 7.)

[Chehroudi *et al.* 2002a] B. Chehroudi, R. Cohn and D. Talley. *Cryogenic Shear Layers: Experiments and Phenomenological Modeling of the Initial Growth Rate under Subcritical and Supercritical Conditions.* International Journal of Heat and Fluid Flow, vol. 23, pages 554–563, October 2002. (Cited on pages 7 and 13.)

[Chehroudi *et al.* 2002b] B. Chehroudi, D. Talley and E. Coy. *Visual characteristics and initial growth rate of round cryogenic jets at subcritical and supercritical pressures.* Physics of Fluids, vol. 14, no. 2, pages 850–861, february 2002. (Cited on page 7.)

[Chen & Rodi 1980] CJ Chen and W. Rodi. *Vertical turbulent buoyant jets–A review of experimental data, 1980*, 1980. (Cited on page 56.)

[Cheng & Farmer 2006] G.C. Cheng and R. Farmer. *Real fluid modeling of multiphase flows in liquid rocket engine combustors.* Journal of Propulsion and Power, vol. 22, no. 6, page 1373, 2006. (Cited on page 78.)

[Chigier & Farago 1992] N. Chigier and Z. Farago. *Morphological classification of disintegration of round liquid jets in a coaxial air stream.* Atomization and Sprays, vol. 2, no. 2, 1992. (Cited on page 77.)

[Chung *et al.* 1984] T. H. Chung, L. L. Lee and K. E. Starling. *Applications of Kinetic Gas Theories and Multiparameter Correlation for Prediction of Dilute Gas Viscosity and Thermal Conductivity.* Industrial & Engineering Chemistry Fundamentals, vol. 23, pages 8–13, 1984. (Cited on pages 22 and 23.)

[Chung *et al.* 1988] T.H. Chung, M. Ajlan, L.L. Lee and K.E. Starling. *Generalized Multiparameter Correlation for Nonpolar and Polar Fluid Transport Properties.* Industrial & Engineering Chemistry Research, vol. 27, no. 4, pages 671–679, 1988. (Cited on pages 22 and 23.)

[CNES 2001] CNES, editeur. Combustion dans les moteurs fusées, 2001. (Cited on page 77.)

[Colin & Rudgyard 2000] O. Colin and M. Rudgyard. *Development of high-order Taylor-Galerkin schemes for unsteady calculations.* J. Comput. Phys. , vol. 162, no. 2, pages 338–371, 2000. (Cited on page 82.)

[Cutrone *et al.* 2010] L. Cutrone, P. De Palma, G. Pascazio and M. Napolitano. *A RANS flamelet-progress-variable method for computing reacting flows of real-gas mixtures.* Computers & Fluids, vol. 39, no. 3, pages 485 – 498, 2010. (Cited on page 78.)

[Demoulin *et al.* 2009] F.X. Demoulin, S. Zurbach and A. Mura. *High-Pressure Supercritical Turbulent Cryogenic Injection and Combustion: A Single-Phase Flow Modeling Proposal.* J. Prop. Power , vol. 25, no. 2, 2009. (Cited on page 78.)

[Enaux *et al.* 2011] B. Enaux, V. Granet, O. Vermorel, C. Lacour, C. Pera, C. Angelberger and T. Poinsot. *LES and experimental study of cycle-to-cycle variations in a spark ignition engine.* Proc. Combust. Inst. , vol. 33, pages 3115–3122, 2011. (Cited on page 19.)

[Favre-Marinet & Camano Schettini 2001] M. Favre-Marinet and EB Camano Schettini. *The density field of coaxial jets with large velocity ratio and large density differences.* International journal of heat and mass transfer, vol. 44, no. 10, pages 1913–1924, 2001. (Cited on page 12.)

[Foster & Miller 2011] J.W. Foster and R.S. Miller. *A Priori Analysis of Subgrid Mass Flux Vectors from Massively Parallel Direct Numerical Simulations of High Pressure H2/O2 Reacting Shear Layers.* In Proceedings of the 64th Annual Meeting of the American Physical Society Division of Fluid Dynamics, volume 56, Baltimore, Maryland,, November 20-22 2011. (Cited on page 13.)

[Foster 2009] J. Foster. A priori analysis of subgrid scalar phenomena and mass diffusion vectors in turbulent hydrogen-oxygen flames. Master's thesis, Clemson University, 2009. (Cited on page 13.)

[Gicquel *et al.* 2005] O. Gicquel, D. Thévenin and N. Darabiha. *Influence of differential diffusion on super-equilibrium temperature in turbulent non-premixed hydrogen/air flames.* Flow, turbulence and combustion, vol. 73, no. 3, pages 307–321, 2005. (Cited on page 68.)

[Giovangigli *et al.* 2011] V. Giovangigli, L. Matuszewski and F. Dupoirieux. *Detailed modeling of planar transcritical H2-O2-N2 flames.* Combustion Theory and Modelling, vol. 15, no. 2, pages 141–182, 2011. (Cited on pages 16, 20, 36 and 41.)

[Goodwin 2002] D. Goodwin. *Cantera: An object-oriented software toolkit for chemical kinetics, thermodynamics, and transport processes", Caltech, Pasadena, 2009. [Online].* http://code.google.com/p/cantera, 2002. (Cited on page 42.)

[Gourdain *et al.* 2009a] N. Gourdain, L.Y.M. Gicquel, M. Montagnac, O. Vermorel, M. Gazaix, G. Staffelbach, M. García, J.-F. Boussuge and T. Poinsot. *High performance parallel computing of flows in complex geometries - part 1: methods.* Computational Science and Discovery, vol. 2, no. November, page 015003 (26pp), 2009. (Cited on page 19.)

[Gourdain *et al.* 2009b] N. Gourdain, L.Y.M. Gicquel, G. Staffelbach, O. Vermorel, F. Duchaine, J.-F. Boussuge and T. Poinsot. *High performance parallel computing of flows in complex geometries - part 2: applications.* Computational Science and Discovery, vol. 2, no. November, page 015004 (28pp), 2009. (Cited on page 19.)

[Granet *et al.* 2010] V. Granet, O. Vermorel, T. Leonard, L. Gicquel, and T. Poinsot. *Comparison of Nonreflecting Outlet Boundary Conditions for Compressible Solvers on Unstructured Grids.* Am. Inst. Aeronaut. Astronaut. J. , vol. 48, no. 10, pages 2348–2364, 2010. (Cited on page 36.)

[Guezennec & Poinsot 2009] N. Guezennec and T. Poinsot. *Acoustically nonreflecting and reflecting boundary conditions for vorticity injection in compressible solvers.* AIAA Journal , vol. 47, pages 1709–1722, 2009. (Cited on page 85.)

[Haberzettl *et al.* 2000] A. Haberzettl, D. Gundel, K. Bahlmann and P. Vuillermoz. *European research and technology test bench P8 for high pressure liquid rocket propellants.* Paris, France, 29 Nov.- 01 Dec. 1999 2000. 3rd European Conference on Space Transportation Systems. (Cited on page 77.)

[Habiballah *et al.* 1996] M. Habiballah, L. Vingert, JC Traineau and P. Vuillermoz. *MASCOTTE- A test bench for cryogenic combustion research.* In IAF, International Astronautical Congress, 47 th, Beijing, China, 1996. (Cited on page 77.)

[Habiballah *et al.* 1998] M. Habiballah, L. Vingert, V. Duthoit and P. Vuillermoz. *Research as a key in the design methodology of liquid propellant combustion devices.* J. Prop. Power , vol. 14, no. 5, pages 782–788, 1998. (Cited on page 77.)

[Habiballah *et al.* 2006] M. Habiballah, M. Orain, F. Grisch, L. Vingert and P. Gicquel. *Experimental studies of high-pressure cryogenic flames on the mascotte facility.* Combust. Sci. Tech. , vol. 178, no. 1-3, pages 101–128, 2006. (Cited on pages 8, 4, 77, 96 and 97.)

[Haidn & Habiballah 2003] OJ Haidn and M. Habiballah. *Research on high pressure cryogenic combustion.* Aerospace Science and Technology, vol. 7, no. 6, pages 473–491, 2003. (Cited on page 4.)

[Herding *et al.* 1996] G. Herding, R. Snyder, P. Scouflaire, C. Rolon and S. Candel. *Flame stabilization in cryogenic propellant combustion.* In Symposium (International) on Combustion, volume 26, pages 2041–2047. Elsevier, 1996. (Cited on page 6.)

[Herding *et al.* 1998] G. Herding, R. Snyder, J.C. Rolon, S. Candel*et al. Investigation of cryogenic propellant flames using computerized tomography of emission images.* Journal of propulsion and power, vol. 14, no. 2, pages 146–151, 1998. (Cited on pages 6 and 7.)

[Herding 1997] G. Herding. *Analyse exp'erimentale de la combustion d'ergols cryog'eniques.* PhD thesis, 1997. (Cited on page 78.)

[Hirschfelder *et al.* 1954] J. O. Hirschfelder, C. F. Curtiss and R. B. Bird. Molecular theory of gases and liquids. Wiley, New York, 1954. (Cited on pages 23 and 24.)

[Jaegle 2009] F. Jaegle. *Large eddy simulation of evaporating sprays in complex geometries using Eulerian and Lagrangian methods*. 2009. (Cited on page 20.)

[Juniper & Candel 2003a] M. Juniper and S. Candel. *Edge diffusion flame stabilization behind a step over a liquid reactant*. Journal of propulsion and power, vol. 19, no. 3, pages 332–341, 2003. (Cited on pages 8 and 15.)

[Juniper & Candel 2003b] M.P. Juniper and S.M. Candel. *The stability of ducted compound flows and consequences for the geometry of coaxial injectors*. J. Fluid Mech. , vol. 482, pages 257–269, 2003. (Cited on pages 12 and 78.)

[Juniper *et al.* 2000] M. Juniper, A. Tripathi, P. Scouflaire, JC Rolon and S. Candel. *Structure of cryogenic flames at elevated pressures*. Proc. Combust. Inst. , vol. 28, no. 1, pages 1103–1110, 2000. (Cited on pages 7, 12 and 15.)

[Juniper *et al.* 2001] M. Juniper, B. Leroux, F. Lacas and S. Candel. Stabilization of cryogenic flames and effect of recess, pages 221–231. Cepadues, 2001. (Cited on page 78.)

[Juniper *et al.* 2003] M. Juniper, N. Darabiha and S. Candel. *The extinction limits of a hydrogen counterflow diffusion flame above liquid oxygen*. Combust. Flame , vol. 135, no. 1-2, pages 87–96, 2003. (Cited on pages 15 and 73.)

[Juniper 2001] M. Juniper. *Structure and stabilization of cryogenic spray flames*. PhD thesis, Ecole Centrale Paris, 2001. (Cited on pages 5, 9, 45 and 88.)

[Kendrick *et al.* 1999] D. Kendrick, G. Herding, P. Scouflaire, C. Rolon and S. Candel. *Effects of a Recess on Cryogenic Flame Stabilization*. Combust. Flame , vol. 118, pages 327–339, 1999. (Cited on pages 78 and 103.)

[Kim *et al.* 2010] T. Kim, Y. Kim and S.K. Kim. *Numerical study of cryogenic liquid nitrogen jets at supercritical pressures*. The Journal of Supercritical Fluids, 2010. (Cited on page 13.)

[Kim *et al.* 2011] T. Kim, Y. Kim and S.K. Kim. *Numerical analysis of gaseous hydrogen/liquid oxygen flamelet at supercritical pressures*. International Journal of Hydrogen Energy, 2011. (Cited on page 55.)

[Kraichnan 1970] R.H. Kraichnan. *Diffusion by a random velocity field*. Phys. Fluids , vol. 13, pages 22–31, 1970. (Cited on page 85.)

[Lamarque 2007] N. Lamarque. *Schémas numériques et conditions limites pour la simulation aux grandes échelles de la combustion diphasique dans les foyers d'hélicoptère*. Phd thesis, INP Toulouse, 2007. (Cited on page 20.)

[Lasheras *et al.* 1998] JC Lasheras, E. Villermaux and EJ Hopfinger. *Break-up and atomization of a round water jet by a high-speed annular air jet.* Journal of Fluid Mechanics, vol. 357, no. 1, pages 351–379, 1998. (Cited on page 12.)

[Lemmon *et al.* 1998] EW Lemmon, MO McLinden and DG Friend. Nist-janaf thermochemical tables. National Institute of Standards and Technology, 1998. (Cited on page 41.)

[Lemmon *et al.* 2009] EW Lemmon, MO McLinden and DG Friend. *Thermophysical properties of fluid systems.* NIST chemistry webbook, NIST standard reference database, vol. 69, 2009. (Cited on pages 5, 23 and 30.)

[Locke *et al.* 2010] J.M. Locke, S. Pal, R.D. Woodward and R.J. Santoro. *High Speed Visualization of LOX/GH2 Rocket Injector Flowfield: Hot-Fire and Cold-Flow Experiments.* 2010. (Cited on pages 5, 9 and 10.)

[Masquelet *et al.* 2009] M. Masquelet, S. Menon, Y. Jin and R. Friedrich. *Simulation of unsteady combustion in a LOX-GH2 fueled rocket engine.* Aerospace Science and Technology, 2009. (Cited on pages 16 and 78.)

[Matsuyama *et al.* 2006] S. Matsuyama, J. Shinjo, Y. Mizobuchi and S. Ogawa. *A Numerical Investigation on Shear Coaxial LOx/GH2 Jet Flame at Supercritical Pressure.* In 44th AIAA Aerospace Sciences Meeeting and Exhibit, Reno, Nevada, numéro 761, 2006. (Cited on pages 16 and 78.)

[Matsuyama *et al.* 2010] S. Matsuyama, J. Shinjo, S. Ogawa and Y. Mizobuchi. *Large Eddy Simulation of LOX/GH2 Shear-Coaxial Jet Flame at Supercritical Pressure.* In 48th AIAA Aerospace Sciences Meeting Including the New Horizons Forum and Aerospace Exposition, Orlando, Florida, numéro 208, 2010. (Cited on pages 5, 16, 17 and 78.)

[Matuszewski 2011] L. Matuszewski. *Modélisation et simulation numérique des phénomènes de combustion en régime supercritique.* PhD thesis, Ecole Polytechnique, March 2011. (Cited on page 78.)

[Mayer & Branan 2004] W. Mayer and R. Branan. *Atomization characteristics on the surface of a round liquid jet.* Exp. Fluids , vol. 36, pages 528–539, 2004. (Cited on page 7.)

[Mayer & Smith 2004] W.O.H. Mayer and J.J. Smith. *Fundamentals of supercritical mixing and combustion of cryogenic propellants.* Liquid rocket thrust chambers: aspects of modeling, analysis, and design, page 339, 2004. (Cited on page 7.)

[Mayer & Tamura 1996] W. Mayer and H. Tamura. *Propellant injection in a liquid oxygen/gaseous hydrogen rocket engine.* J. Prop. Power , vol. 12, no. 6, pages 1137–1147, November-December 1996. (Cited on page 7.)

[Mayer *et al.* 1996] W. Mayer, A. Schik, C. Schweitzer and M. Schaffler. *Injection and mixing processes in high pressure LOX/GH2 rocket combustors, AIAA Paper No. 96-2620*. 32nd AIAA/ASME/SAE/ASEE Joint Propulsion Conference & Exhibit, Lake Buena Vista, Florida, 1996. (Cited on page 7.)

[Mayer *et al.* 1998a] W. Mayer, A. Ivancic, A. Schik and U. Hornung. *Propellant atomization in LOX/GH2 rocket combustors*. AIAA Paper, pages 98–3685, 1998. (Cited on page 7.)

[Mayer *et al.* 1998b] W. Mayer, A. Schik, B. Vielle, C. Chaveau, I. Gökalp and D. Talley. *Atomization and breakup of cryogenic propellants under high pressure subcritical and supercritical conditions*. J. Prop. Power , vol. 14, no. 5, pages 835–842, 1998. (Cited on page 7.)

[Mayer *et al.* 2000] W. Mayer, A. Schik, M. Schäffler and H. Tamura. *Injection and Mixing Processes in High-Pressure Liquid Oxygen/Gaseous Hydrogen Rocket Combustor*. J. Prop. Power , vol. 16, no. 5, pages 823–828, September-October 2000. (Cited on page 7.)

[Mayer *et al.* 2001] W. Mayer, B. Ivancic, A. Schik and U. Hornung. *Propellant atomization and ignition phenomena in liquid oxygen / gaseous hydrogen rocket combustors*. J. Prop. Power , vol. 17, page 794, 2001. (Cited on page 7.)

[Mayer *et al.* 2003] W. Mayer, J. Tellar, R. Branam, G. Schneider and J. Hussong. *Raman Measurement of Cryogenic Injection at Supercritical Pressure.* , vol. 39, pages 709–719, 2003. (Cited on pages 7 and 13.)

[Meng & Yang 2003] Hua Meng and Vigor Yang. *A Unified Treatment of General Fluid Thermodynamics and Its Application to a Preconditioning Scheme*. J. Comput. Phys. , vol. 189, pages 277–304, July 2003. (Cited on pages 22 and 28.)

[Moin & Mahesh 1998] P. Moin and K. Mahesh. *Direct numerical simulation: a tool in turbulence research*. Annual Review of Fluid Mechanics, vol. 30, no. 1, pages 539–578, 1998. (Cited on page 38.)

[Nicoud & Ducros 1999] F. Nicoud and F. Ducros. *Subgrid-scale stress modelling based on the square of the velocity gradient*. Flow, Turb. and Combustion , vol. 62, no. 3, pages 183–200, 1999. (Cited on page 28.)

[Oefelein & Yang 1998] J.C. Oefelein and V. Yang. *Modeling High-Pressure Mixing and Combustion Processes in Liquid Rocket Engines*. J. Prop. Power , vol. 14, no. 5, 1998. (Cited on pages 5, 15 and 34.)

[Oefelein 2001] J.C. Oefelein. *A Perspective on LES and its Application to Liquid Rocket Combustion Systems*, 2001. (Cited on page 34.)

[Oefelein 2005] J.C. Oefelein. *Thermophysical characteristics of shear-coaxial LOX-H2 flames at supercritical pressure.* Proceedings of the Combustion Institute, vol. 30, no. 2, pages 2929–2937, 2005. (Cited on pages 34 and 38.)

[Oefelein 2006] J. Oefelein. *Mixing and combustion of cryogenic oxygen-hydrogen shear-coaxial jet flames at supercritical pressure.* Combust. Sci. Tech. , vol. 178, no. 1-3, pages 229–252, 2006. (Cited on pages 4, 22, 24 and 34.)

[Okong'o & Bellan 2002a] N. Okong'o and J. Bellan. *Consistent Boundary Conditions for Multicomponent Real Gas Mixtures Based on Characteristic Waves.* Journal of Computational Physics, vol. 176, pages 330–344, 2002. (Cited on page 36.)

[Okong'o & Bellan 2002b] N.A. Okong'o and J. Bellan. *Direct numerical simulation of a transitional supercritical binary mixing layer: heptane and nitrogen.* J. Fluid Mech. , vol. 464, pages 1–34, 2002. (Cited on pages 13, 57 and 93.)

[Oppenheim *et al.* 1989] A.V. Oppenheim, R.W. Schafer, J.R. Buck*et al.* Discrete-time signal processing, volume 2. Prentice hall Englewood Cliffs, NJ:, 1989. (Cited on page 47.)

[Oschwald *et al.* 2006] M. Oschwald, J. J. Smith, R. Branam, J. Hussong, A. Schik, B. Chehroudi and D. Talley. *Injection of Fluids into Supercritical Environments.* Combust. Sci. Tech. , vol. 178, pages 49–100, 2006. (Cited on pages 4 and 57.)

[Papamoschou & Roshko 1988] D. Papamoschou and A. Roshko. *The compressible turbulent shear layer: an experimental study.* J. Fluid Mech. , vol. 197, pages 453–477, 1988. (Cited on page 37.)

[Peng & Robinson 1976] Ding-Yu Peng and Donald B. Robinson. *A New Two-Constant Equation of State.* Industrial & Engineering Chemistry Fundamentals, vol. 15, pages 59–64, February 1976. (Cited on pages 29 and 35.)

[Peters 2001] N. Peters. Turbulent combustion. Cambridge University Press, 2001. (Cited on pages 5, 82 and 83.)

[Petrova & Williams 2006] M.V. Petrova and F.A. Williams. *A small detailed chemical-kinetic mechanism for hydrocarbon combustion.* Combust. Flame , vol. 144, no. 3, pages 526 – 544, 2006. (Cited on page 41.)

[Pierce & Moin 1998] C. D. Pierce and P. Moin. *A dynamic model for subgrid scale variance and dissipation rate of a conserved scalar.* Phys. Fluids , vol. 10, no. 12, pages 3041–3044, 1998. (Cited on page 83.)

[Pohl *et al.* 2011] S. Pohl, M. Jarczyk and M. Pfitzner. *A real gas laminar flamelet combustion model for the CFD-Simulation of LOX/GH2 combustion.* 2011. (Cited on page 78.)

[Poinsot & Lele 1992] T. Poinsot and S. Lele. *Boundary conditions for direct simulations of compressible viscous flows.* J. Comput. Phys. , vol. 101, no. 1, pages 104–129, 1992. (Cited on page 36.)

[Poinsot & Veynante 2005] T. Poinsot and D. Veynante. Theoretical and numerical combustion. R.T. Edwards, 2nd edition, 2005. (Cited on pages 5, 6, 21 and 26.)

[Polyanin & Manzhirov 2007] A.D. Polyanin and A.V. Manzhirov. Handbook of mathematics for engineers and scientists. Chapman & Hall/CRC, 2007. (Cited on page 107.)

[Pons *et al.* 2008] L. Pons, N. Darabiha and S. Candel. *Pressure effects on nonpremixed strained flames.* Combust. Flame , vol. 152, no. 1-2, pages 218–229, 2008. (Cited on page 15.)

[Pons *et al.* 2009] L. Pons, N. Darabiha, S. Candel, T. Schmitt and B. Cuenot. *The structure of multidimensional strained flames under transcritical conditions.* Comptes rendus-Mécanique, vol. 337, no. 6-7, pages 517–527, 2009. (Cited on page 42.)

[Poschner & Pfitzner 2009] M. Poschner and M. Pfitzner. *CFD-Simulation of supercritical LOX/GH2 combustion considering consistent real gas thermodynamics.* In Proceedings of the European Combustion Meeting 2009. The Combustion Institute, 2009. (Cited on page 78.)

[Pourouchottamane *et al.* 2001] M. Pourouchottamane, V. Burnley, F. Dupoirieux, M. Habiballah and L. Vingert. *Numerical analysis of the 10 bar MASCOTTE flow field.* Heilbronn, Germany, 26-27 march 2001 2001. 2nd International Workshop on Rocket Combustion Modeling. (Cited on page 77.)

[Raynal 1997] L. Raynal. *Instabilite et entrainement a l'interface d'une couche de melange liquide-gaz.* PhD thesis, Universite Joseph Fourier, Grenoble, 1997. (Cited on page 37.)

[Renard *et al.* 2000] P.H. Renard, D. Thévenin, JC Rolon and S. Candel. *Dynamics of flame/vortex interactions.* Progress in energy and combustion science, vol. 26, no. 3, pages 225–282, 2000. (Cited on page 64.)

[Ribert *et al.* 2008] G. Ribert, N. Zong, V. Yang, L. Pons, N. Darabiha and S. Candel. *Counterflow diffusion flames of general fluids: Oxygen/hydrogen mixtures.* Combustion and Flame, vol. 154, no. 3, pages 319–330, 2008. (Cited on pages 15, 43, 68 and 73.)

[Richard & Nicoud 2011] J Richard and F Nicoud. *Effect of the Fluid Structure Interaction on the Aeroacoustic Instabilities of Solid Rocket Motors.* 17th AIAA/CEAS Aeroacoustics Conference (32nd AIAA Aeroacoustics Conference), 2011. (Cited on page 2.)

[Roshko 1961] A. Roshko. *Experiments on the flow past a circular cylinder at very high Reynolds number.* Journal of Fluid Mechanics, vol. 10, no. 03, pages 345–356, 1961. (Cited on page 47.)

[Roux *et al.* 2005] S. Roux, G. Lartigue, T. Poinsot, U. Meier and C. Bérat. *Studies of mean and unsteady flow in a swirled combustor using experiments, acoustic analysis and Large Eddy Simulations.* Combust. Flame , vol. 141, pages 40–54, 2005. (Cited on page 19.)

[Roux *et al.* 2010] A. Roux, L. Y. M. Gicquel, S. Reichstadt, N. Bertier, G. Staffelbach, F. Vuillot and T. Poinsot. *Analysis of unsteady reacting flows and impact of chemistry description in Large Eddy Simulations of side-dump ramjet combustors.* Combust. Flame , vol. 157, pages 176–191, 2010. (Cited on page 19.)

[Rutgers 1998] M.A. Rutgers. *Forced 2D turbulence: experimental evidence of simultaneous inverse energy and forward enstrophy cascades.* Physical review letters, vol. 81, no. 11, pages 2244–2247, 1998. (Cited on page 47.)

[Sagaut 2002] P. Sagaut. Large eddy simulation for incompressible flows. Springer, 2002. (Cited on page 28.)

[Schmitt *et al.* 2009] T. Schmitt, L. Selle, B. Cuenot and T. Poinsot. *Large-Eddy Simulation of transcritical flows.* Comptes Rendus Mécanique, vol. 337, no. 6-7, pages 528–538, 2009. (Cited on pages 16, 78 and 80.)

[Schmitt *et al.* 2010a] T. Schmitt, Y. Méry, M. Boileau and S. Candel. *Large-Eddy Simulation of oxygen/methane flames under transcritical conditions.* Proceedings of the Combustion Institute, vol. In Press, Corrected Proof, pages –, 2010. (Cited on pages 5, 16, 17, 78, 82, 83 and 84.)

[Schmitt *et al.* 2010b] T. Schmitt, L. Selle, A. Ruiz and B. Cuenot. *Large-Eddy Simulation of Supercritical-Pressure Round Jets.* AIAA Journal , vol. 48, no. 9, pages 2133–2144, September 2010. (Cited on pages 13, 35, 56 and 84.)

[Schmitt 2009] T. Schmitt. *Simulation des Grandes Echelles de la combustion turbulente à pression supercritique.* PhD thesis, Institut National Polytechnique de Toulouse, 2009. (Cited on pages 28, 39, 78 and 105.)

[Schumaker & Driscoll 2009] S.A. Schumaker and J.F. Driscoll. *Coaxial turbulent jet flames: Scaling relations for measured stoichiometric mixing lengths.* Proceedings of the Combustion Institute, vol. 32, no. 2, pages 1655–1662, 2009. (Cited on pages 5 and 11.)

[Selle *et al.* 2004] L. Selle, G. Lartigue, T. Poinsot, R. Koch, K.-U. Schildmacher, W. Krebs, B. Prade, P. Kaufmann and D. Veynante. *Compressible Large-Eddy Simulation of turbulent combustion in complex geometry on unstructured meshes.* Combust. Flame , vol. 137, no. 4, pages 489–505, 2004. (Cited on page 19.)

[Senoner 2010] J.M. Senoner. *Simulations aux grandes échelles de l'écoulement diphasique dans un brûleur aéronautique par une approche Euler-Lagrange.* 2010. (Cited on page 20.)

[Singla *et al.* 2005] G. Singla, P. Scouflaire, C. Rolon and S. Candel. *Transcritical oxygen/transcritical or supercritical methane combustion.* Proceedings of the Combustion Institute, vol. 30, no. 2, pages 2921–2928, 2005. (Cited on pages 7, 8, 34 and 73.)

[Singla *et al.* 2006] G. Singla, P. Scouflaire, C. Rolon and S. Candel. *Planar laser-induced fluorescence of OH in high-pressure cryogenic LOx/GH2 jet flames.* Combust. Flame , vol. 144, no. 1-2, pages 151–169, 2006. (Cited on page 9.)

[Singla *et al.* 2007] G. Singla, P. Scouflaire, JC Rolon and S. Candel. *Flame stabilization in high pressure LOx/GH2 and GCH4 combustion.* Proceedings of the Combustion Institute, vol. 31, no. 2, pages 2215–2222, 2007. (Cited on pages 5, 7, 8, 9, 10, 15, 34, 35, 63, 73, 74 and 75.)

[Singla 2005] G. Singla. *Etude des Flammes Cryotechniques Oxyène/Méthane à Haute Pression.* PhD thesis, Ecole Centrale Paris, 2005. (Cited on pages 5 and 17.)

[Smagorinsky 1963] J. Smagorinsky. *General circulation experiments with the primitive equations: 1. The basic experiment.* Mon. Weather Rev. , vol. 91, pages 99–164, 1963. (Cited on page 28.)

[Smirnov *et al.* 2001] A. Smirnov, S. Shi and I. Celik. *Random flow generation technique for large eddy simulations and particle-dynamics modeling.* Trans. ASME. J. Fluids Eng. , vol. 123, pages 359–371, 2001. (Cited on page 85.)

[Snecma 2011] Snecma. *Vulcain2*, 2011. (Cited on pages 5, 2 and 3.)

[Snyder *et al.* 1997] R. Snyder, G. Herding, J. C. Rolon and S. Candel. *Analysis of Flame Patterns in Cryogenic Propellant Combustion.* Combustion Science and Technology, vol. 124, pages 331–370, 1997. (Cited on pages 6 and 12.)

[Soave 1972] G. Soave. *Equilibrium constants from a modified Redlich-Kwong equation of state.* Chemical Engineering Science, vol. 27, no. 6, pages 1197–1203, 1972. (Cited on page 29.)

[Takahashi 1974] S. Takahashi. *Preparation of a generalized chart for the diffusion coefficients of gases at high pressures.* J. Chem. Eng. (Japan), 1974. (Cited on page 24.)

[Teshome *et al.* 2011] Sophonias Teshome, Ivett Leyva and Douglas Talley. Nearcritical shear coaxial flows (private communication). 2011. (Cited on pages 5, 7 and 8.)

[Vallgren & Lindborg 2011] A. Vallgren and E. Lindborg. *The enstrophy cascade in forced two-dimensional turbulence.* Journal of Fluid Mechanics, vol. 671, no. 1, pages 168–183, 2011. (Cited on page 47.)

[Vermorel *et al.* 2009] O. Vermorel, S. Richard, O. Colin, C. Angelberger, A. Benkenida and D. Veynante. *Towards the understanding of cyclic variability in a spark ignited engine using multi-cycle LES.* Combust. Flame , vol. 156, no. 8, pages 1525–1541, 2009. (Cited on page 19.)

[Vingert *et al.* 1998] L. Vingert, M. Habiballah, P. Gicquel, E. Brisson, S. Candel, G. Herding, R. Snyder, P. Scouflaire, C. Rolon, D. Stepowski*et al. Optical diagnostics for cryogenic liquid propellants combustion.* In AGARD conference proceedings, pages 44–1. AGARD, 1998. (Cited on page 77.)

[Vingert *et al.* 2000] L. Vingert, M. Habiballah and JC Traineau. *Mascotte, a research test facility for high pressure combustion of cryogenic propellants.* In AAAF/CEAS, European Aerospace Conference, 12 th, Paris, France, Nov. 29-Dec. 1, 1999, ONERA, TP, numéro 2000-15, 2000. (Cited on page 77.)

[Vingert *et al.* 2002] L. Vingert, M. Habiballah and P. Vuillermoz. *Upgrading of the Mascotte cryogenic test bench to the LOX/Methane combustion studies.* In 4th International Conference on Launcher Technology "Space Launcher Liquid Propulsion", Liège, Belgium, 2002. (Cited on page 77.)

[William P. Rogers 1986] David Acheson Eugene Covert Richard Feynman Robert Hotz Donald Kutyna Sally Ride Robert Rummel Joseph Sutter Arthur Walker Albert Wheelon Chuck Yeager William P. Rogers Neil Armstrong. Report of the presidential commission on the space shuttle challenger accident. 1986. (Cited on page 2.)

[Williamson & Brown 1998] CHK Williamson and GL Brown. *A series in 1/[radical sign] Re to represent the Strouhal-Reynolds Number relationship of the cylinder wake.* Journal of Fluids and Structures, vol. 12, no. 8, pages 1073–1085, 1998. (Cited on page 47.)

[Wolf *et al.* 2009] P. Wolf, G. Staffelbach, A. Roux, L. Gicquel, T. Poinsot and V. Moureau. *Massively parallel LES of azimuthal thermo-acoustic instabilities in annular gas turbines.* C. R. Acad. Sci. Mécanique, vol. 337, no. 6-7, pages 385–394, 2009. (Cited on page 19.)

[Zong & Yang 2006] N. Zong and V. Yang. *Cryogenic fluid jets and mixing layers in transcritical and supercritical environments.* Combust. Sci. Tech. , vol. 178, pages 193–227, 2006. (Cited on pages 5, 13, 14, 35 and 47.)

[Zong & Yang 2007] N. Zong and V. Yang. *Near-field flow and flame dynamics of LOX/methane shear-coaxial injector under supercritical conditions.* Proceedings of the Combustion Institute, vol. 31, no. 2, pages 2309–2317, 2007. (Cited on pages 15, 35 and 47.)

[Zong *et al.* 2004] Nan Zong, Hua Meng, Shih-Yang Hsieh and Vigor Yang. *A numerical study of cryogenic fluid injection and mixing under supercritical conditions.* Physics of Fluids, vol. 16, pages 4248–4261, December 2004. (Cited on page 13.)

[Zurbach 2006] Stephan Zurbach, editeur. Supercritical combustion modeling of the rcm-2 test-case : Mascotte 60 bar, 2006. (Cited on pages 8, 96 and 97.)